

2017

# Predicting heavy oil and bitumen viscosity from well logs and calculated seismic properties

Rops, Eric

---

Rops, E. (2017). Predicting heavy oil and bitumen viscosity from well logs and calculated seismic properties (Master's thesis, University of Calgary, Calgary, Canada). Retrieved from <https://prism.ucalgary.ca>. doi:10.11575/PRISM/27402

<http://hdl.handle.net/11023/3705>

*Downloaded from PRISM Repository, University of Calgary*

UNIVERSITY OF CALGARY

Predicting heavy oil and bitumen viscosity from well logs and calculated seismic properties

by

Eric Anthony Rops

A THESIS

SUBMITTED TO THE FACULTY OF GRADUATE STUDIES  
IN PARTIAL FULFILMENT OF THE REQUIREMENTS FOR THE  
DEGREE OF MASTER OF SCIENCE

GRADUATE PROGRAM IN GEOLOGY AND GEOPHYSICS

CALGARY, ALBERTA

APRIL, 2017

© Eric Anthony Rops 2017

## Abstract

Viscosity is the most important parameter influencing heavy oil production and development. While heavy oil viscosities can be measured in the lab from core and wellhead samples, it would be very useful to have a method to reliably estimate heavy oil viscosity directly from well logs.

Multi-attribute analysis enables a target attribute (viscosity) to be predicted from other known attributes (the well logs). The viscosity measurements were generously provided by Donor Company, which allowed viscosity prediction equations to be trained.

Once the best method of training the prediction was determined, viscosity was successfully predicted from resistivity, gamma-ray, NMR porosity, spontaneous potential, and the sonic logs. The predictions modelled vertical viscosity variations throughout the reservoir interval, while matching the true measurements with a 0.76 correlation.

Another set of viscosity predictions were generated using log-derived seismic properties. The top viscosity-predicting seismic properties were found to be P-wave velocity and acoustic impedance. They predicted viscosity with an average validation error less than one standard deviation, however the predictions were less detailed with a correlation of only 0.35.

Also explored in this thesis was the effect of including depth as a viscosity predictor, predicting viscosity from acoustic logs scaled to seismic frequencies, and bitumen-water contact detection from acoustic logs.

## **Acknowledgements**

First and foremost, I want to thank my supervisor, Dr. Larry Lines, for taking me on as his (potentially last) student. I am grateful to him for giving me the freedom to pursue a topic of great interest to me, and for his constant encouragement and positivity. This thesis was an interesting progression stemming from my GOPH 701 work in April 2015 and has evolved ever since.

A special thank-you to Bob Everett who took an interest to this research at GeoConvention 2016. Since then he has consistently offered his professional advice assisting me with the well log analysis, and even gave me a two-week crash course in advanced petrophysical interpretation. I cannot state enough how valuable that was for me.

I also want to thank David Gray, Scott Keating, Doug Clark, Rudy Strobl, Kevin Pyke, and Xianfeng Zhang for their thoughts and suggestions related to this work. This thesis could not have turned out as it did without the contributions from all these individuals.

A sincere thank-you to Dr. Brian Russell and Dr. Brij Maini for taking the time to be on my defense committee and for actually having to read this whole thesis. Thank-you also to Dr. Roy Lindseth for graciously assisting with the technical writing.

Thank-you to CREWES sponsors and NSERC for funding this research, to the anonymous donor company for providing the viscosity data, and to CGG Hampson-Russell for making their software available to CREWES students.

Finally, I want to acknowledge Bobby Gunning, Jason Levesque, Adriana Gordon, Andrew Mills, and several others for helping make my graduate student experience as enjoyable as it was!

## Table of Contents

Abstract.....	ii
Acknowledgements .....	iii
Table of Contents .....	iv
List of Tables .....	vi
List of Figures and Illustrations .....	vii
List of Symbols, Abbreviations and Nomenclature .....	xi
<b>Chapter 1 – Introduction .....</b>	<b>1</b>
1.1 - Introduction to oil sands, heavy oil, and viscosity .....	1
1.2 – Shear properties of heavy oil .....	5
1.3 – Previous studies of estimating heavy oil viscosity .....	9
1.4 – Motivation and goals of this thesis .....	11
<b>Chapter 2 – Well Logging Principles .....</b>	<b>13</b>
2.1 – Overview of the well log measurement .....	13
2.2 – Overview of the total gamma ray tool.....	14
2.3 – Overview of the induction resistivity tool .....	15
2.4 – Overview of the spontaneous potential (SP) tool .....	17
2.5 – Overview of the density logging tool .....	19
2.6 – Overview of the sonic logging tool.....	21
2.7 – Overview of Nuclear Magnetic Resonance (NMR) logging .....	25
<b>Chapter 3 – Theory of Multilinear Regression .....</b>	<b>29</b>
3.1 – Multi-Attribute Analysis .....	29
3.2 – Step-Wise Regression .....	32
3.3 – Cross-Validation .....	33
<b>Chapter 4 – Study Area Geology and Dataset.....</b>	<b>36</b>
4.1 – Introduction to Study Area.....	36
4.2 – Study Area Geology .....	37
4.3 – Dataset.....	42
<b>Chapter 5 – Problem Setup, and Viscosity Prediction Results.....</b>	<b>45</b>
5.1 – Well log normalization process.....	45
5.2 – Adding NMR logs as viscosity predicting attributes .....	47
5.3 – Viscosity training model.....	49
5.4 – Viscosity prediction results from all logs, and seismic properties.....	51
5.5 – Visualizing the viscosity predictions .....	54
5.6 – Viscosity prediction from standard logs, and predicting log <sub>10</sub> (viscosity).....	61
5.7 – Blind test on a well from a nearby reservoir .....	65
5.8 – Adding depth as a viscosity predictor .....	67
5.9 – Predicting viscosity using acoustic logs upscaled to seismic frequencies.....	71
5.10 – Predicting resistivity from log-derived seismic properties .....	74

<b>Chapter 6 – Discussion and Conclusions .....</b>	<b>78</b>
<b>6.1 – Comments regarding the well logs used to predict viscosity .....</b>	<b>78</b>
<b>6.2 – Concluding remarks regarding viscosity prediction from all well logs .....</b>	<b>80</b>
<b>6.3 – Concluding remarks regarding viscosity prediction from standard well         logs only.....</b>	<b>81</b>
<b>6.4 – Concluding remarks regarding viscosity prediction from calculated         seismic properties.....</b>	<b>81</b>
<b>6.5 – Concluding remarks regarding depth as a viscosity predictor.....</b>	<b>82</b>
<b>6.6 – Concluding remarks regarding the potential of seismic data for viscosity         prediction .....</b>	<b>82</b>
<b>6.7 – Future Work.....</b>	<b>83</b>
<b>6.8 – Final Remark.....</b>	<b>84</b>
<b>References .....</b>	<b>86</b>
<b>Appendices.....</b>	<b>90</b>
<b>A.1. Viscosity prediction equations .....</b>	<b>90</b>
<b>A.2. Other useful prediction equations not discussed in the main text.....</b>	<b>92</b>
<b>A.3. Viscosity - Depth relation from the ConocoPhillips Surmont project .....</b>	<b>93</b>

## List of Tables

Table 5-1: Emerge™ top predicting attributes for NMR Total Porosity.....	47
Table 5-2: Emerge™ top predicting attributes for NMR Free Porosity. ....	47
Table 5-3: Emerge™ top predicting attributes for NMR Moveable Fluid Porosity.....	47
Table 5-4: Comparison of the three viscosity prediction methods .....	64
Table 5-5: Emerge™ top viscosity predicting attributes using acoustic logs upscaled to..... seismic frequencies .....	71
Table 5-6: Emerge™ top resistivity predicting attributes from calculated seismic properties.....	75

## List of Figures and Illustrations

Figure 1-1: Oil grade categories, defined by their API gravity values. ....	1
Figure 1-2: Viscosity concept from laminar shear of two plates.....	2
Figure 1-3: Oil viscosities by grade category, compared to typical kitchen items. ....	3
Figure 1-4: Temperature dependence of oil viscosity using the Beggs & Robinson (1975) relation at API values of -5, 10, and 25 .....	4
Figure 1-5: Ultrasonic compressional waveforms measured through a very heavy oil (API = -5) at -12.5°C and 49.3°C. ....	5
Figure 1-6: Bulk modulus and shear modulus for an API 8° heavy oil .....	6
Figure 1-7: Frequency dependence of velocity for a heavy oil saturated carbonate rock from Texas. ....	6
Figure 1-8: Shear modulus – temperature – frequency relation from lab measurements of a heavy oil saturated carbonate from Uvalde, Texas .....	8
Figure 1-9: Viscosity tomogram from Vasheghani & Lines (2012). ....	9
Figure 1-10: A pseudo-viscosity log produced from two NMR logging parameters ( $T_2$ and HI), calibrated to laboratory viscosity measurements from the Athabasca oil sands .....	11
Figure 2-1: The elements of well logging .....	13
Figure 2-2: The life of a single gamma ray, which is emitted in the formation and ultimately detected by a NaI detector in the borehole.....	15
Figure 2-3: The principle of the induction tool.....	16
Figure 2-4: Borehole mud invasion profile: “step model” of invasion.....	17
Figure 2-5: A schematic representation of the development of the spontaneous potential signal in a borehole .....	18
Figure 2-6: Schematic diagram of a density tool .....	19
Figure 2-7: A typical acoustic waveform recorded in a borehole.....	22
Figure 2-8: Simplified schematic of a sonic array logging system.....	23
Figure 2-9: a) An array of waveforms showing increasing moveout from near to far receivers. b) A slowness-time map in which coherent peaks correlate to different wave components. c) A continuous log is built from repeating steps (a) and (b) at each depth measurement point .....	24

Figure 2-10: A summary of the idealized interpretation of T <sub>2</sub> distributions for water wet clastic rocks.....	26
Figure 2-11: NMR T <sub>2</sub> distributions as a function of depth.....	27
Figure 2-12: Oil sands well in the study area with NMR data.....	28
Figure 3-1: (Left): Cross-plotting against 1 attribute gives a line best fit. (Right): Cross-plotting against 2 attributes gives a planar best fit.....	29
Figure 3-2: Illustration of the basic multi-attribute regression problem.....	29
Figure 3-3: Example: Cross-plot of predicted V <sub>p</sub> against measured V <sub>p</sub> .....	31
Figure 3-4: An Emerge™ prediction error plot. ....	34
Figure 3-5: Illustration of how a higher order polynomial can over-fit the training data.....	35
Figure 4-1: Distribution of Alberta’s oil sands deposits.....	36
Figure 4-2: Stratigraphic chart for the McMurray oil sands system.....	38
Figure 4-3: Log suite for an example well in the study area .....	39
Figure 4-4: Stratigraphic framework for the McMurray Formation.....	41
Figure 4-5: Map of the oil sands study area.....	43
Figure 4-6: Histogram of all laboratory viscosity measurements throughout the study area. ....	44
Figure 4-7: Distribution map of the base reservoir viscosity measurements.....	44
Figure 5-1: Distribution of the gamma ray values for the 40 training wells.....	45
Figure 5-2: What the normalized logs look like (red) versus the un-normalized logs (blue). ....	46
Figure 5-3: Distribution of the 25 NMR wells in the study area .....	48
Figure 5-4: Predicting NMR porosities from Resistivity, P-wave sonic, Gamma Ray, and Neutron Porosity. Validation results for two example wells are shown. ....	49
Figure 5-5: Illustrating the old and new viscosity training models using all well logs .....	50
Figure 5-6: Viscosity training model using only log-derived seismic properties.....	51
Figure 5-7: <u>Top:</u> Emerge™ prediction error plot and cross-plot for viscosity using the new training model, and all the available well logs as the predicting attributes. In the crossplot, each color represents a different well. <u>Bottom:</u> The list of attributes with their associated validation errors.....	52

Figure 5-8: <i>Top:</i> Emerge™ prediction error plot and cross-plot for viscosity using the new training model, and calculated seismic properties as the predicting attributes. In the cross-plot, each color represents a different well. <i>Bottom:</i> The list of attributes with their associated validation errors. ....	53
Figure 5-9: Viscosity predictions (validation results) for an example well where the viscosity trend continues 20m above the top measurement. ....	56
Figure 5-10: Viscosity predictions (validation results) for an example well where two viscosity gradients are modelled from 440m to 460m, separated by a shaley zone. ....	57
Figure 5-11: Viscosity predictions (validation results) for an example well where two viscosity gradients are modelled throughout the reservoir interval. ....	58
Figure 5-12: Viscosity predictions (validation results) for an example well with a smooth increasing viscosity gradient with depth, and a beautiful inverse correlation with resistivity. ....	59
Figure 5-13: Viscosity measurements at 20°C and API gravity measurements plotted versus depth for two wells in a nearby bitumen reservoir. ....	60
Figure 5-14: <i>Top:</i> Emerge™ prediction error plot and cross-plot for viscosity using the new training model, and only the standard logs as predicting attributes. In the crossplot, each color represents a different well. <i>Bottom:</i> The list of attributes with their associated validation errors. ....	62
Figure 5-15: Comparison of the three viscosity prediction methods for an example well. ....	63
Figure 5-16: Comparison of the three viscosity prediction methods for an example well. ....	63
Figure 5-17: Location of the blind test well (yellow star) relative to the study area wells. ....	65
Figure 5-18: Prediction results in the blind test well 10km north of the study area. ....	66
Figure 5-19: Viscosity measurements from all 40 training wells plotted against depth. ....	67
Figure 5-20: <i>Top:</i> Emerge™ viscosity prediction error plot and cross-plot, using all well logs plus depth as predicting attributes. For the cross-plot, each color represents a different well. <i>Bottom:</i> The list of attributes with their associated validation errors. ....	68
Figure 5-21: <i>Top:</i> Emerge™ viscosity prediction error plot and cross-plot, using log-derived seismic properties plus depth as predicting attributes. For the cross-plot, each color represents a different well. <i>Bottom:</i> The list of attributes with their associated validation errors. ....	69
Figure 5-22: Influence of depth as a viscosity predictor for three example wells. ....	70

Figure 5-23: Predicting viscosity from upscaled acoustic logs for a well with a continuous 20m reservoir interval. ....	72
Figure 5-24: Predicting viscosity from upscaled acoustic logs for a well with several interbedded shale intervals.....	73
Figure 5-25: Resistivity prediction from log-derived seismic properties for three example wells. ....	76
Figure 5-26: Histogram of all bitumen density measurements throughout the study area. ....	77
Figure A3-1: Viscosity measurements plotted against reservoir depth for the ConocoPhillips Surmont oil sands project.....	93

## List of Symbols, Abbreviations and Nomenclature

Symbol	Definition
API	API gravity, ratio of the fluid density of oil to pure water. Used for classifying oil grade.
cP	Centipoise. Unit of viscosity measurement. 1 cP = 1 mPa*s = 0.001 Pa*s Water = 1cP. Bitumen = millions of cP.
DT	Compressional sonic log. Measures P-wave slowness
DTS	Shear sonic log. Measures S-wave slowness
GR	Gamma-ray log. Measures formation radioactivity
GR-API	Unit of measurement for the gamma ray log
NMR	Nuclear Magnetic Resonance logging. Responds to hydrogen protons in formation
RHOB	Formation bulk density log
SAGD	Steam-assisted gravity drainage
SP	Spontaneous potential log. Responds to electric potential differences across rock boundaries
V <sub>p</sub>	P-wave velocity
V <sub>s</sub>	S-wave velocity

## Chapter 1 – Introduction

### 1.1 - Introduction to oil sands, heavy oil, and viscosity

Oil sands consist of unconsolidated sand that is held together by bitumen (soluble organic matter). World resources of bitumen and heavy oil are estimated to be 5.6 trillion barrels (20% to 25% of which are recoverable), compared with the remaining conventional crude oil reserves of 1.02 trillion barrels (Hein, 2006). Of the heavy oil and bitumen resources, over 80% are in Venezuela, Canada and the U.S.A. The largest oil-sands deposits are in Alberta, Canada, which account for more than 70% of world's bitumen in place (Hein, 2006). In 2001, raw bitumen production in Alberta surpassed conventional crude production for the first time, and in 2014, total oil sands production from Alberta reached 2.3 million barrels per day (Teare et. al., 2014).

The American Petroleum Institute (API) recommends the use of API gravity for classifying crude oil, defined as the ratio of the fluid density of oil to the density of pure water, taken at 60°F and 1 atmosphere of pressure as shown in Figure 1-1.

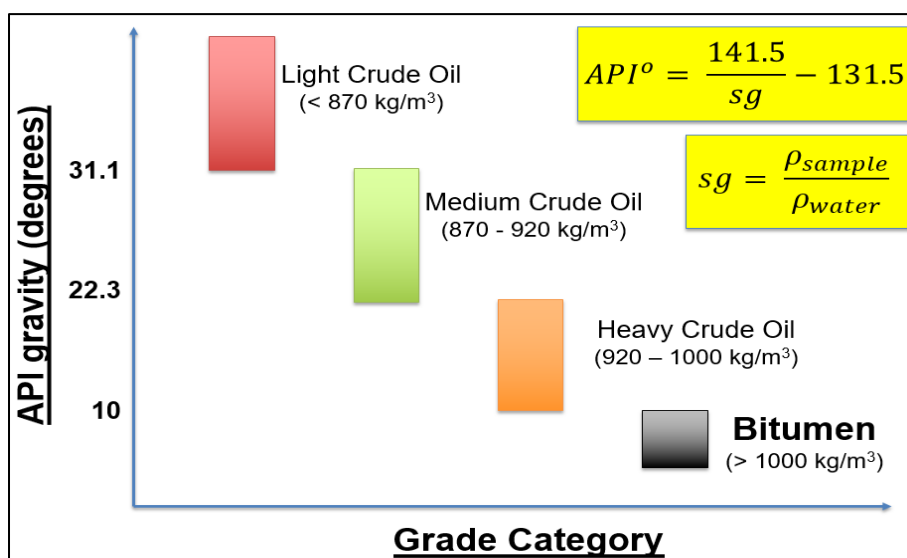


Figure 1-1: Oil grade categories, defined by their API gravity values (modified from Cheadle, 2014).

Heavy oil is defined as having 22.3°API gravity or less. Hydrocarbons of 10°API (density of water) or less are defined as bitumen. In comparison, conventional crude oils have densities greater than 22.3° API (Chopra et. al., 2010).

The fluid property that most greatly affects productivity and recovery is viscosity (Batzle et. al., 2006). The more viscous the oil, more energy needs to be injected into the system to reduce the viscosity to allow it to flow (ie. steam-assisted gravity drainage, or cyclic steam stimulation).

Viscosity is a fluid's resistance to deformation by shear stress, or more simply, a fluid's resistance to flow (McKennell, 1956). The definition of viscosity is given by Equation 1.1 and illustrated in Figure 1-2 as laminar shear of fluid between two plates. From the diagram,

$$\text{Viscosity} = \frac{\text{ShearStress}}{\text{ShearRate}} = \frac{\tau}{\left(\frac{\partial u}{\partial y}\right)} \quad \text{Units: } \frac{N/m^2}{s^{-1}} = \frac{N \cdot s}{m^2} = Pa \cdot s \quad (1.1)$$

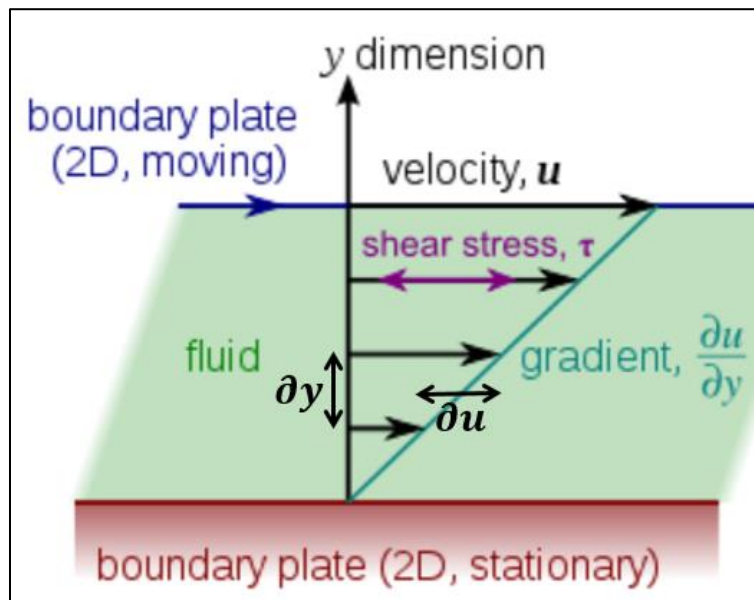


**Figure 1-2: Viscosity concept.** If a fluid is placed between two plates separated by  $1m$ , and one plate is pushed sideways with a shear stress of  $1 Pa$ , and it moves at “ $u$ ”  $m/s$ , then the fluid has viscosity of “ $u$ ”  $Pa \cdot s$  (Wikipedia user Duk, Own work, Public Domain, [https://commons.wikimedia.org/wiki/File%3ALaminar\\_shear.svg](https://commons.wikimedia.org/wiki/File%3ALaminar_shear.svg)).

viscosity is the tangential force per unit area required to move one horizontal plate with respect to another plate at a unit velocity, while maintaining a unit distance apart in the fluid.

The SI units for viscosity are  $N \cdot s/m^2$ ,  $kg/(m \cdot s)$ , or  $Pa \cdot s$ . For practical use, viscosity is usually expressed in smaller units called centipoise (cP), where:

$$1 \text{ cP} = 1 \text{ mPa} \cdot \text{s} = 0.001 \text{ Pa} \cdot \text{s} = 0.001 \frac{N \cdot s}{m^2} = 0.001 \frac{kg}{m \cdot s} \quad (1.2)$$

Conventional oil viscosity can range from 1 centipoise (cP) [0.001 Pa\*s] which is the viscosity of water, to about 10 cP [0.01 Pa\*s]. Viscosity of heavy and extra-heavy oils can range from 10 cP [0.01 Pa\*s] to 10,000 cP [10 Pa\*s]. The most viscous hydrocarbon, bitumen, is a solid at room temperature and softens readily when heated. Viscosity of bitumen can range from 10,000 cP [10 Pa\*s] to more than 1,000,000 cP [1,000 Pa\*s] (Hein, 2006). Figure 1-3 shows the logarithmic scale of viscosity subdivided by the grade category of oil, and compares it to the viscosities of typical items found in our kitchen.

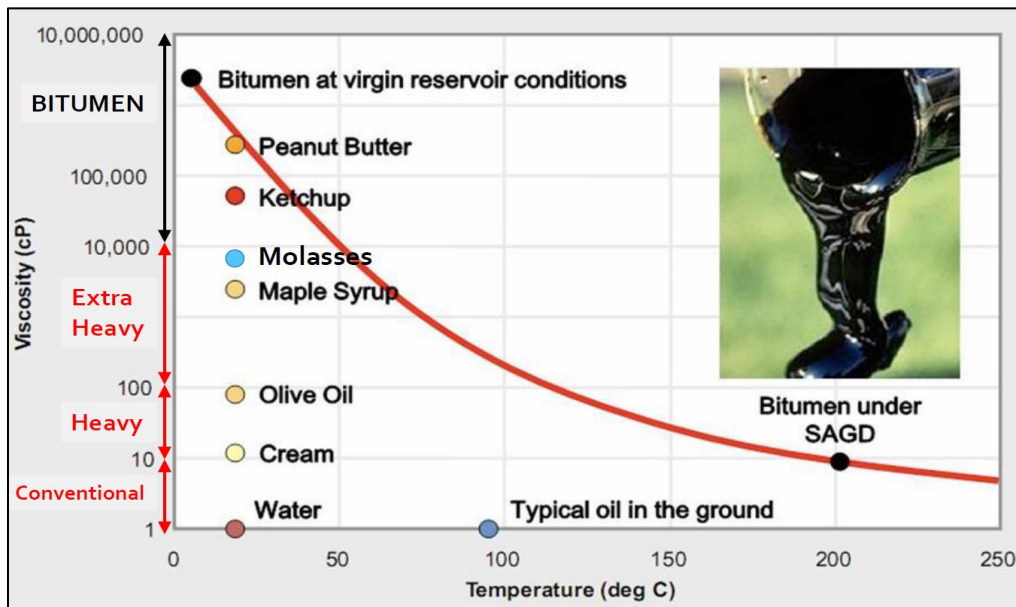


**Figure 1-3: Oil viscosities by grade category, compared to typical kitchen items. Note that viscosity has a logarithmic scale (ConocoPhillips Oil Sands website).**

The viscosity of heavy oils is mainly dependent on temperature, API gravity, and composition (Chopra et. al., 2010). One of the typical empirical relations for viscosity was developed by Beggs & Robinson (1975):

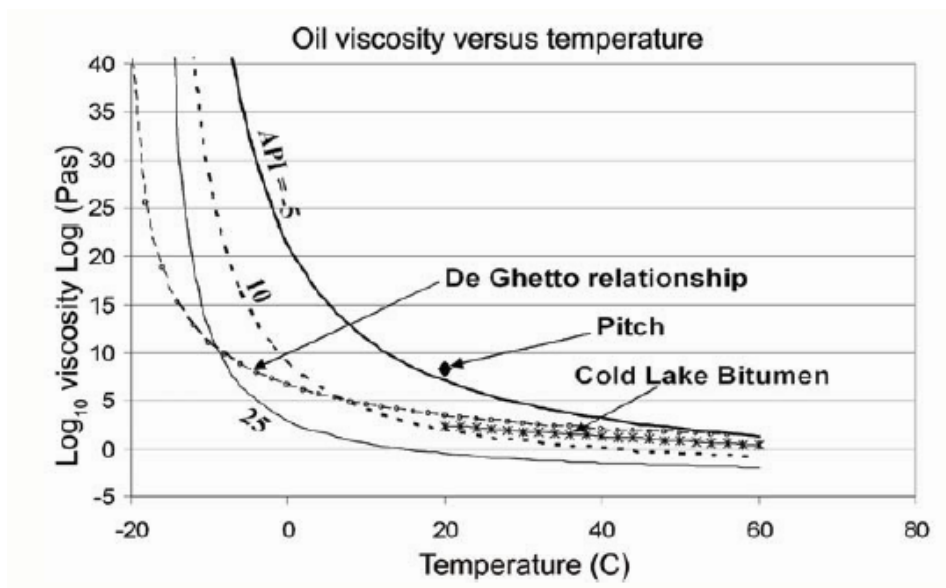
$$\text{Log}_{10}(\eta + 1) = 0.505y(17.8 + T)^{-1.163}$$

where (1.3)

$$\text{Log}_{10}(y) = 5.693 - 2.863 / \rho_0$$

Here,  $\eta$  is viscosity in centipoise (cP),  $T$  is temperature in °C, and  $\rho_0$  is the oil density at standard temperature and pressure.

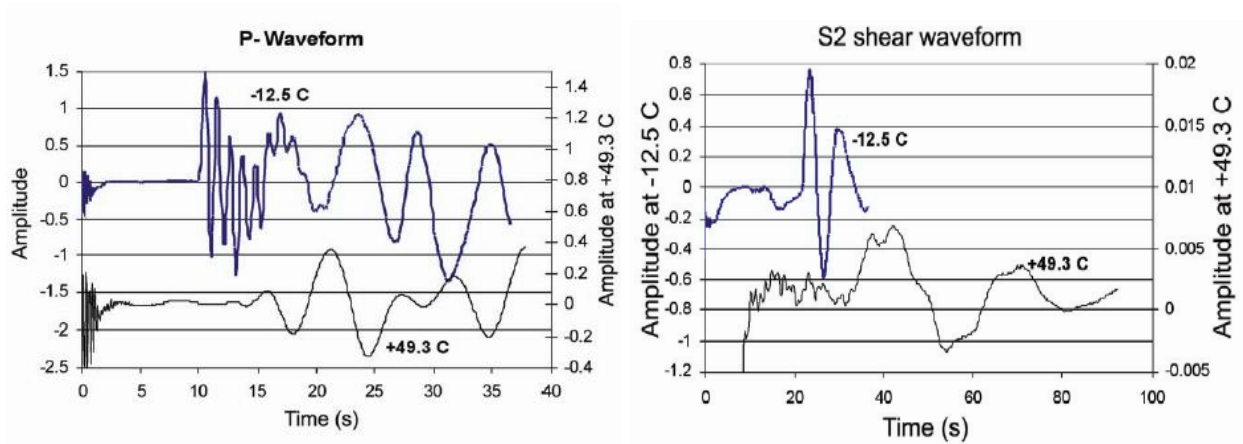
Figure 1-4 shows the temperature dependence of oil viscosity of Cold Lake bitumen plotted alongside the Beggs & Robinson (1975) relation at API values of -5, 10, and 25. (Batzle et al. 2006). This plot shows a double logarithmic relationship between reservoir temperature and oil viscosity. Clearly, increasing the temperature decreases the viscosity.



**Figure 1-4: Temperature dependence of oil viscosity using the Beggs & Robinson (1975) relation at API values of -5, 10, and 25. The heavy oil relationship from De Ghetto et al (1995) is also plotted. (Batzle et al. 2006).**

## 1.2 – Shear properties of heavy oil

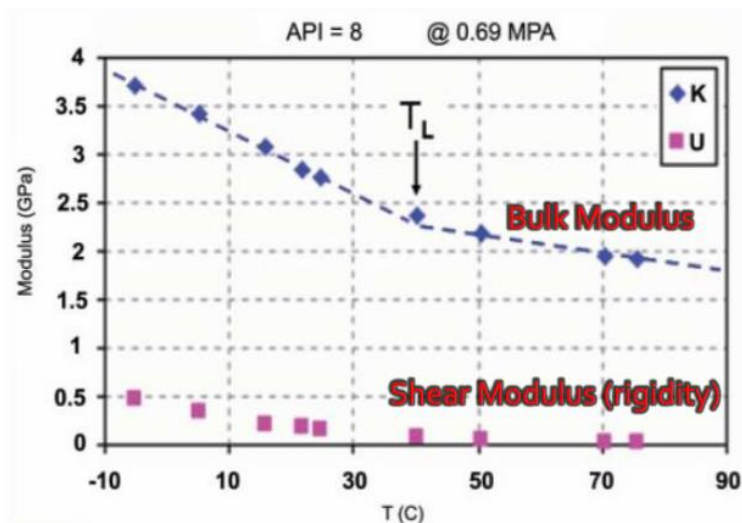
As the viscosity of heavy oil becomes high, it develops a non-negligible shear modulus (Chopra et. al., 2010). This transition can be tested in the laboratory by propagating a shear wave through the fluid sample. Batzle et. al., (2006) noticed for a very heavy oil sample (-5° API) at low temperatures (-12.5 °C), a sharp shear-wave arrival is detected (Figure 1-5 right).



**Figure 1-5: Left – Ultrasonic compressional waveforms measured through a very heavy oil (API = -5) at -12.5°C and 49.3°C. Right – Ultrasonic shear waveforms in the same heavy oil at the same temperatures. Notice how in both cases, the waveform is both delayed and attenuated at higher temperature (Batzle et. al., 2006).**

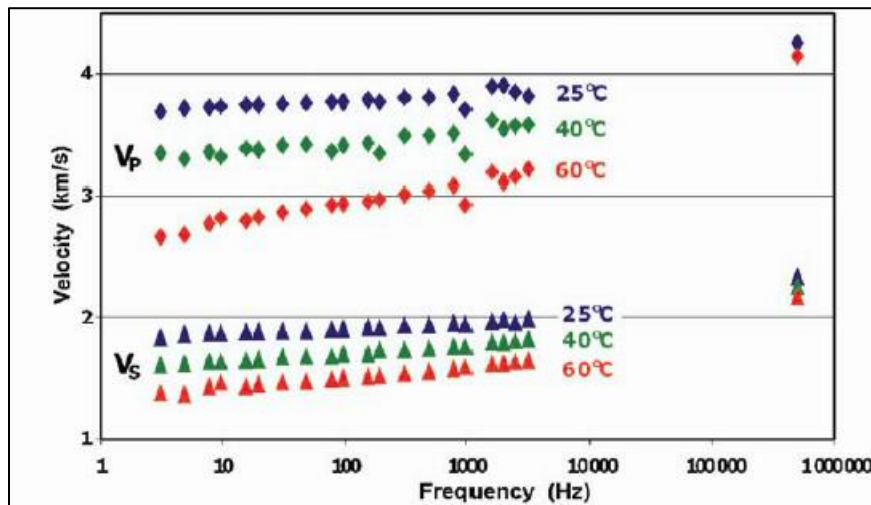
At this temperature, the oil is almost a solid and therefore has a shear modulus. As the temperature is increased and the heavy oil becomes more fluid-like, the shear-wave velocity decreases as well as its amplitude.

Figure 1-6 shows bulk and shear modulus lab measurements for an 8° API heavy oil (Han et. al., 2008). At low temperatures, both bulk and shear moduli are present, but above a certain temperature (called the liquid point), the shear modulus vanishes and the bulk modulus changes slope. This analysis shows how heavy oil behaves like a viscoelastic material (semisolid) at lower temperatures (high viscosities), and a viscous fluid at higher temperatures (Han et. al., 2008).



**Figure 1-6: Bulk modulus and shear modulus for an API 8° heavy oil. Above a certain temperature (called the liquid point), the shear modulus vanishes and the bulk modulus changes slope (Han et. al., 2008).**

We have so far been discussing the shear properties of heavy oil by itself. However, well logs and seismic waves sample the heavy-oil saturated rock, and there is strong frequency-dependence between the types of measurement. Figure 1-7 shows  $V_p$  and  $V_s$  measurements of a Texas heavy oil saturated carbonate as a function of frequency at different temperatures (Batzle



**Figure 1-7: Frequency dependence of velocity for a heavy oil saturated carbonate rock from Texas. Velocity decreases with increasing temperature. Also, higher frequencies (well logs ~ 10,000Hz) measure higher velocities than lower frequencies (seismic ~ 10-100Hz). (Batzle et al 2006).**

et. al., 2006). Note the frequency dependence (dispersion) of both the P and S wave velocities, which becomes more pronounced as temperatures increase. These observations clearly show how velocities measured in the seismic band of 10–100 Hz do not agree with standard acoustic log data (~10,000 Hz) nor with lab-measured ultrasonic (MHz-range) data (Batzle et. al., 2006).

This frequency-dependence (dispersion) of velocity is directly related to the attenuation (Q factor) of the material. The Q factor can be related to the real and complex parts of the dynamic shear modulus, as explained by Behura et. al. (2007), summarized below.

For a viscoelastic material subjected to a sinusoidal varying strain, the strain  $\epsilon$  and resulting stress  $\sigma$  can be represented by:

$$\epsilon = \epsilon_0 e^{-i\omega t} \quad (1.4)$$

and

$$\sigma = \sigma_0 e^{-i(\omega t - \delta)} \quad (1.5)$$

where  $\omega = 2\pi f$ ,  $i = \sqrt{-1}$ , and  $\delta$  is the phase lag. For an elastic material, the resulting stress is instantaneous and so  $\delta=0$ . For a purely viscous fluid,  $\delta$  approaches  $\pi/2$ , whereas for a viscoelastic body,  $\delta$  lies in between the two limits. The complex dynamic shear modulus is given by:

$$\tilde{G} = \frac{\text{stress}}{\text{strain}} = G' + iG'' \quad (1.6)$$

where

$$G' = \frac{\sigma_0 \cos \delta}{\epsilon_0} \quad (1.7)$$

and

$$G'' = \frac{\sigma_0 \sin \delta}{\epsilon_0} \quad (1.8)$$

$G'$  is the real part and is called the storage modulus, which represents the elastic component of

the material.  $G''$  is the imaginary part and is called the loss modulus, which represents the viscous fluid component.

Integrating the out-of-phase component of stress over an entire cycle gives the energy lost per cycle, and integrating the in-phase component of stress over a 1/4 full cycle gives the maximum energy stored per cycle. As shown in Behura et. al. (2007), these integrations allow us to derive  $Q$  as the ratio of the real and imaginary components of the complex shear modulus:

$$Q = \frac{1}{\tan \delta} = \frac{\text{energy}}{\text{energy loss}} (\text{per frequency cycle}) = \frac{G'}{G''} \quad (1.9)$$

Behura et. al., (2007) performed lab measurements of  $G'$  and  $Q$  (inversely proportional to attenuation) of a heavy-oil saturated carbonate sample from Uvalde, Texas at varying temperatures within the seismic frequency band. Their results are shown as color scaled three-variable plots in Figure 1-8.  $G'$  and  $Q$  show a moderate dependence on frequency but are strongly influenced by temperature.  $G'$  monotonically decreases with increasing temperature. As for the quality factor,  $Q$  increases with frequency and initially decreases with temperature.

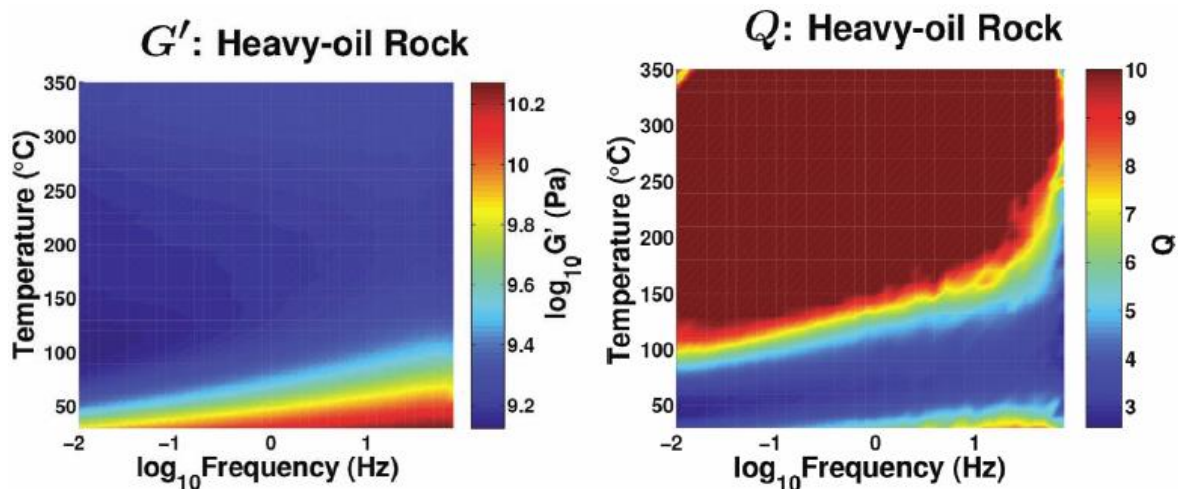


**Figure 1-8: (Left): Storage modulus – temperature – frequency relation from lab measurements of a heavy oil saturated carbonate from Uvalde, Texas. (Right): Quality factor – temperature – frequency relation of the Uvalde heavy oil saturated carbonate. Measurements were made at temperature increments of 10°C and frequency increments of 0.1 on the Log<sub>10</sub> scale (Behura et al 2007).**

However, at higher temperatures, the  $Q$  trend reverses and begins to increase with increasing temperatures. A likely explanation for this behavior is due to a loss of lighter hydrocarbon components at high enough temperatures.

### 1.3 – Previous studies of estimating heavy oil viscosity

Several engineering-based empirical methods have been published to predict heavy oil viscosity, such as the Beggs & Robinson (1975) relationship in Equation 1.3. However, the author is only aware of two published methods where geophysical technology has been used to predict heavy oil viscosity. Both of these methods are briefly summarized in this section.

Vasheghani & Lines (2012) developed a methodology to estimate viscosity from cross-well seismic data between two wells by using travelttime tomography, attenuation tomography, and rock physics (Figure 1-9). Since heavy oil is viscoelastic, the seismic energy attenuates with propagation distance which can be measured in terms of the seismic quality factor  $Q$ . They

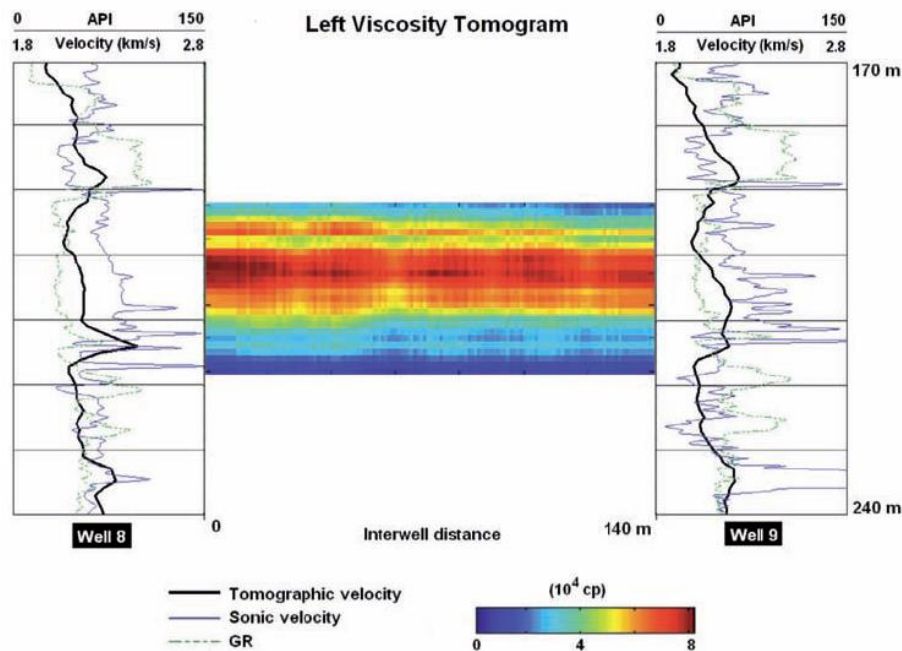


Figure 1-9: Viscosity tomogram from Vasheghani & Lines (2012).

related seismic Q to fluid viscosity in a two-stage process: First, they generated Q-tomograms from the cross-well data using attenuation tomography with the frequency shift method. Secondly, they related Q to fluid viscosity through the BISQ equations (Dvorkin et. al., 1994) to create an estimated viscosity cross-section between the two study wells (Figure 1-9). There is ambiguity, however, because for every Q value, two viscosity values can be calculated through the BISQ equations. Also, there was no real viscosity data available for the authors to validate their results against. Nevertheless, the work of Vasheghani & Lines (2012) demonstrates that seismic data has potential to be used to estimate fluid viscosity in heavy oil reservoirs.

The second published method of estimating viscosity using geophysical technology is through NMR well logging. Nuclear magnetic resonance (NMR) tools measure transverse relaxation times ( $T_2$ ) of protons in rocks, and can be used to determine pore size distribution (Rider & Kennedy 2011). A secondary parameter measured through NMR logging is the Hydrogen Index (HI), which is a result of the signal amplitude being proportional to the amount of hydrogen in the pore spaces (Rider & Kennedy 2011). Bryan et. al. (2005) demonstrated that lab measured viscosities showed a correlation with these two NMR parameters ( $T_2$  and HI). They showed that with increasing viscosity,  $T_2$  decreased, and at high viscosities  $T_2$  became less sensitive to viscosity changes. However, increasing viscosities caused the decreasing HI to become more sensitive to viscosity change at high viscosities. Based on these findings, Bryan et. al. (2005) developed a new empirical relationship between the two NMR parameters and viscosity, and adjusted it to provide the best possible fit to the database they were using, which had oil viscosities from less than 1 cP to 3,000,000 cP. More studies (Sun et. al., 2007; Kantzas, 2009) have further developed on the NMR-viscosity correlation in the lab, all for the purpose of

developing a method to use downhole NMR measurements to predict viscosity down the wellbore.

Figure 1-10 shows a heavy oil example from the Athabasca oil sands where lab viscosity measurements were available from multiple samples down the wellbore. The empirical NMR-viscosity relationship was used to generate a pseudo-viscosity log that showed fairly good agreement with the lab viscosity measurements which ranged from 30,000 to 300,000 cP (Alboudwarej et. al., 2006).

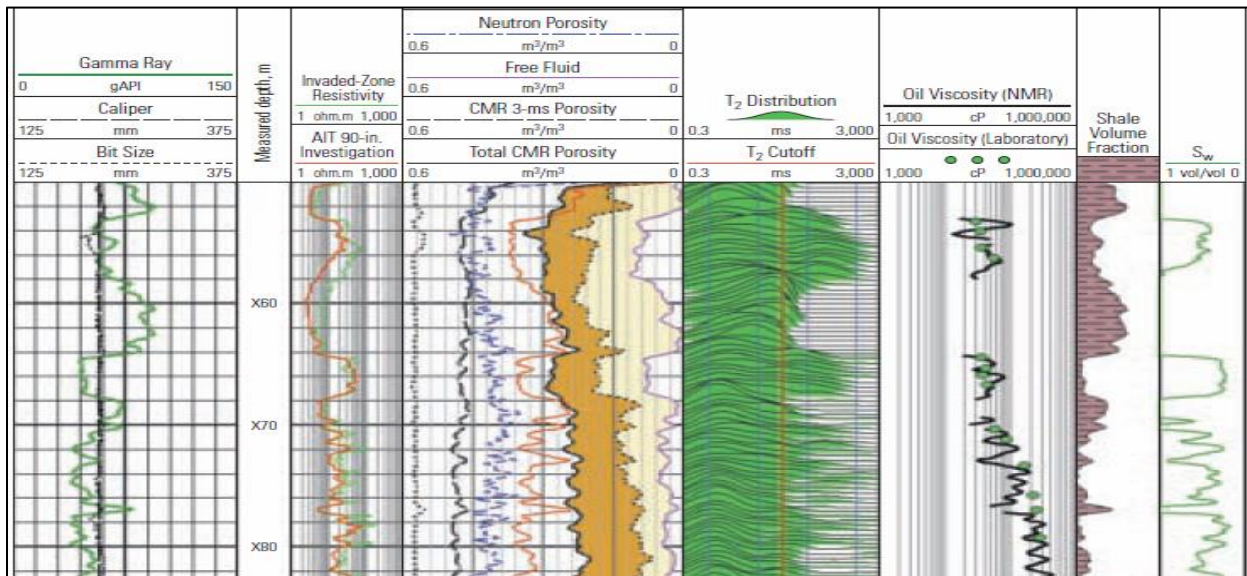


**Figure 1-10: A pseudo-viscosity log produced from two NMR logging parameters (T<sub>2</sub> and HI), calibrated to laboratory viscosity measurements from the Athabasca oil sands (Alboudwarej et. al. 2006).**

#### 1.4 – Motivation and goals of this thesis

Reservoir fluid PVT (pressure-volume-temperature) properties, in particular fluid viscosity, are crucial factors in selection of a recovery technique. For example, cold heavy-oil production with sand (CHOPS) has been applied to reservoirs in Canada with oil viscosities ranging from 50 to 15,000 cP (Alboudwarej et. al., 2006). However, recovery techniques cannot

be chosen solely based on viscosity ranges. Many factors must be taken into consideration such as fluid properties, formation continuity, rock mechanics, drilling technology, completion options, production simulation, surface facilities, reservoir thickness, and expected recovery and production rates (Alboudwarej et. al., 2006). However, having an estimate of oil viscosity of a reservoir beforehand will greatly aid in choosing the best recovery technique and determining how to optimally produce the reservoir.

The only way to achieve a high degree of certainty on the viscosity of a heavy oil or oil sands reservoir is by measuring the viscosity in the lab from core samples or wellhead oil samples, which is an expensive undertaking (Miller et. al., 2006). It has been mentioned that the signal from the NMR logging tool can be correlated to viscosity, however NMR logs are also expensive and not commonly run. It would therefore be very useful to have a method to reliably estimate viscosity using only standard well logs.

Donor Company has generously provided the author with lab viscosity measurements from one of their major oil sands projects. The goal of this thesis is to investigate if a reasonable correlation can be established between the measured viscosity values and the available well log data, so that viscosity can be blindly predicted in nearby wells with a standard suite of well logs.

## Chapter 2 – Well Logging Principles

### 2.1 – Overview of the well log measurement

The continuous recording of a geophysical parameter down a borehole produces a geophysical well log, more commonly referred as a well log. The logging tool is lowered down the borehole by a spool and cable and measures different physical properties of the rocks as it is pulled back up (Figure 2-1). For example, gamma-ray logs measure the natural radiation of the formation, density and neutron logs calculate the porosity by measuring bulk density and hydrogen concentrations, respectively, and resistivity logs measure the resistivities of the fluids in the formation. From this data, geoscientists can infer lithological successions, depositional environments, and fluid characteristics, which allow them to make predictions on where petroleum accumulations are likely to exist. Once a reservoir is found, geoscientists and

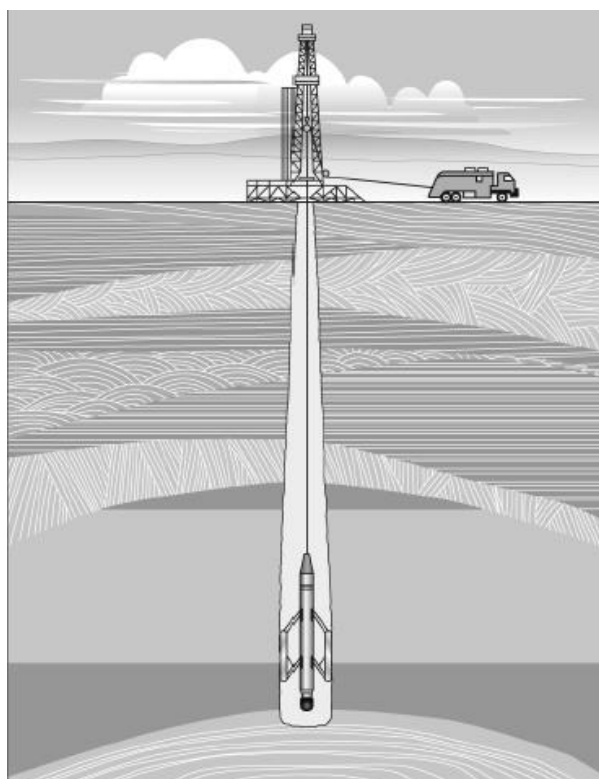


**Figure 2-1: The elements of well logging: the measurement tool (sonde) in a borehole, the wireline pulled by a spool and cable, and the logging truck (Ellis & Singer, 2008).**

engineers make use of the well-log data to evaluate fundamental reservoir characteristics such as porosity, permeability, reservoir thickness, and fluid saturation to predict how much oil can be recovered and whether or not it is economic to do so.

The remainder of this chapter gives a basic overview of the principles of the well log measurements most relevant to this thesis, which are: gamma ray, resistivity, spontaneous potential, NMR, density, and sonic logs.

## **2.2 – Overview of the total gamma ray tool**

The total gamma-ray tool (GR) responds to the total natural radioactivity of a formation due to the decay of three radioactive isotopes:  $^{40}\text{K}$  (potassium),  $^{232}\text{Th}$  (thorium), and  $^{238}\text{U}$  (uranium). It is essentially a clay detector, because clay minerals (such as illite and smectite) have significant amounts of potassium (Rider & Kennedy 2011).

The tool consists of a highly sensitive gamma ray detector in the form of a scintillation counter. The scintillation counter is composed of a sodium iodide crystal backed by a photomultiplier (Ellis & Singer 2008). When a gamma ray strikes the crystal a small photon of energy is emitted (due to the photoelectric effect). This flash is too small to be measured using conventional electronics. Instead, it is amplified by a photomultiplier which outputs an electric pulse for each incident gamma-ray (Ellis & Singer 2008). Since the emitted photon and the amplified electric pulse is proportional to the energy of the incident gamma ray, the final current from the scintillation counter is also proportional to the energy of the incident gamma ray from the formation (Ellis & Singer 2008). A schematic of this process is shown in Figure 2-2.

The gamma-ray log is reported in pseudo-units called GR-API. The GR-API unit is defined empirically by calibrating to a reference well at the University of Houston, which is

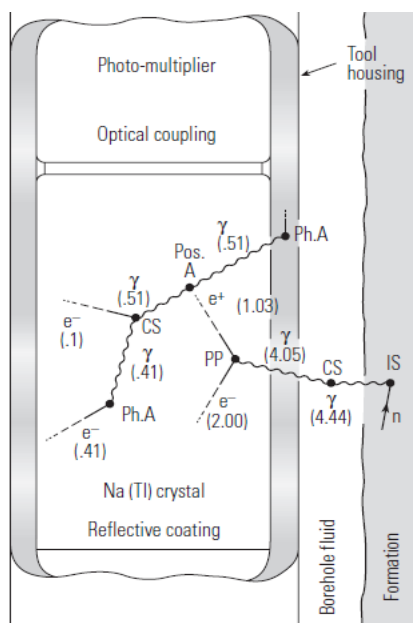


**Figure 2-2: The life of a single gamma ray, which is emitted in the formation and ultimately detected by a NaI detector in the borehole (Ellis & Singer 2008).**

made of large blocks of precisely known radioactivity's ranging from very low to very high. The scale is designed such that an "average shale" reads 100 GR-API (Rider & Kennedy 2011). *Note that the GR-API unit is completely unrelated to API gravity as discussed in chapter 1.*

### 2.3 – Overview of the induction resistivity tool

The induction resistivity tool measures the conductivity of the invaded formation and inverts it to obtain the resistivity value. The main application of the resistivity log is that it provides information about the pore fluids (ie. if it is water or hydrocarbon bearing).

The tool consists of a transmitter coil and a receiver coil, illustrated in Figure 2-3. A high frequency alternating current (AC) of about 20,000 Hz is applied to the transmitter coil, which generates a magnetic field around it and induces secondary currents in the formation. These currents flow in coaxial loops around the tool and create their own secondary magnetic field, which induces currents in the receiver coil.

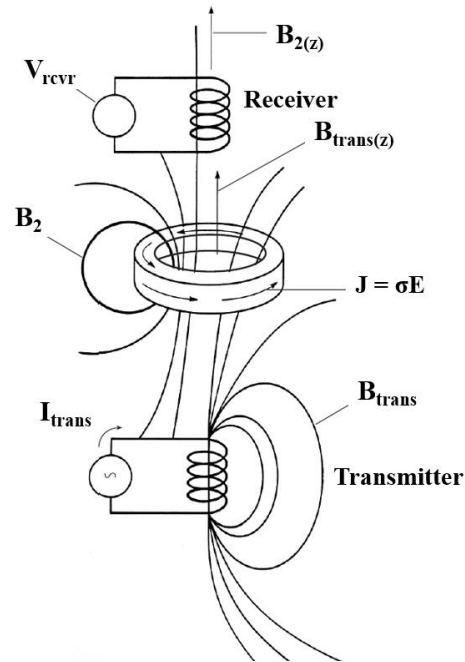


**Figure 2-3: The principle of the induction tool. The vertical component of the magnetic field from the transmitter coil,  $B_t$ , induces ground current loops,  $J$ , in the formation. These current loops in the conductive formation produce an alternating magnetic field,  $B_2$ , the vertical component of which is detected by the receiver coil (Ellis & Singer 2008).**

The voltage detected at the receiver is proportional to the conductivity of the formation and to the square of the applied AC frequency, as given by (Ellis & Singer 2008):

$$V_{rcvr} \propto -\frac{\partial(B_2)}{\partial t} \propto -\omega^2 \sigma I_0 e^{-i\omega t} \quad (2.1)$$

where  $(B_2)_z$  is the vertical component of the secondary magnetic field in Teslas,  $\omega$  is the transmitter alternating current frequency in Hz,  $\sigma$  is the formation conductivity in mSiemens/m,  $I_0$  is the transmitter current flow in Amperes, and  $i = \sqrt{-1}$ .

As the hole gets drilled, the drilling mud can displace formation fluids in a circumferential zone near the open borehole. This process is called invasion, which is illustrated in Figure 2-4. The borehole wall acts like a filter, allowing the mud filtrate to invade the pores immediately adjacent to the hole, and leaving the solid portion behind to coat the hole with “mud cake.” Therefore, the completely invaded zone (“flushed zone”) will have different resistivity

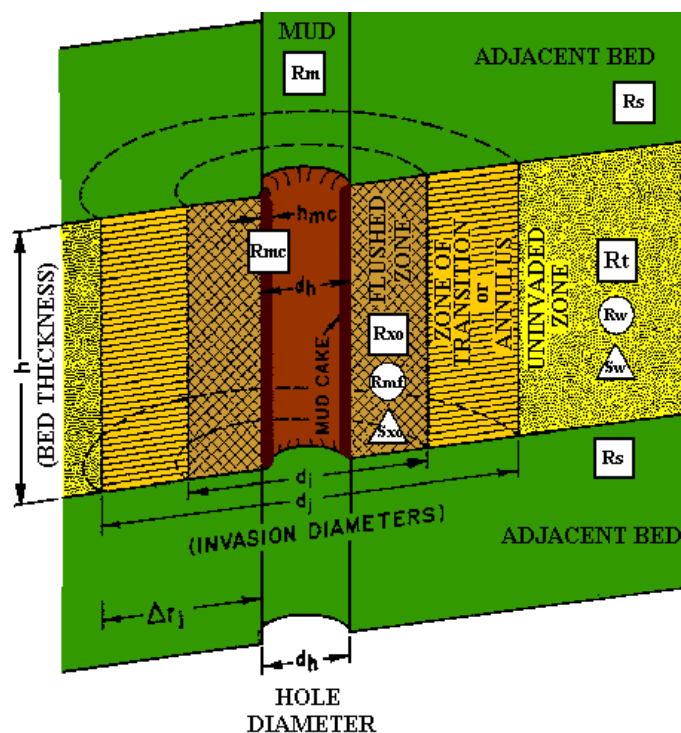


Figure 2-4: Borehole mud invasion profile: “step model” of invasion (adapted from Schlumberger 2009)

**Nomenclature:**

**Borehole:**

**$R_m$**  = Resistivity of mud

**$R_{m c}$**  = Resistivity of mud cake

**Flushed (Invaded) Zone:**

**$R_{m f}$**  = Resistivity of mud filtrate

**$R_{XO}$**  = Resistivity of flushed zone

**$S_{XO}$**  = Water Saturation of flushed zone

**Uninvaded or Virgin Zone:**

**$R_t$**  = True resistivity of formation

**$R_w$**  = Resistivity of formation water

**$S_w$**  = Formation water saturation

**$R_s$**  = Resistivity of adjacent (shoulder) bed

**$d_i$**  = Diameter of invasion

**$d_h$**  = Borehole diameter

**$h$**  = Bed thickness

characteristics than the uninvaded formation which is further away from the hole. Between these two regions is a transitional zone of partial invasion (Schlumberger 2009).

The induction tool typically measures three resistivity curves: deep, medium, and shallow. The deep curve measures the uninvaded zone ( $R_t$ ), the medium curve measures the transition zone, and the shallow curve measures the invaded zone  $R_{XO}$  (Rider & Kennedy 2011).

In oil sands settings, invasion is minimal because of the highly viscous bitumen, and so the three resistivity curves track each other closely (Cheng et. al., 2015).

## 2.4 – Overview of the spontaneous potential (SP) tool

The spontaneous potential (SP) log is a measurement of the natural potential differences between an electrode in the borehole and a reference electrode at the surface. It can be used for well-to-well correlation (though not as good as the gamma ray), estimating formation water

resistivity ( $R_w$ ), and as a permeability indicator (Rider & Kennedy, 2011).

Three factors are necessary to achieve an SP response: conductive drilling fluid in the borehole, a porous and permeable bed surrounded by an impermeable formation, and a salinity difference between the borehole fluid and the formation fluid (Rider & Kennedy 2011).

Consider a porous and permeable sandstone penetrated by a borehole, as shown in Figure 2-5. The mud filtrate is less saline than the sandstone formation water, therefore the mud filtrate becomes negatively charged resulting in a negative SP deflection. Above the sandstone in the semi-permeable shale, the borehole and formation salinities are similar and there is no SP deflection. The greater the SP deflection, the greater the salinity contrast between the mud filtrate and the formation water (Rider & Kennedy 2011).

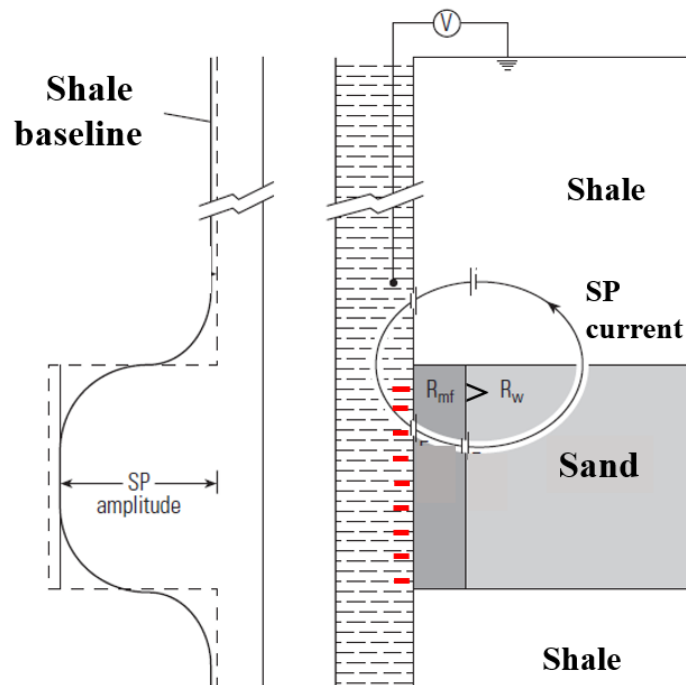


**Figure 2-5: A schematic representation of the development of the spontaneous potential signal in a borehole (modified from Ellis & Singer 2008).**

Quantitatively, the SP can be used to estimate formation water resistivity using the relationship between the resistivity and ionic activity (Rider & Kennedy 2011):

$$SP \cong -K \log \frac{R_{mf}}{R_w} \quad (2.2)$$

where  $SP$  is the reading in mV,  $R_{mf}$  and  $R_w$  are the mud filtrate and formation water resistivities in ohm\*m, respectively, and  $K$  is a temperature constant ( $65 + 0.24(T^\circ\text{C})$ ).

## 2.5 – Overview of the density logging tool

The formation density log measures the bulk density of the formation  $\rho_b$ . Its main use is to calculate the total porosity of the formation. It is also useful in the detection of gas-bearing formations, recognition of evaporite minerals, and for generating synthetic seismograms (in conjunction with the P-wave sonic log).

The tool consists of a radioactive source, a short range detector, and a long range detector, as shown in Figure 2-6. The short range detector is placed about 15 cm from the source, and the long range detector is between 30 and 45 cm from the source. The radioactive source emits gamma-rays of medium energy (0.2 to 2.0 MeV), which bombard the formation and

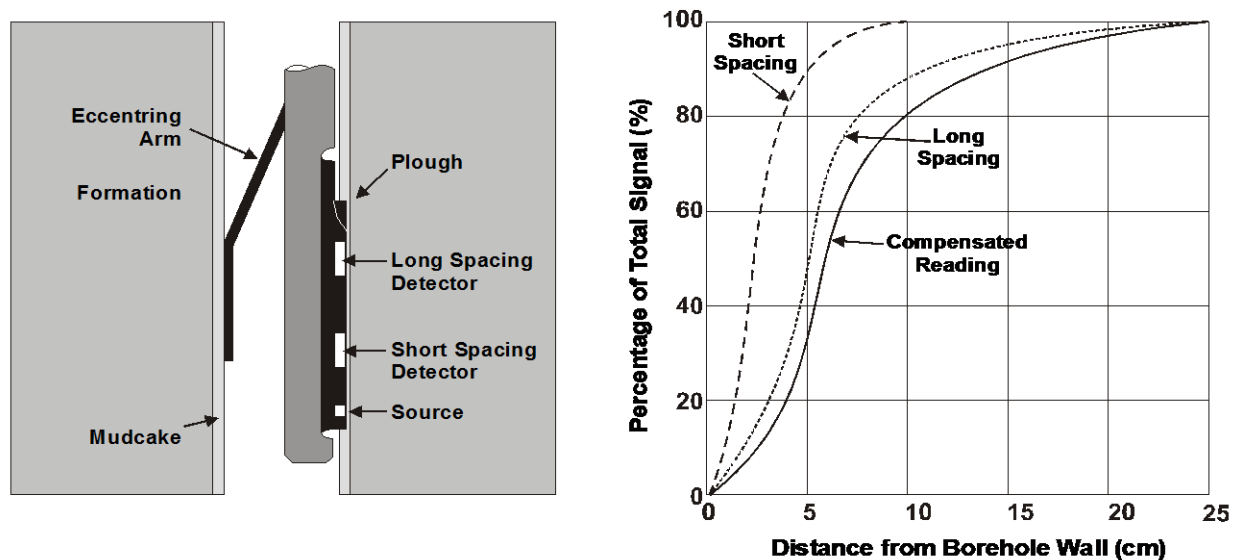


**Figure 2-6: Schematic diagram of a density tool (left), and a representation of typical depths of investigations for the density tool (right) (modified from Rider & Kennedy 2011).**

undergo Compton scattering by interaction with the electrons inside the atoms of the formation. This process reduces the energy of the gamma-rays and scatters them in all directions. The flux of the gamma-rays returning to each of the two detectors is attenuated by an amount dependent upon the electron density of the formation. Formations with a high bulk density have a high electron density, which significantly attenuates the gamma rays to a low count rate being recorded at the detectors. Formations with a low bulk density have a low electron density, which attenuates the gamma-rays less resulting in a higher count rate (Rider & Kennedy 2011).

The electron density in a pure substance is directly related to its bulk density, described by the relationship (Ellis & Singer 2008):

$$n_e = \frac{N_A Z}{A} \rho_b \quad (2.3)$$

where  $n_e$  is the electron number density of the substance in electrons/cm<sup>3</sup>,  $N_A$  is Avogadro's number (6.022x10<sup>23</sup>),  $Z$  is the atomic number,  $A$  is the atomic weight in g/mol, and  $\rho_b$  is the bulk density of the material in g/cm<sup>3</sup>. The gamma ray count at the detectors depends on the electron density (related to the bulk density), as per the general attenuation relation (Ellis & Singer 2008):

$$N = N_0 e^{-n_e \sigma x} \quad (2.4)$$

where  $N$  is the counting rate of the detector at a distance  $x$  cm from the source,  $N_0$  is the natural gamma-ray flux if there was no attenuation, and  $\sigma$  is the cross section for Compton scattering.

Figure 2-6 (right) also shows that over 80% of the signal from the short range detector comes from within 5 cm of the borehole wall, which is mainly mudcake. For the long spacing detector, about 80% of its signal comes from within 10 cm of the borehole wall. This is the shallowest depth of investigation of all the standard logs (Rider & Kennedy 2011).

If the tool is flush against the borehole wall and there is no formation attenuation in the near wellbore region, both detectors should give the same density. When the detectors measure different densities, the difference is called the density correction, which arises due to mudcake or mud filtrate invasion around the detectors. The density correction is applied to the raw measurement and typically ranges from 0 to 1 g/cm<sup>3</sup>. In LAS files, the density correction curve is usually available as a DRHO, ZCOR, or DENCOR curve name. Noisy behavior on the density correction curve can indicate poor wellbore conditions, and potential for erroneous density values (Rider & Kennedy 2011).

## **2.6 – Overview of the sonic logging tool**

The sonic (or acoustic) log measures the slowness (reciprocal of velocity) of an acoustic wave through a formation by recording the time for a pulse of sound to travel a known distance through it. Sonic logs are primarily used for generating synthetic seismograms (in combination with the density log) so that seismic data, measured in time, can be tied to wells, measured in depth.

Three principal acoustic waves are detected in sonic logging: the compressional or P-wave, the shear or S-wave, and the Stoneley wave, as shown in Figure 2-7 (Ellis & Singer 2008). Compressional or P-waves are high in energy, low in amplitude, and caused by particle motion in the direction of propagation. Shear waves or S-waves are associated with particle movement perpendicular to the direction of propagation, and arrive after the compressional waves. The Stoneley wave arrives after the shear wave, has less energy but a high amplitude which varies with frequency, and is a complex type of surface wave. The Stoneley wave exists as a tube wave

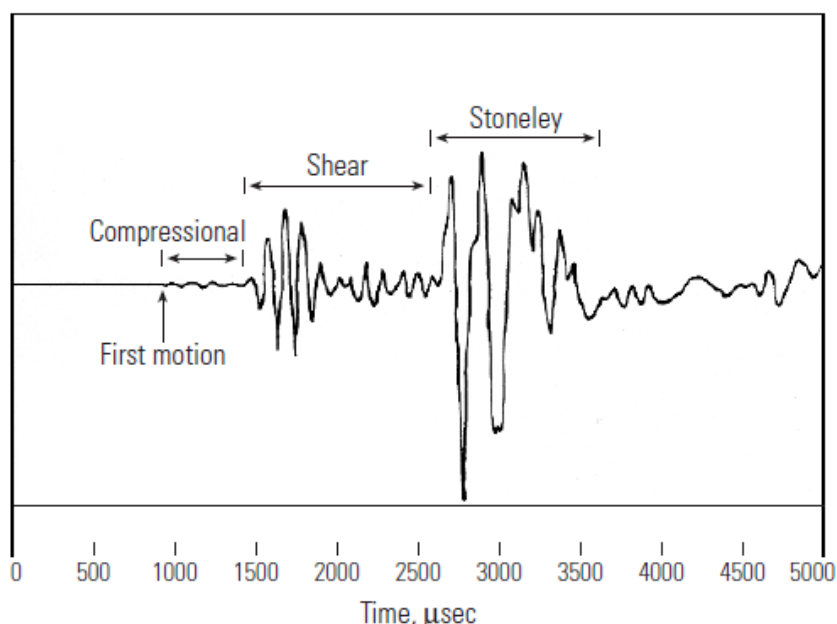


**Figure 2-7: A typical acoustic waveform recorded in a borehole. Three distinct arrivals are indicated (Ellis & Singer 2008).**

in the cylindrical environment of the borehole (Rider & Kennedy 2011).

Older sonic tools (pre-1985) could measure only the P-wave arrival, but with the updated technology of dipole sources, receiver arrays, and downhole digitization, the modern (array) tools used today measure the full waveforms which provide the compressional, shear, and Stoneley wave arrival times (Close et. al., 2009). The principles of the older tools will not be discussed here.

The designs of sonic tools vary between logging companies, but all use an array of receivers (between 8 and 13), and dipole transmitter sources. At each depth increment, the transmitter emits a series of pulses at a frequency range exceeding 10,000 Hz. The refracted P- and S-waves, and the borehole Stoneley waves are recorded by the receiver array (Figure 2-8). The depth being sampled is at the midpoint of the array (Rider & Kennedy 2011).

Various signal processing algorithms exist to extract the slowness values from the series

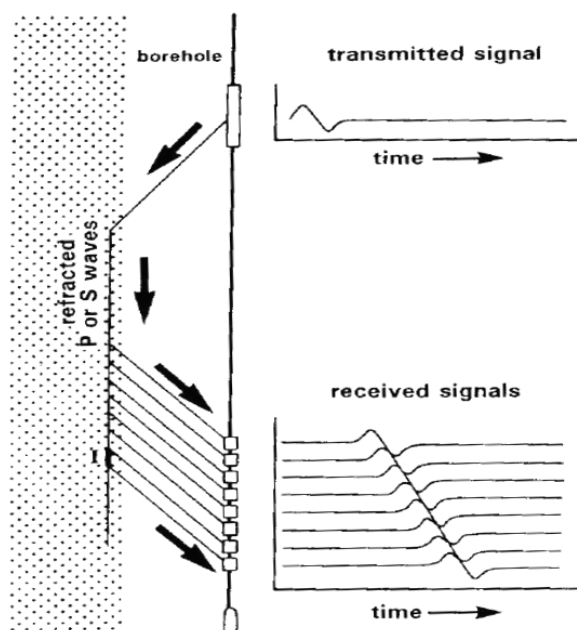
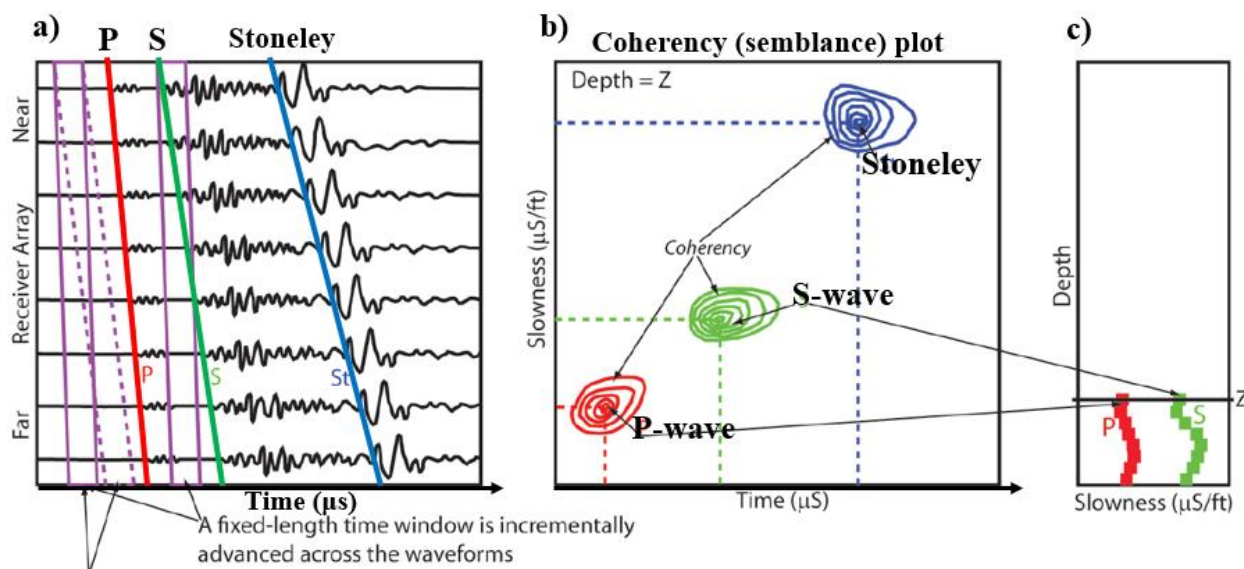


**Figure 2-8: Simplified schematic of a sonic array logging system. At each sample depth, a series of transmitter-common readings are made at different receiver offsets, where the waveforms are digitally recorded by the receivers (modified from Smith et. al., 1991).**

of waveforms, which make use of coherency methods. As an example, Schlumberger uses a method called Slowness Time Coherency (STC), where a fixed-length time window is incrementally advanced across the waveforms (Figure 2-9a). At each increment, the time-window is rotated through the array in steps of increasing slowness (or increasing moveout) and a coherency value is computed which represents how closely each moveout matches the waveform. The coherency function is represented on the Z-axis of a slowness vs. time coherence map for each measurement depth (Figure 2-9b). The coherence peaks are then plotted as points on a log at each given depth (Figure 2-9c). Repeating this process at all depths is how P-wave and S-wave slowness logs are created (Close et. al., 2009).

Computing the S-wave slowness values is less robust than calculating P-wave slowness due to the problem of picking the shear-wave arrivals. In practice, the recorded waveforms are not as clean as Figure 2-9a shows, and while the P-wave arrival is obtained from the first break



At each increment the window is rotated through the array in steps of increasing slowness and the coherency calculated at each step

**Figure 2-9: a) An array of waveforms showing increasing moveout from near to far receivers. b) A slowness-time map in which coherent peaks correlate to different wave components. c) A continuous log is built from repeating steps (a) and (b) at each depth measurement point (modified from Close et. al., 2009).**

of each trace, the shear wave arrival is embedded in the mix of earlier arrivals. This introduces more uncertainty into the S-wave slowness calculation (Lines et. al., 2010).

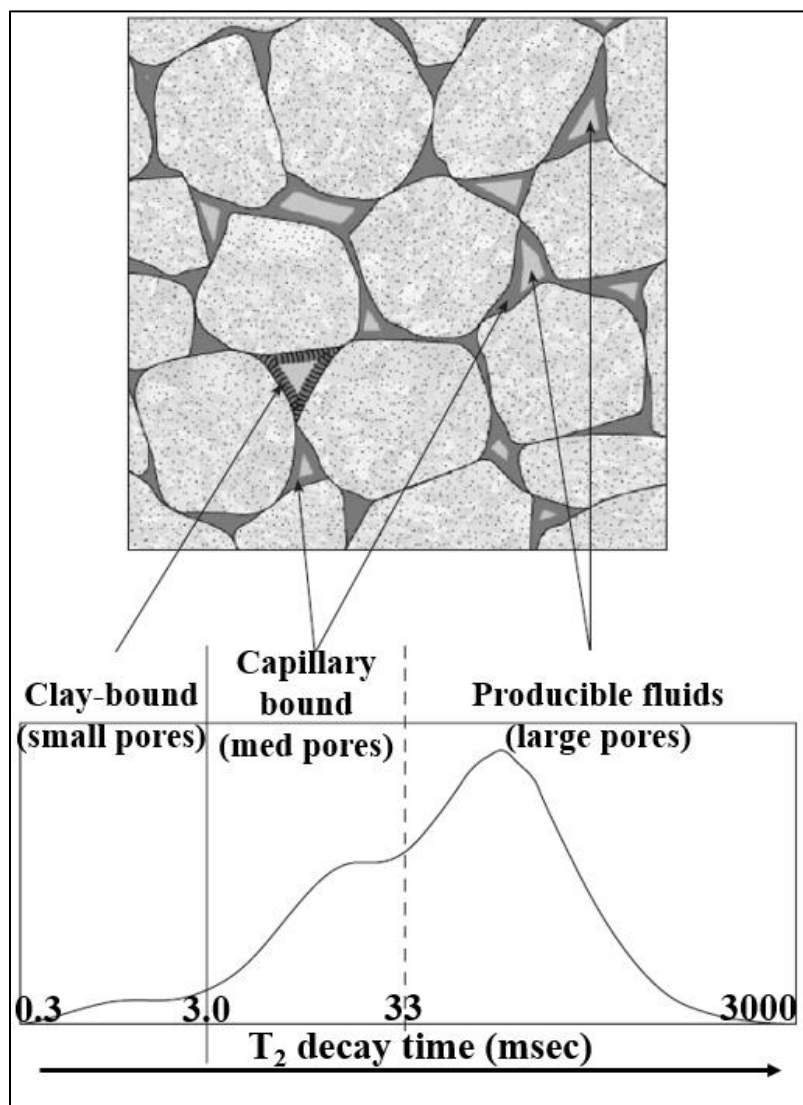
However, shear wave information has become critical in the last two decades for AVO analysis, calculating reservoir geomechanical properties, detailed permeability analysis, and even quantifying wellbore damage (Rider & Kennedy 2011). Despite the higher uncertainty in measuring shear wave slowness, it is typically far superior to acquire a shear log instead of trying to predict it from the compressional sonic log (Close et. al., 2009).

## 2.7 – Overview of Nuclear Magnetic Resonance (NMR) logging

Unlike conventional logging measurements (ie. acoustic, density, and resistivity), which respond to both the rock matrix and fluid properties and are strongly dependent on mineralogy, NMR-logging measurements respond to the presence of hydrogen protons, which occur primarily in pore fluids. NMR (nuclear magnetic resonance) provides information about the quantities of fluids present, the properties of these fluids, and the pore size distributions containing these fluids (Rider & Kennedy 2011).

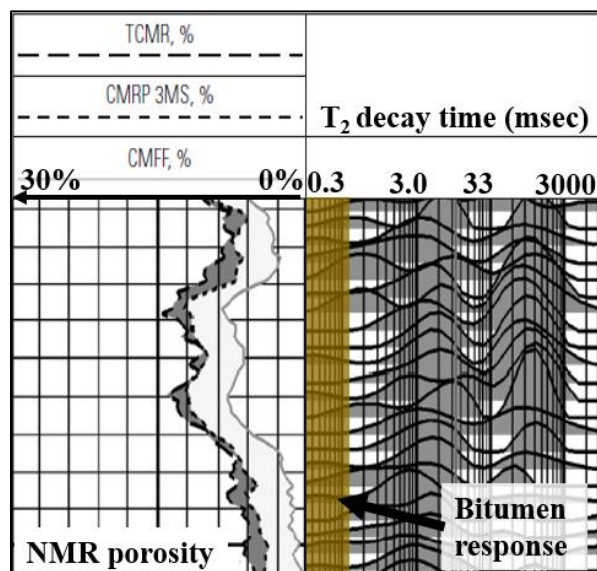
The NMR measurement is extremely sensitive and complex. The heart of the measurement involves measuring the characteristic decay time of protons, called the  $T_2$  *relaxation time*, by emitting a sequence of electromagnetic pulses at the correct Larmor frequencies (Dunn et. al., 2002). In porous rocks, the protons lose their alignment (decay) by surface relaxation as they collide with the solid, pore surface. In large pores, collisions will be fewer and relaxation slower than in small pores. Essentially, the larger the pore, the longer the decay time (Rider & Kennedy, 2011).

Figure 2-10 shows an idealized interpretation of the  $T_2$  distributions for water wet clastic rocks (Ellis & Singer, 2008). Free, producible fluids (water or hydrocarbons) are found with  $T_2$  values greater than 33ms, while capillary bound water is found between 3ms and 33ms. The components that decay faster than 3ms are attributed to clay-bound water, as illustrated in Figure 2-10 (Ellis & Singer, 2008). These  $T_2$  cutoff values are the basis for most NMR interpretation in clastic reservoirs around the world.



**Figure 2-10: A summary of the idealized interpretation of  $T_2$  distributions for water wet clastic rocks (Ellis & Singer, 2008).**

Figure 2-11 shows a typical display of NMR data. The right side track shows the  $T_2$  distribution at each depth. The left track shows the three NMR porosities calculated from the  $T_2$  amplitudes. The rightmost curve is the sum of amplitudes greater than 33ms (moveable fluid porosity). Between this lower limit and the middle dotted line, shaded in very light grey is the additional contribution between 3 and 33 ms (capillary bound water). The dark shaded region beyond corresponds to the porosity with  $T_2$  less than 3 ms (clay bound water).



**Figure 2-11: NMR  $T_2$  distributions as a function of depth are shown in the right track. The left track shows the moveable-fluid (right curve), capillary-bound (middle curve), and total (left curve) porosities calculated from the  $T_2$  amplitudes (Ellis & Singer, 2008).**

In bitumen settings, the NMR response is more complicated. Due to the extremely high viscosities, the  $T_2$  decay times are so low (on the order of 1 ms) to the point where NMR cannot detect the bitumen at all (Ellis & Singer, 2008). The simplest way to find bitumen is to compare the density porosity log (which sees all porosity), to the NMR total porosity (which does not see the bitumen), as shown in Figure 2-12.

Figure 2-12 shows an example well from the study area, with the NMR total, NMR free, and moveable fluid porosities plotted. The dark grey area represents the bitumen in the smallest pores and capillaries (not seen by the NMR). The magenta area represents hydrocarbon with poor mobility in small pores and capillaries that the NMR can see. Green represents free (moveable) fluid in the small to medium pores, and cyan represents free, moveable fluids in the larger pores. However, these are not true representations of moveable porosities because NMR cannot see most of the hydrocarbon porosity in bitumen settings (Bob Everett, retired Schlumberger petrophysicist, personal communication, November 2016).

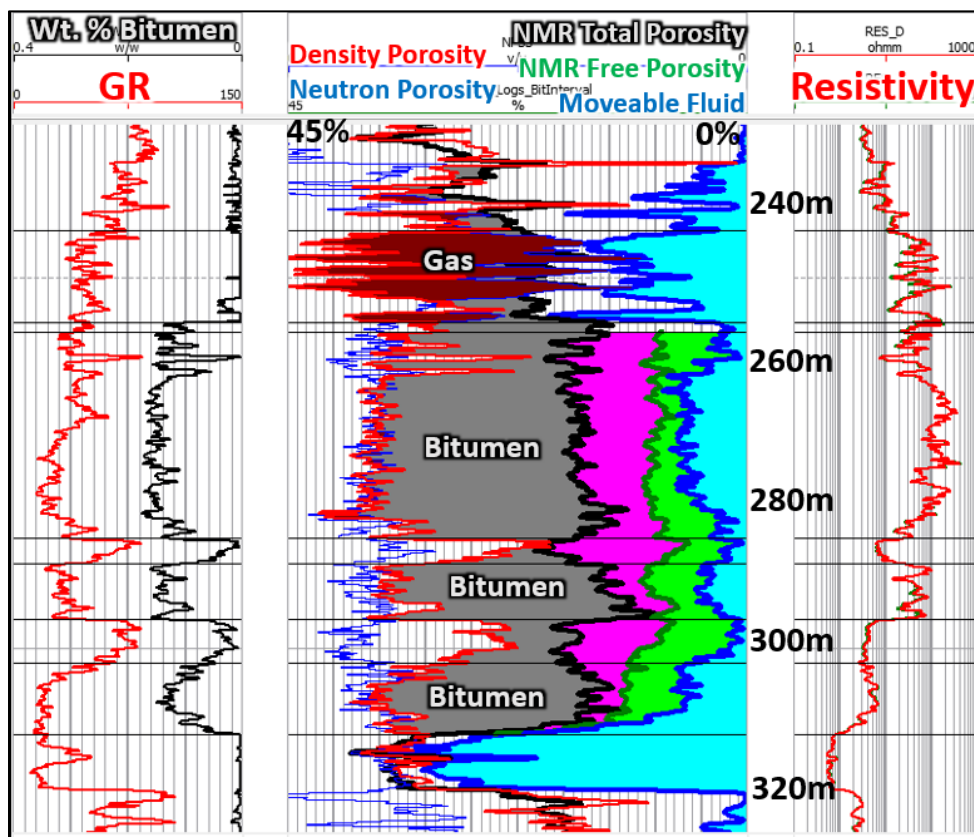


Figure 2-12: Oil sands well in the study area with NMR data. The density porosity and NMR total porosity curves diverge in the bitumen zones. The grey filled area is bitumen, the magenta area is hydrocarbon in small pores and capillaries, the green area is free hydrocarbon in medium pores, and blue represents free fluids in the larger pores (seen by NMR). Figure generated in Hampson-Russell™ software.

## Chapter 3 – Theory of Multilinear Regression

### 3.1 – Multi-Attribute Analysis

One way of measuring the correlation between a single attribute and the target attribute is to cross-plot them, in which case the best fit is a 2D line. If we cross-plot *two* attributes against the target attribute, the best fit is a plane, as shown in Figure 3-1. (Hampson-Russell 2016).

Figure 3-2 illustrates the basic multi-attribute problem, showing the target log and, in this case, three attribute logs to be used to predict the target attribute (Hampson-Russell 2016).

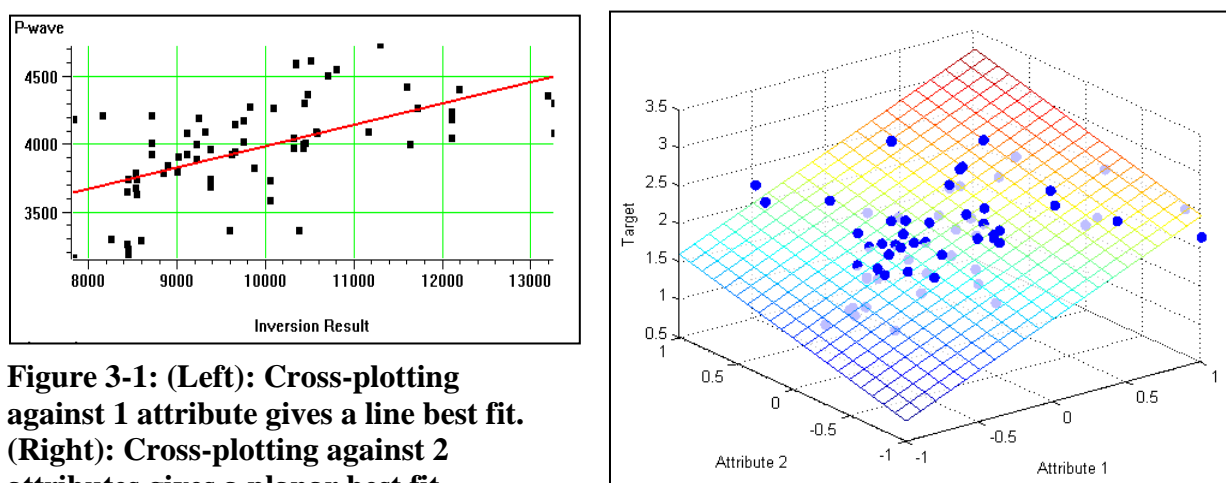


**Figure 3-1: (Left): Cross-plotting against 1 attribute gives a line best fit. (Right): Cross-plotting against 2 attributes gives a planar best fit (Hampson-Russell 2016).**

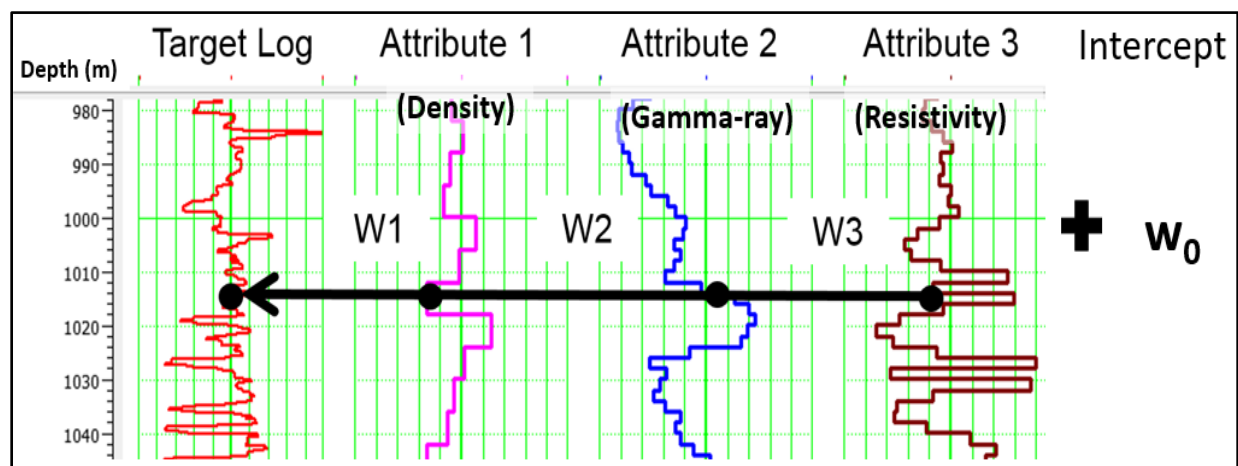


**Figure 3-2: The basic multi-attribute regression problem showing the target log and in this example, the 3 attributes to be used to predict the target (Hampson-Russell 2016).**

To illustrate the theory of multi-attribute prediction, let us assume the target log is P-wave velocity, attribute 1 is bulk density, attribute 2 is gamma-ray, and attribute 3 is resistivity. The goal in this example is to predict P-wave velocity (in the depth domain) from the bulk density, gamma-ray, and resistivity curves.

We can write the fundamental equation for linear prediction as:

$$Vp(z) = w_0 + w_1D(z) + w_2G(z) + w_3R(z) \quad (3.1)$$

where  $Vp(z)$  is P-wave velocity in m/s,  $D(z)$  is bulk density in  $\text{kg/m}^3$ ,  $G(z)$  is gamma-ray in GR-API units, and  $R(z)$  is resistivity in  $\text{ohm}\cdot\text{m}$ . This can be written as a series of linear equations:

$$\begin{aligned} Vp_1 &= w_0 + w_1D_1 + w_2G_1 + w_3R_1 \\ Vp_2 &= w_0 + w_1D_2 + w_2G_2 + w_3R_2 \\ &\dots \\ Vp_N &= w_0 + w_1D_N + w_2G_N + w_3R_N \end{aligned} \quad (3.2)$$

where each row of equations represents a single depth increment. This can also be written in matrix form:

$$\begin{bmatrix} Vp_1 \\ Vp_2 \\ \vdots \\ Vp_N \end{bmatrix} = \begin{bmatrix} 1 & D_1 & G_1 & R_1 \\ 1 & D_2 & G_2 & R_2 \\ \vdots & \vdots & \vdots & \vdots \\ 1 & D_N & G_N & R_N \end{bmatrix} \begin{bmatrix} w_0 \\ w_1 \\ w_2 \\ w_3 \end{bmatrix} \quad (3.3)$$

or more compactly as:

$$\mathbf{V}_p = \mathbf{A}\mathbf{W} \quad (3.4)$$

We typically find that there are many more depth increments than the number of input attributes. In other words, there are more rows in the  $\mathbf{A}$  matrix than columns. This means that we have an over-determined problem (more observations than unknowns), and the least-squares solution is given by (Russell 2004):

$$\mathbf{W} = [\mathbf{A}^T \mathbf{A}]^{-1} \mathbf{A}^T \mathbf{V}_p \quad (3.5)$$

Applying these solved weights minimizes the squared error between  $\mathbf{V}_p$  and  $\mathbf{AW}$ :

$$|\mathbf{V}_p - \mathbf{AW}|^2 \quad (3.6)$$

and by using Equation 3.2, we can now predict our target P-wave sonic log. An example cross-plot of the result is shown in Figure 3-3, with a correlation value of 0.93 between the measured and predicted P-wave sonic log.

The prediction error is defined as the root-mean-squared difference between the true target log and the predicted log:

$$PE = \sqrt{\frac{\sum_{i=1}^N (V_{pTrue,i} - (w_0 + w_1 D_i + w_2 G_i + w_3 R_i))^2}{N}} \quad (3.7)$$

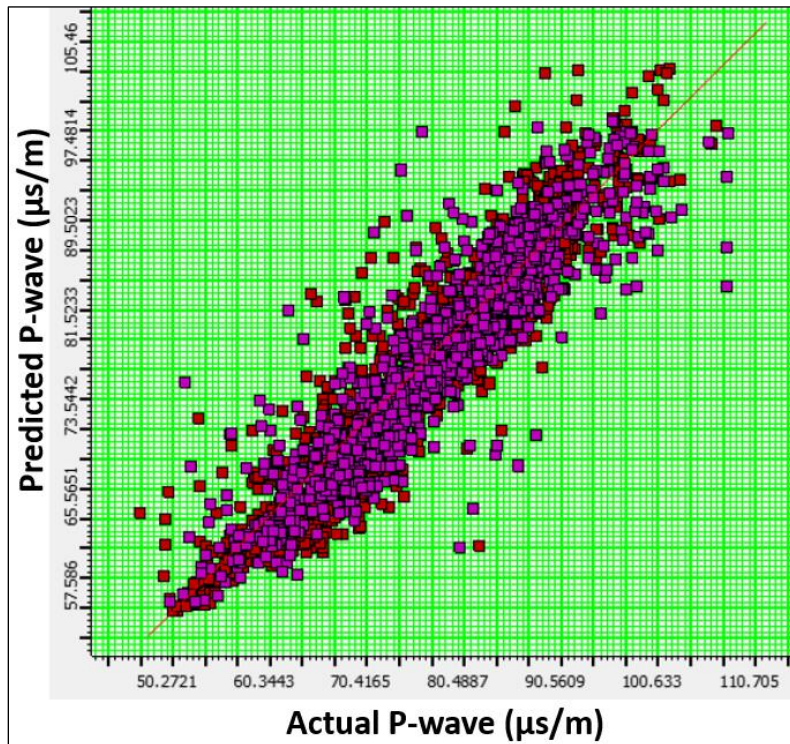


**Figure 3-3: Cross-plot of the predicted  $V_p$  against the actual  $V_p$ . The correlation value is 0.93 in this example (Hampson-Russell 2016).**

or more simply:

$$PE = \sqrt{\frac{\sum_{i=1}^N (V_{pTrue,i} - V_{pPredicted,i})^2}{N}} \quad (3.8)$$

where  $N$  is the number of depth increments in the well that we use to train our correlation.

### 3.2 – Step-Wise Regression

In the previous section we showed that P-wave velocity could be predicted using three attributes (density, gamma-ray, and resistivity). However, these might not be the best attributes to use for the prediction. Hampson-Russell's Emerge™ software uses a process called step-wise regression to find the combination of attributes that is most useful for predicting the target log. Step-wise regression can be nicely explained in a series of steps (Russell 2004):

1. Find the single best attribute by trial and error. In other words, calculate the prediction error for *each* individual attribute. The best attribute is the one with the lowest prediction error. Call this attribute A1.
2. Find the best *pair* of attributes. In other words, form all pairs of attributes including A1: (A1, gamma-ray); (A1, resistivity); (A1, neutron porosity); and so on. The pair with the lowest prediction error is the best pair. Call this second attribute A2.
3. Find the best *triplet* of attributes. In other words, form all triplets of attributes including A1 and A2: (A1, A2, resistivity); (A1, A2, neutron porosity); and so on. The triplet with the lowest prediction error is the best triplet. Call this third attribute A3.
4. Carry on this process until all the available attributes are used.

An important point to note is that the prediction error will *always* decrease (or stay the same) as we increase the number of attributes (Russell 2004). However, the validation error does *not* always decrease as we add attributes, which is addressed in the following section.

### 3.3 – Cross-Validation

Step-wise regression will give us a set of attributes that is guaranteed to reduce the total error as the number of attributes goes up. So when do we stop? This is determined using a technique called cross-validation, where we leave out a training well and predict it from the remaining wells (Russell 2004).

Suppose we use five wells to train our correlation:  $Well_1$ ,  $Well_2$ ,  $Well_3$ ,  $Well_4$ ,  $Well_5$ . Cross-validation works in the following steps (Hampson-Russell 2016):

1. Leave out  $Well_1$ , and solve for the regression coefficients using only data from ( $Well_2$ ,  $Well_3$ ,  $Well_4$ ,  $Well_5$ ). In other words, solve the system of equations from Equation 3.2 where the rows contain *no data* from  $Well_1$ .
2. With these coefficients, calculate the prediction error for  $Well_1$  (Equation 3.7 or 3.8), where now *only* data points from  $Well_1$  are used. This gives us the validation error for  $Well_1$ . Denote it as  $VE_1$ .
3. Repeat this process for  $Well_2$ ,  $Well_3$ ,  $Well_4$ , and  $Well_5$ , each time leaving the selected well out in the calculation of regression coefficients, but using only that well for the error calculation.
4. Calculate the average validation error for all wells:

$$VE_{avg} = \frac{VE_1 + VE_2 + VE_3 + VE_4 + VE_5}{5} \quad (3.9)$$

In this example, the validation error computation was done using three attributes. However, it is routinely performed after each stage of the step-wise regression procedure, so that we have the average validation error as a function of the number of attributes. A validation plot for an Emerge™ analysis is shown in Figure 3-4.

The horizontal axis shows the number of attributes used for the prediction, and the vertical axis shows the root-mean-square prediction error for that number of attributes (Equation 3.8). The lower black curve shows the error calculated using the training data (all of the wells). The upper red curve shows the error calculated using the validation data (by systematically leaving out wells and calculating the average validation error). This particular example shows that when greater than four attributes are used, the validation error starts to increase, which means that any additional attributes will over-fit the data (Russell 2004).

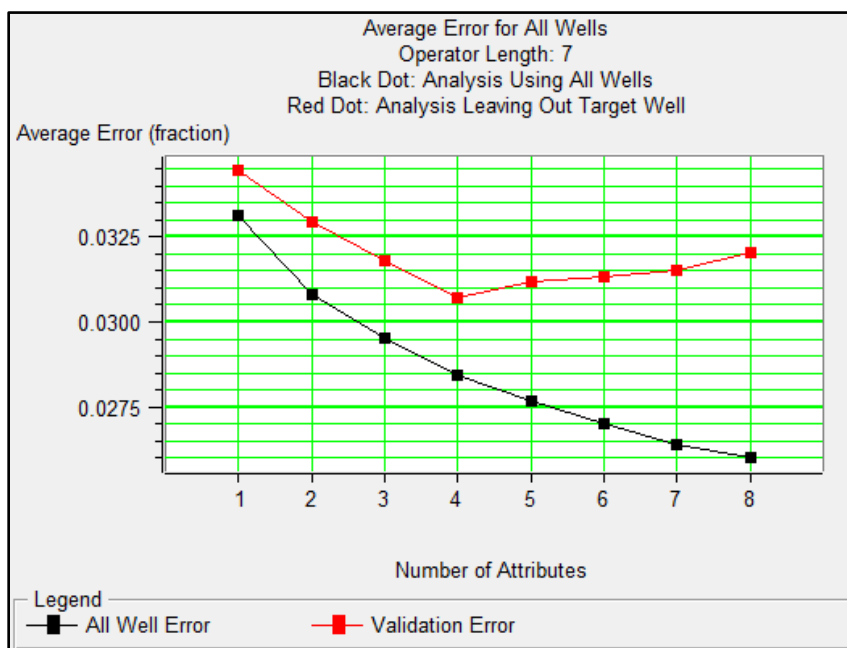


**Figure 3-4: An Emerge™ prediction error plot. (Hampson-Russell 2016).**

Why would the validation error increase when we add more data? Adding attributes is similar to fitting a curve through a set of points, using a polynomial of increasing order (Hampson-Russell 2016). Figure 3-5 shows how a higher order polynomial (dashed curve) can fit the training data better (the black points), but can still fit the remaining test data poorly (the white points). A lower-order polynomial (solid curve) fits the training data slightly poorer, but the overall fit to the data is improved (Hampson-Russell 2016).

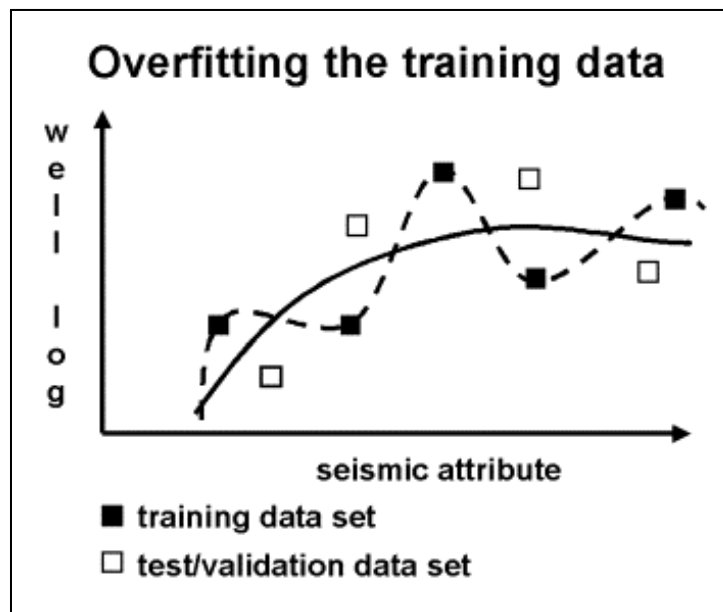


**Figure 3-5: Illustration of how a higher order polynomial can over-fit the training data (Hampson-Russell 2016).**

## Chapter 4 – Study Area Geology and Dataset

### 4.1 – Introduction to Study Area

The study area for this thesis is located within the Athabasca oil sands of Alberta, in the vicinity of Fort McMurray. Athabasca is the largest oil sands deposit, followed by Cold Lake and Peace River (Figure 4-1). The data donor has requested that the exact project location remain confidential.

The reservoir of interest is the McMurray Formation, a bitumen saturated reservoir situated about 200m to 350m below the surface. Production of the viscous bitumen is ongoing



**Figure 4-1: Distribution of Alberta’s oil sands deposits (Norman Einstein, Own work, Public Domain, <https://commons.wikimedia.org/w/index.php?curid=773312>).**

through steam-assisted gravity drainage (SAGD) which uses pairs of horizontal steam injection and producing wells drilled through the McMurray formation reservoir to mobilize the bitumen. The reservoir sands are hosted in stacked channel deposits, separated by silty or muddy intervals (Hein et. al. 2013).

Bitumen of the Athabasca region is heavy and largely immobile due to extensive biodegradation, containing in-situ viscosities from 100,000 cP to over 1,000,000 cP, and API gravities from 8° to 10°, in comparison to conventional oil with API gravities from 24° to 40° (Mossop, 1980). The sand grains of the bitumen reservoir are water wet, a key element which makes steam injection recovery possible. Oil saturation levels vary, containing up to 20% bitumen by weight (Mossop, 1980).

Average reservoir effective porosities in the study area are on the order of 30%, with an average shale volume of 11% and permeability in the range of 4800-6300 mD. Water saturation levels average 32%, and in-situ reservoir temperatures are about 10°C at pressures from 1000-1100 kPa (Kelly, 2012).

## **4.2 – Study Area Geology**

The stratigraphic units of the Athabasca oil sands system comprise of the Cretaceous siliciclastic rocks and the underlying Devonian carbonates. Figure 4-2 shows a simplified stratigraphic column highlighting the three intervals of interest: the Beaverhill Lake Group carbonates, the McMurray Formation reservoir, and the Clearwater Formation caprock. The units will be described here from the bottom up, using the example well log suite from Figure 4-3 to support the descriptions. This particular well was chosen because it is one of the few wells that has log data reaching the top of the Devonian carbonates.

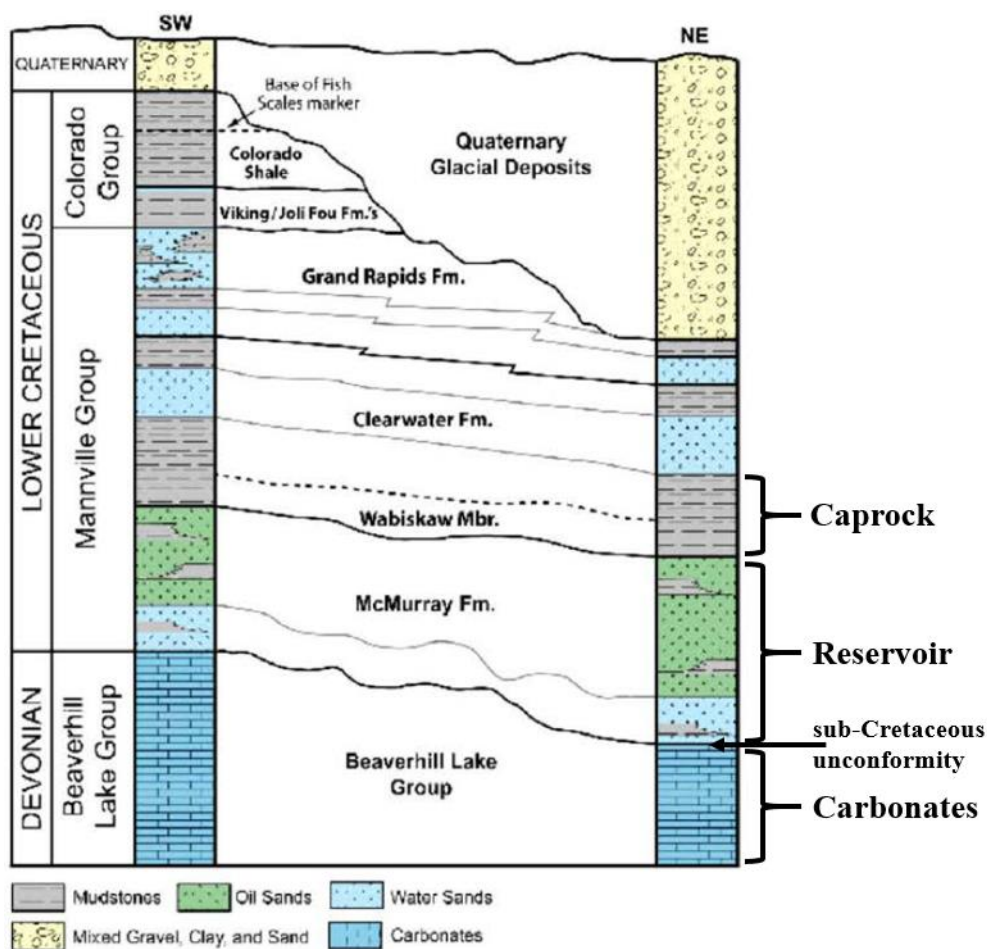


**Figure 4-2: Stratigraphic chart for the McMurray oil sands system (Nexen AER Report, 2015).**

Below the bitumen reservoir sits the Beaverhill Lake Group carbonates, consisting of Devonian age dolomites, limestones, and evaporates (Schneider et. al., 2012). They are characterized by a high degree of deformation and karsting due to dissolution of the Prairie Evaporite Formation salts (situated directly underneath the Beaverhill Lake Group). The result is a complex surface with varying structural highs and lows (Schneider et. al., 2012). The upper boundary of the Beaverhill Lake Group is defined by the sub-Cretaceous unconformity. It is an angular unconformity representing an ~ 250Ma hiatus of sedimentation, with extensive erosion and karsting (Hein et. al., 2013). The sub-Cretaceous unconformity represents an ancient

paleo-geographic erosional surface containing escarpments, faults, sinkholes, and collapse features (Schneider et. al., 2012). The structure of the sub-Cretaceous unconformity is important to understand since it heavily influences the deposition of the overlying McMurray Formation sediments.

The transition from the McMurray Formation sands to the Beaverhill Lake Group carbonates is easily identified from logs (Figure 4-3 at 235m). There are abrupt decreases in the P- and S-wave slownesses, and in the density porosity (meaning increasing density), plus an increase on the photoelectric curve from 2 barns/electron (indicating sandstone) to 5 barns/electron (indicating limestone). Sonic logs are usually plotted with slowness increasing to the left (ie. velocity increasing to the right). For an illustration of how the  $V_p/V_s$  ratio behaves, refer to Figure 5-6 in chapter 5.

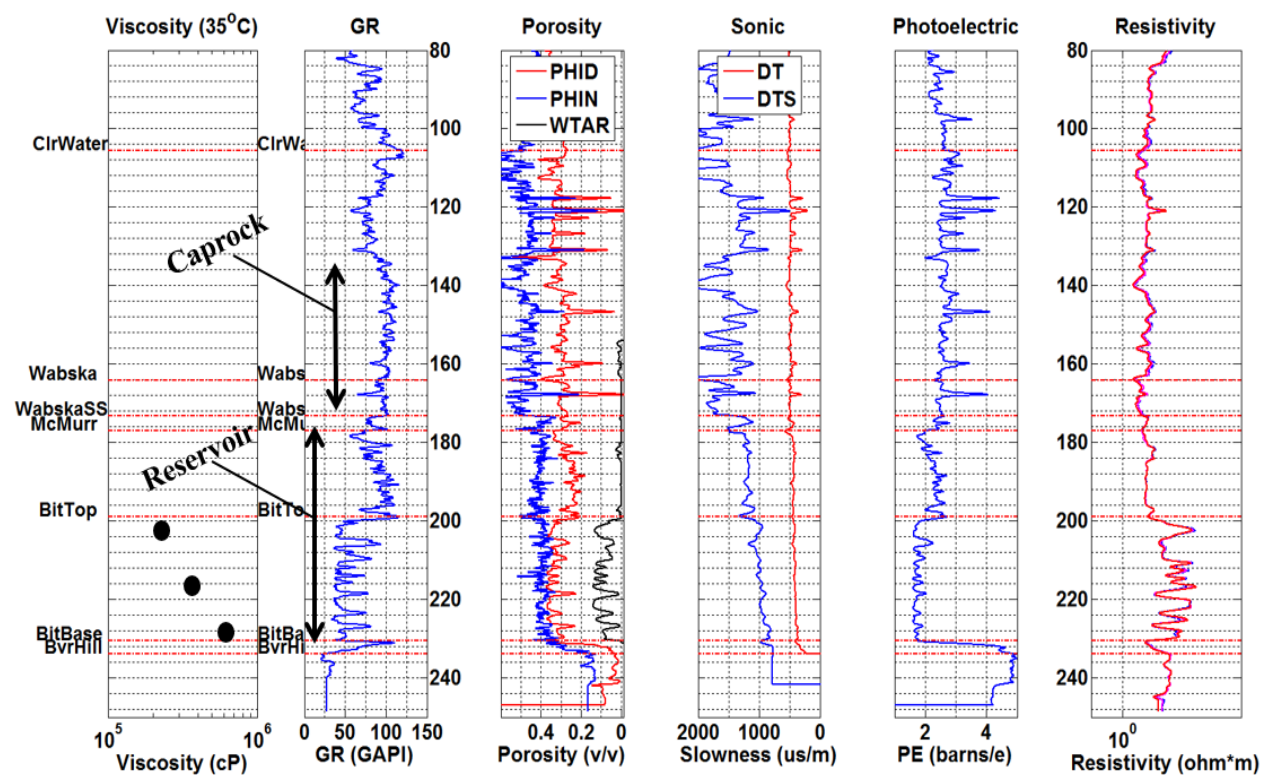


**Figure 4-3: Log suite for an example well in the study area, from the Clearwater Formation caprock down to the Beaverhill Lake Group carbonates. The depth units are in meters. Figure plotted in MATLAB®.**

The McMurray Formation is the main bitumen reservoir throughout the Athabasca region and the focus point of this study. It is characterized by continental successions of fine to very fine-grained sands with mixed-in conglomerates and mudstones (Mossop, 1980). It was deposited in a N-S trending incised valley or depression on top of the sub-Cretaceous unconformity, created from dissolution of the Prairie River Evaporite salts and resulting collapse of the overlying formations (Hein et. al., 2013). In the Cretaceous period, a large fluvial system shaped the underlying carbonates into a distribution of structural highs and lows. The lows play a key role in the amount of reserves in the McMurray Formation, because the sediments that were deposited in lows host most of the bitumen. The thickness of the McMurray is dependent on the Devonian structure, varying from 150m thick in the centre of deposition to where it pinches out in the west against a ridge of Devonian limestone (Flach, 1984). The stratigraphic framework of the McMurray is shown in Figure 4-4.

The McMurray is usually divided into a Lower and an Upper section. The Lower McMurray is comprised of fluvial sediments with sand dominated channels and point-bar complexes with high porosities and permeabilities. These lowermost sediments are called the McMurray C channel deposits. They directly overlay the sub-Cretaceous unconformity. In some regions, channel fill from the Upper McMurray almost entirely erodes through the Lower McMurray to the sub-Cretaceous unconformity. These sediments are simply called McMurray channel sediments (Hein et. al., 2013).

The Upper McMurray is split into A and B sequences, which mainly consist of coastal plain and estuarine successions, respectively, containing channel fill and point bar complexes with lower porosities and permeabilities than in the Lower McMurray (Hein et. al., 2013). The

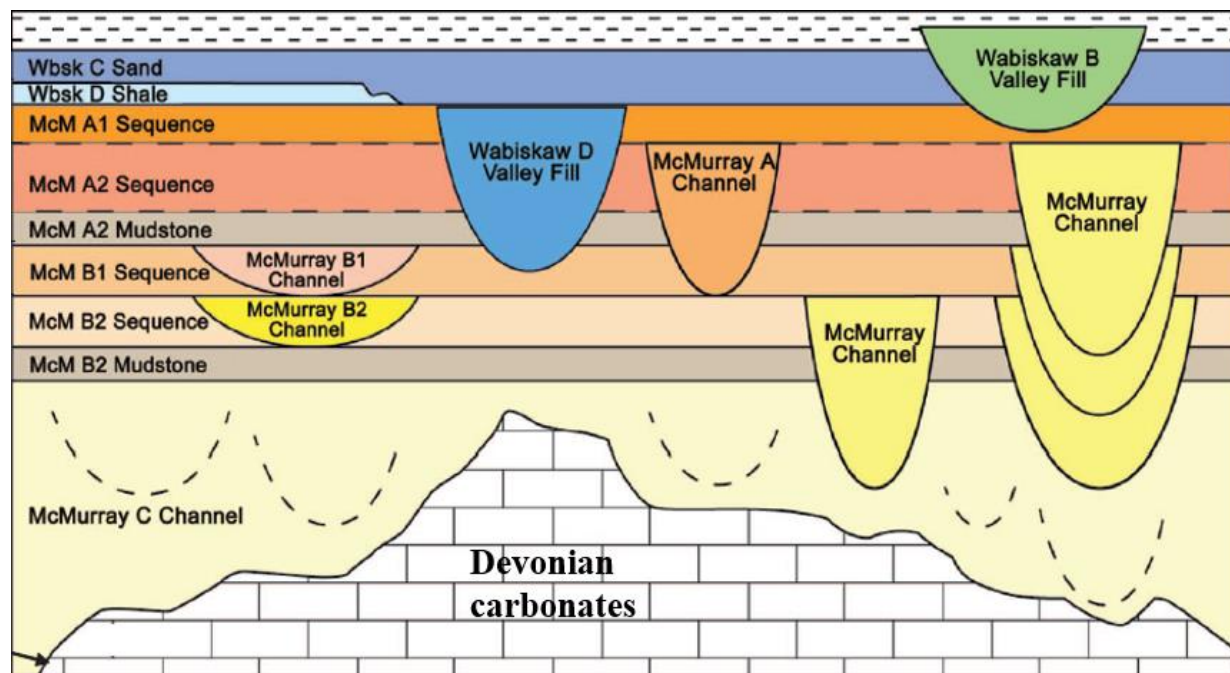


**Figure 4-4: Stratigraphic framework for the McMurray Formation and Wabiskaw member in the Athabasca region of Alberta (Hein et. al., 2013).**

channel fills contain a mixture of mudstones and point bar sands, which are often bitumen-saturated. The mudstones are commonly present in the form of inclined heterolithic stratification (IHS), which are typically thick and discontinuous fills from abandoned channels, acting as baffles to steam-chamber flow (Hein et. al., 2013). Due to the shallow depth of the McMurray (lack of burial), the bitumen sands are unconsolidated (Mossop, 1980).

In the study area, the bitumen saturated zones are mostly confined in the mid to lower levels of the McMurray. This is demonstrated in Figure 4-3 from the low (sand) gamma-ray response, porosities greater than 30%, high resistivity readings, and the weight % bitumen (WTAR) curve from 200m to 230m. Note that it is not a homogeneous sand unit, there are several thin shaley zones in between the clean sands. Figure 4-2 shows a wet sand layer underneath the oil sands layer because water is present underneath the bitumen in some, but not all places throughout the study area. The well from Figure 4-3 does not have bottom water, but

several wells in the area do have bottom water ranging from thin to 20m thick.

Lastly, the viscosity samples in this study encompass the bitumen-saturated zones in the mid to lower McMurray (Figure 4-3), and viscosity appears to increase with depth in most cases.

The Clearwater Formation conformably overlies the McMurray reservoir throughout the Athabasca region. The base of the Clearwater Formation contains the Wabiskaw Member, a glauconitic sandstone with interbedded shales, that acts as a secondary target for oil sands extraction (Hein et. al., 2013). The rest of the Clearwater Formation is largely heterogeneous, containing fine-grained marine shales with intermixed silt and sands (Flach, 1984). The fine-grained shales form the caprock of the McMurray reservoir, providing a vertical seal for the oil prior to biodegradation, and presently serves as a vertical barrier preventing steam from migrating upward.

In the study area, there is a shaley-sand wet zone in the Upper Clearwater, seen from 120m to 130m depth in the example well (Figure 4-3). The caprock interval in the study area is defined as the interval from the shale beneath this wet zone down to the Wabiskaw sand zone, as annotated in Figure 4-3.

### **4.3 – Dataset**

A focused map of the oil sands study area is shown in Figure 4-5. In the area, there are 78 total wells with viscosity measurements, shown by the large well symbols. 40 of these wells have full suites of logs, highlighted by the large red symbols. *These 40 wells were used to train the viscosity prediction*, as described in chapter 5. All wells here with viscosity measurements were vertically drilled. The wells each have had cores taken from the McMurray formation. The bitumen was extracted from the cores by a 3<sup>rd</sup> party laboratory and the kinematic viscosities were

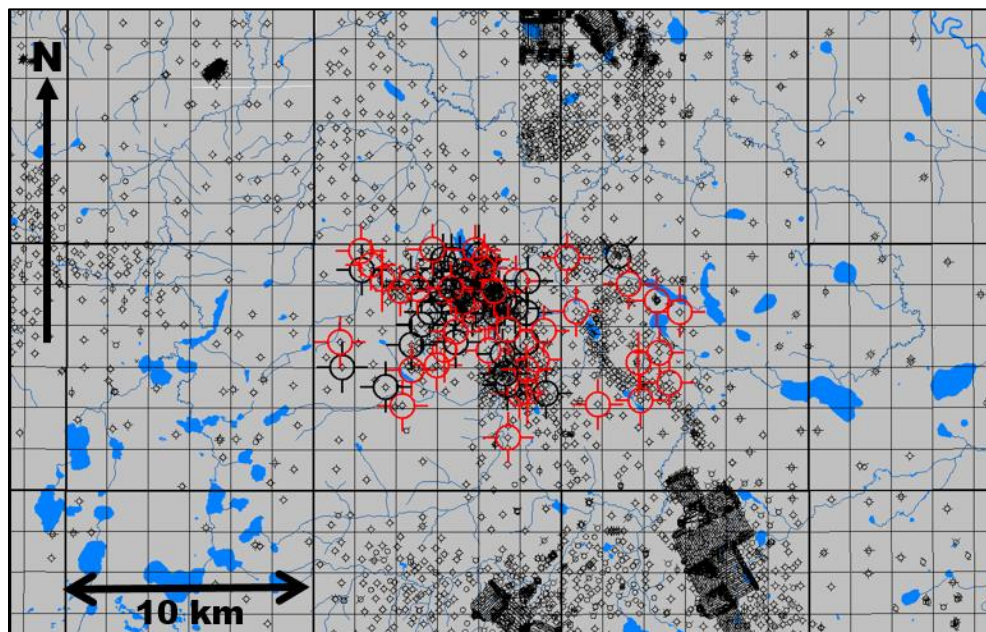


**Figure 4-5: Map of the oil sands study area. The large well symbols are the 78 wells with viscosity measurements. The large red well symbols are the 40 corresponding wells that also contain a full suite of logs. These 40 wells were used to train the viscosity prediction. Figure generated in SeisWare™**

measured at 35°C, 55°C, and 75°C. The measurements at 35°C were used for this study which most closely resembles reservoir conditions. The majority of wells have 3 viscosity measurements: shallow, middle, and base reservoir samples as in Figure 4-3.

Figure 4-6 shows a histogram of all the viscosity samples throughout the study area. The viscosities range from 10,000 cP to 550,000 cP, with an average value of 121,000 cP and standard deviation of 100,000 cP.

Figure 4-7 shows the distribution of the base reservoir viscosity measurements, interpolated between wells using a standard minimum curvature algorithm in SeisWare™. There are significant lateral viscosity variations throughout the reservoir. If we could predict these variations from well logs before developing the reservoir (the focus for the next chapter), it would greatly help in determining the optimal recovery method, amount of steam to inject, and well placement.

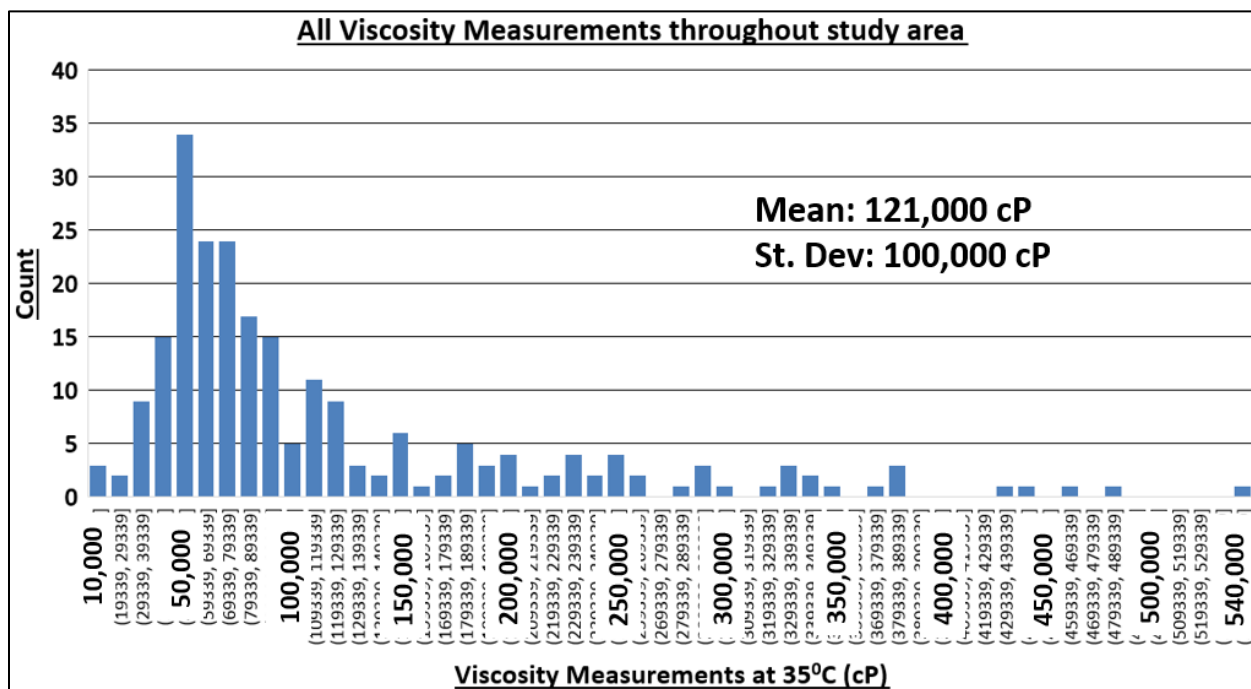


Figure 4-6: Histogram of all laboratory viscosity measurements throughout the study area.

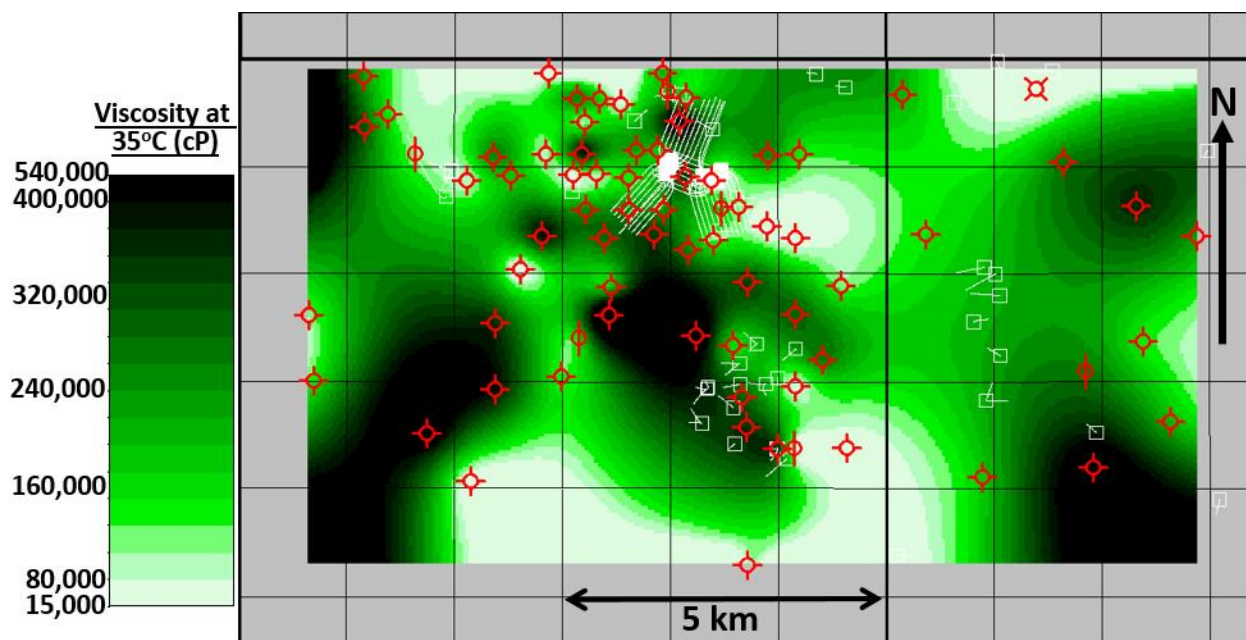


Figure 4-7: Distribution map of the base reservoir viscosity measurements. All the data wells are shown in red (generated in SeisWare™).

## Chapter 5 – Problem Setup, and Viscosity Prediction Results

### 5.1 – Well log normalization process

Before performing quantitative analysis on well logs (such as prediction), the logs should all be normalized. Well log normalization identifies and removes systematic errors from well log data so that reliable results may be obtained for reservoir evaluation, solving difficult correlation and quantitative problems. Reasons for tool inaccuracies include varying borehole conditions from well to well, improper wellsite tool calibrations, or logs from different logging companies in the same area (Shier, 2004).

There are a number of methods for normalizing logs within a cluster of wells. For this study the “Big Histogram Method” was used, which adjusts the logs within a zone of interest to all have the same average and standard deviation value from well to well (Shier, 2004). Figure 5-1 illustrates this concept for the gamma ray logs. The histogram shows the distribution of gamma ray values for the 40 project wells from top to base of the gross bitumen interval.

The gamma ray logs for each well were then adjusted so that the average and standard deviation values matched the global average (44 and 15.5 GR-API respectively) using the

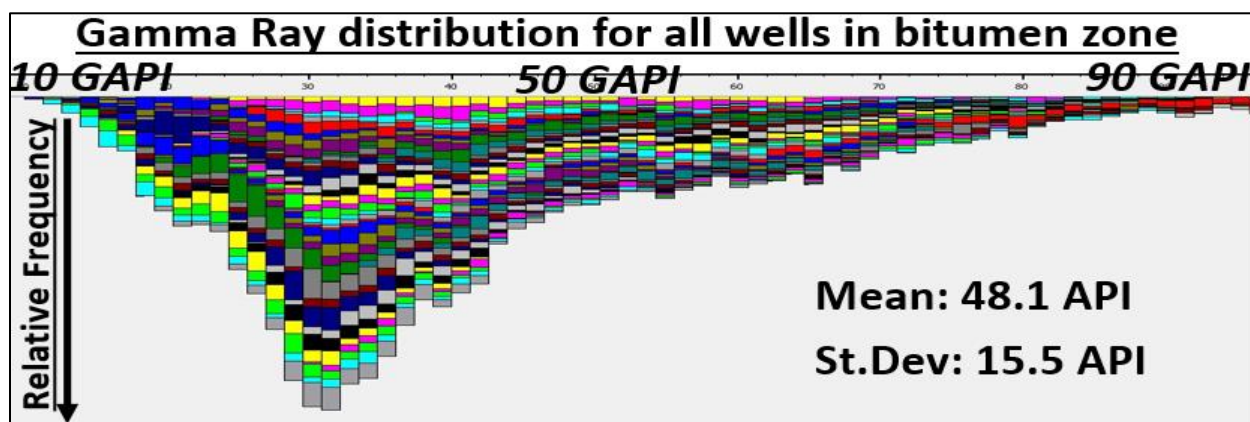


**Figure 5-1: Distribution of the gamma ray values for the 40 training wells from top to base of the gross bitumen interval. Each color represents a different well. Figure created in Hampson-Russell™ software.**

normalization equation at each depth sample:

$$Output(i) = \frac{LogValue(i) - Average}{StdDev} (DesiredStdDev) + DesiredMean \quad (5.1)$$

where *Average* and *StdDev* represent the average and standard deviation values of the log in a specific well, and *DesiredStdDev* and *DesiredMean* represent the global values that each well is adjusted to match.

Figure 5-2 shows an example well of how the normalized logs (red) compare to the un-normalized logs (blue). The normalized logs resemble bulk shifted versions of the original logs to match the global average, with some slight character changes to match the global standard deviation. To normalize the resistivity logs, the base 10 logarithm of resistivity was normalized and converted back to ohm\*m units, since resistivity has a logarithmic scale.

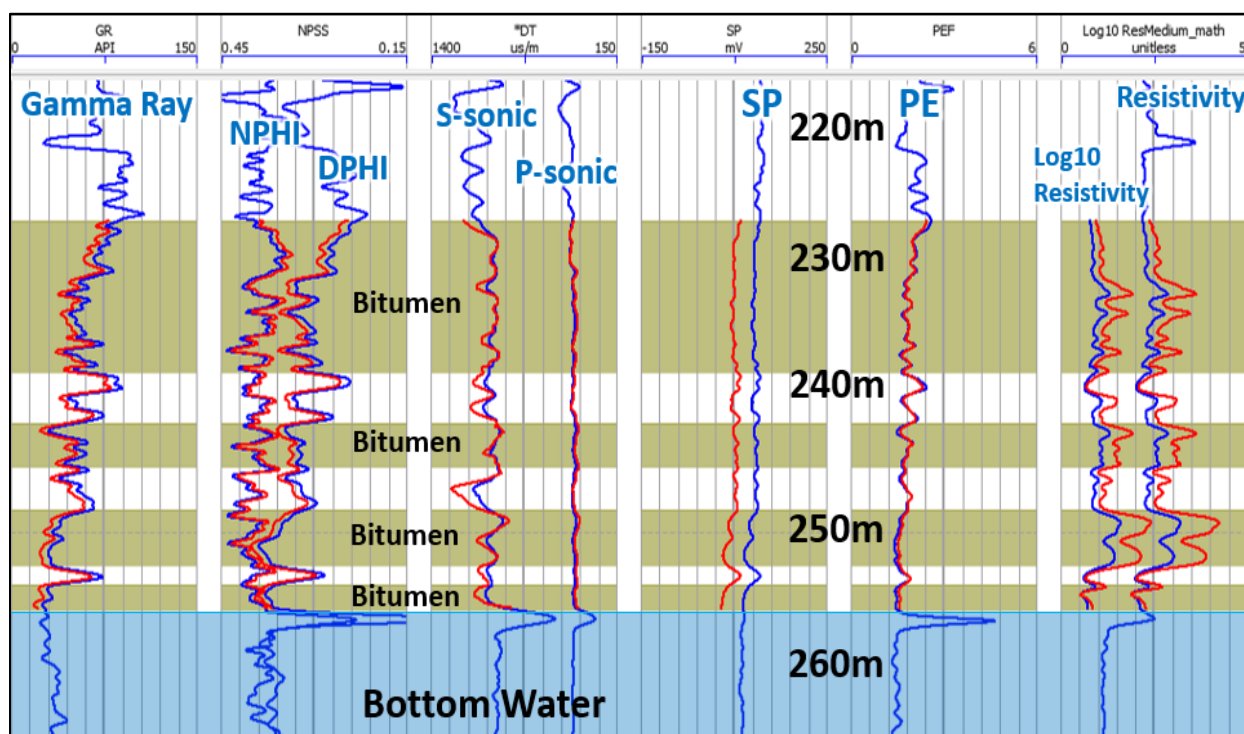


**Figure 5-2: What the normalized logs look like (red) versus the un-normalized logs (blue). The normalization was focused from top to base of the gross bitumen interval. The gold zones highlight the bitumen intervals.**

## 5.2 – Adding NMR logs as viscosity predicting attributes

It is already known that the NMR logging response can be correlated to viscosity, as discussed in section 1.3. The purpose of incorporating NMR data into this study was to see if combining NMR with the other well logs improves the data-driven viscosity prediction.

Donor Company has generously provided all of their wells in the study area that have NMR data. Unfortunately, none of the 25 provided NMR wells have viscosity measurements. Therefore, the 25 NMR wells were used to find the best NMR prediction model from the remaining well logs. The prediction model was then used to blindly predict the NMR logs in each of the 40 viscosity wells to see if the predicted NMR logs would improve the viscosity prediction. Quite an ambitious, and possibly laughable, task.

Table 5-1, Table 5-2, and Table 5-3 show the Emerge™ top predicting attributes for NMR total porosity, NMR free porosity, and NMR moveable water, respectively. Note that each row corresponds to a particular multi-attribute transform and includes all the rows above it.

	<b>Target (%)</b>	<b>Attribute</b>	<b>Units</b>	<b>Validation Error (%)</b>
1	NMR Total Porosity	1 / (Medium Resistivity)	1 / (ohmm)	3.47
2	NMR Total Porosity	(P-wave sonic) <sup>1/2</sup>	( $\mu\text{s}/\text{m}$ ) <sup>1/2</sup>	3.23
3	NMR Total Porosity	ln  Gamma Ray	ln GR-API	2.96

**Table 5-1: Emerge™ top predicting attributes for NMR Total Porosity.**

	<b>Target (%)</b>	<b>Attribute</b>	<b>Units</b>	<b>Validation Error (%)</b>
1	NMR Free Porosity	1 / (Medium Resistivity)	1 / (ohmm)	3.53
2	NMR Free Porosity	(P-wave sonic) <sup>2</sup>	( $\mu\text{s}/\text{m}$ ) <sup>2</sup>	3.28
3	NMR Free Porosity	Gamma Ray	GR-API	3.09

**Table 5-2: Emerge™ top predicting attributes for NMR Free Porosity.**

	<b>Target (%)</b>	<b>Attribute</b>	<b>Units</b>	<b>Validation Error (%)</b>
1	NMR Moveable Fluid	1 / (Medium Resistivity)	1 / (ohmm)	3.45
2	NMR Moveable Fluid	(Density) <sup>1/2</sup>	( $\text{kg}/\text{m}^3$ ) <sup>1/2</sup>	3.17
3	NMR Moveable Fluid	1 / (Neutron Porosity)	1 / (decimal)	2.93
4	NMR Moveable Fluid	(P-wave sonic) <sup>2</sup>	( $\mu\text{s}/\text{m}$ ) <sup>2</sup>	2.79

**Table 5-3: Emerge™ top predicting attributes for NMR Moveable Fluid Porosity.**

Figure 5-3 is the distribution of the NMR wells in the study area, showing respectable coverage throughout the study area except perhaps in the far western part.

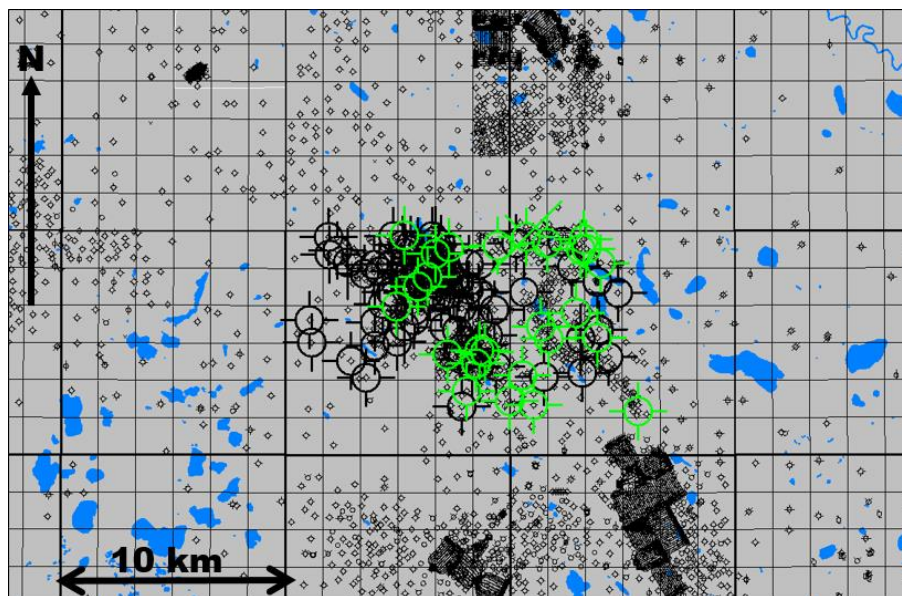


**Figure 5-3: Distribution of the 25 NMR wells in the study area. The NMR wells are shown in large green symbols. The large black symbols are the project wells with viscosity data.**

Figure 5-4 shows the predicted NMR porosities plotted over the measured NMR porosities for 2 example wells. The prediction model was trained using all 25 NMR wells from the top to base of the bitumen interval. Overall, the raw logs did a slightly better job at predicting the NMR curves than the normalized logs, with an average validation error of 3%. NMR free porosity was the least detailed prediction, but the overall trend was usually present. Normalizing the NMR logs before predicting them made the prediction more unstable, so the results were normalized after they were predicted.

The multi-regression prediction models (Table 5-1, Table 5-2, Table 5-3) were then used to blindly predict the NMR porosity logs in each of the 40 viscosity wells. If the 25 NMR training wells had not sampled the entire study area as well, much more uncertainty would have been associated with the blind NMR predictions.

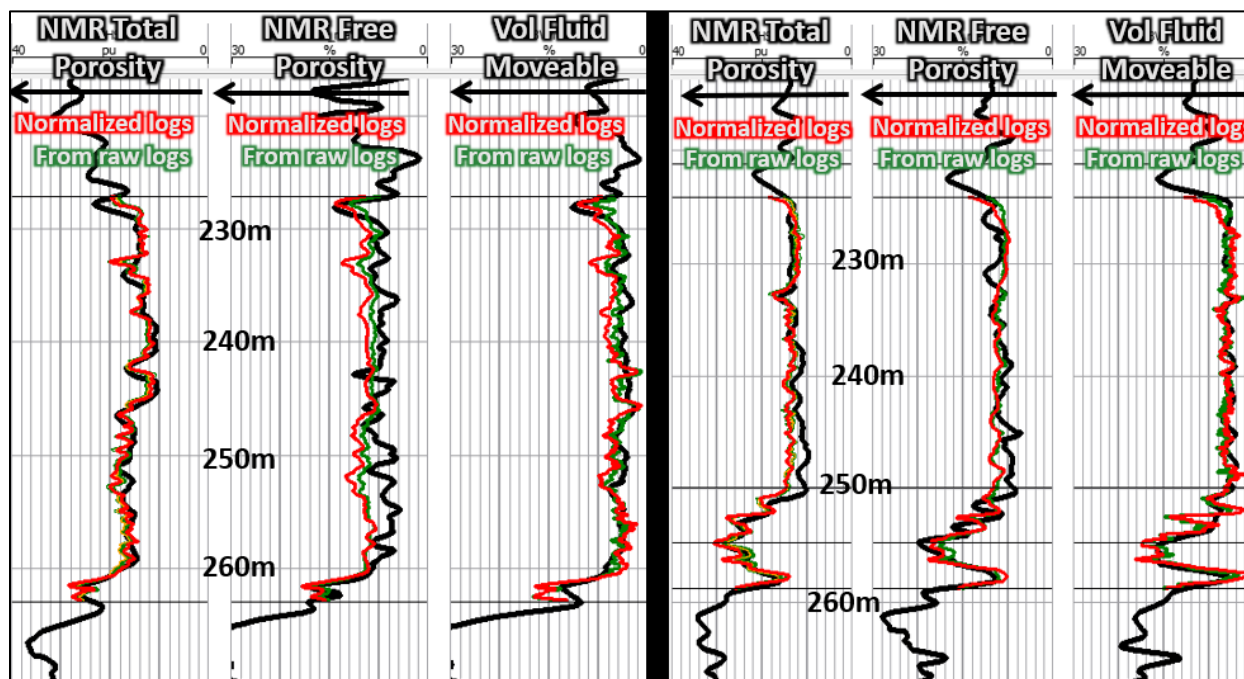


**Figure 5-4: Predicting NMR porosities from Resistivity, P-wave sonic, Gamma Ray, and Neutron Porosity. Validation results for two example wells are shown. Each of the 25 NMR wells were systematically left-out and predicted from the remaining 24 wells. The black curves are the measured NMR porosities, the red curves are the predicted NMR porosities using normalized logs, and the green curves are the predicted NMR porosities using the un-normalized (raw) logs. Credit: Hampson-Russell Emerge™**

### 5.3 – Viscosity training model

In order to train a multi-attribute relationship how to predict viscosity from other logs, we had to create viscosity target logs for the Hampson-Russell Emerge™ database. This was done for each of the 40 training wells (Figure 4-5) using two different methods: in the first method, the target viscosity logs were created by linear interpolation between each viscosity measurement point, and nulling the log everywhere outside of the reservoir interval. This is shown in the left track of Figure 5-5 for an example well, where the three viscosity measurements are denoted by the blocked red log, and the black curve shows the interpolated target viscosity log.

The second method creates the target viscosity log using a 1-meter training window centered around the true measurement depths, as shown by the gold zones in Figure 5-5.

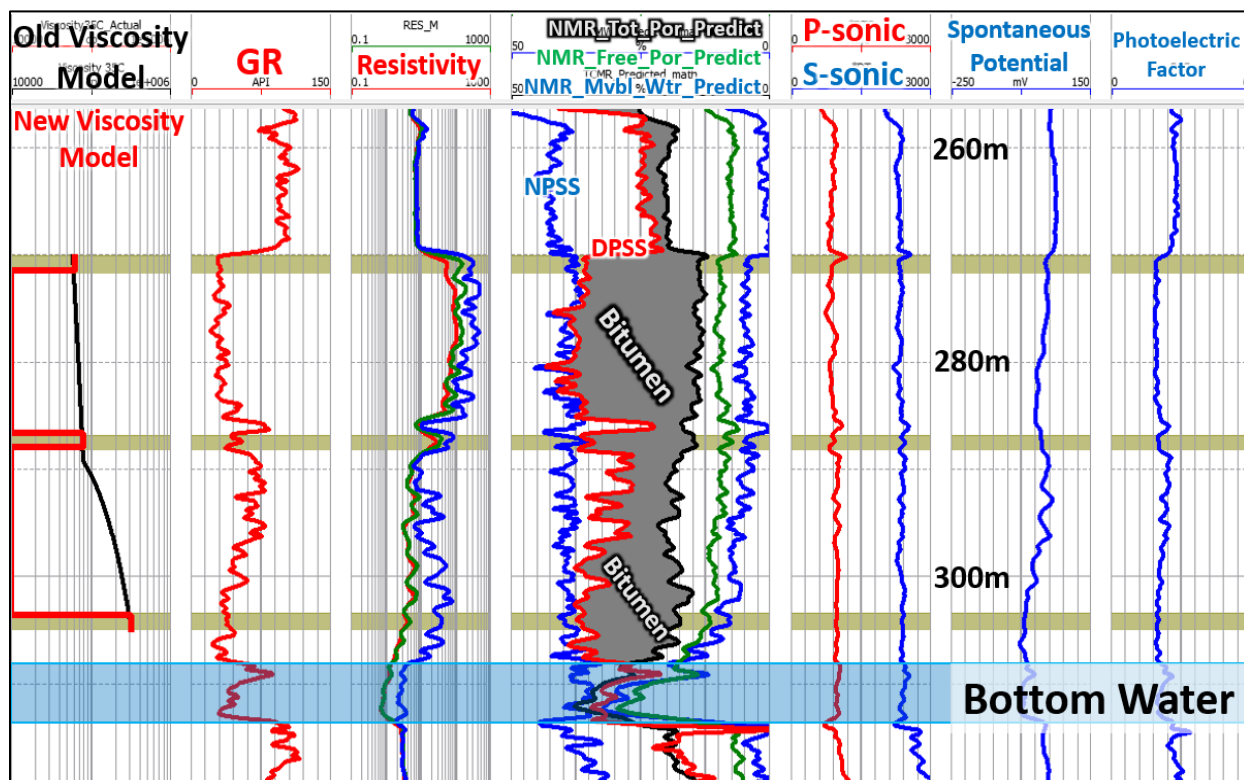


**Figure 5-5: Viscosity training model.** In the left track, the black curve is the old (interpolated) target viscosity log. The red curve is the new target viscosity log, with 1-meter training windows centered around the true measurement depths (shown by the gold zones). The viscosity is presented on a logarithmic scale from 10,000 cP to 1,000,000 cP. The predicted NMR porosity logs are also shown, with the shaded grey area indicating the presence of bitumen from the density porosity and NMR total porosity.

In cases where the measurement depth plotted in a shale interval, it was moved to the nearest reservoir interval. It is believed that the second method generates superior viscosity predictions because the initial model (black curve) assumed that viscosity varies linearly between each measurement point, which is a significant oversimplification. The updated prediction model (red blocked log) trains the prediction only at the known measurement depths with the known values.

The results presented in this thesis focus on the predictions generated from the new (second) training model. However, comparison figures are presented in section 5.5 that qualitatively show how the new training model generates results superior to the old model.

To extend the concept of viscosity prediction into the seismic domain, the density, P-

wave, and the S-wave sonic logs were used to calculate the following seismic properties in the 40 project wells: P-impedance, S-impedance, Bulk Modulus, Shear Modulus,  $V_p/V_s$ , Young's Modulus, Poisson's Ratio, P-Elastic Impedance, and PS-Elastic Impedance. These properties were used as predicting attributes to generate a separate viscosity prediction in each well, using only log-derived seismic properties. The setup of the training model was exactly the same as the one described above, only the predicting attributes have changed (Figure 5-6).

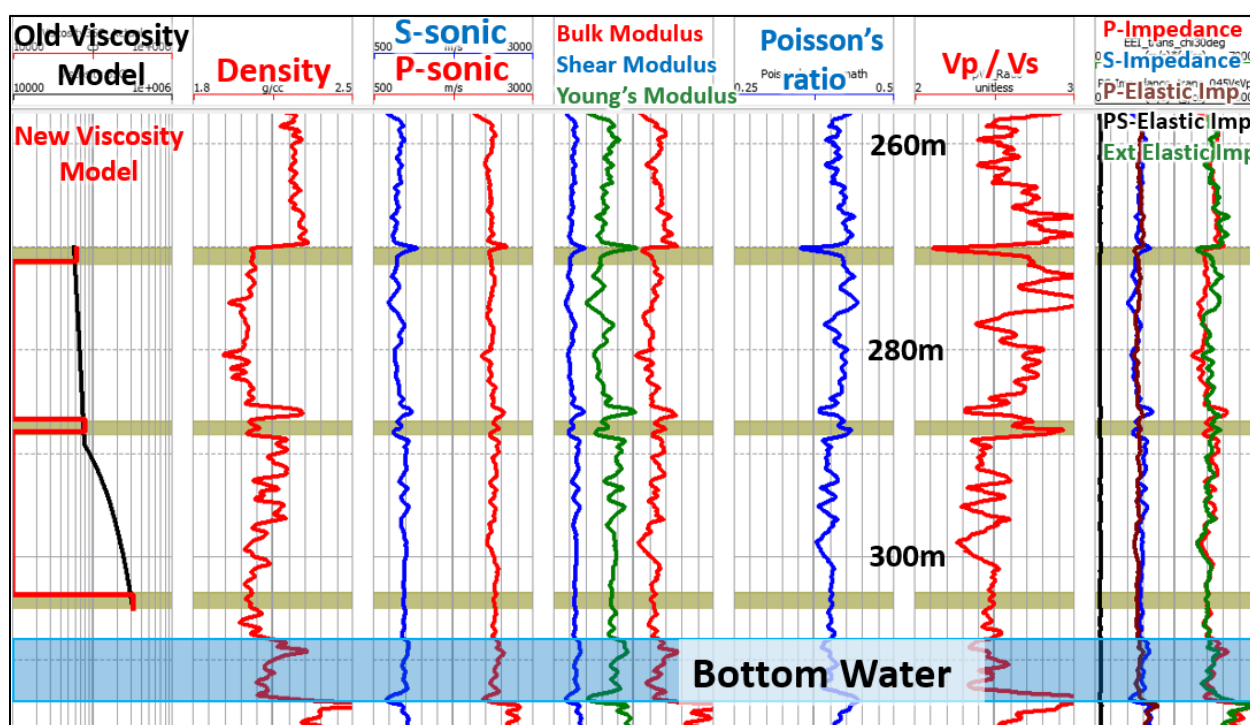
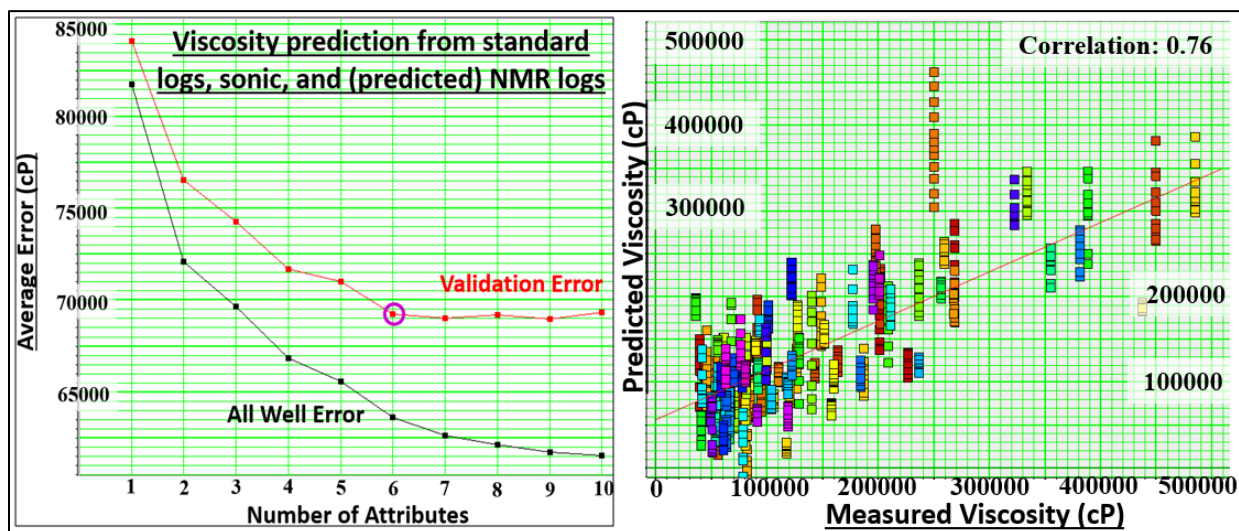


**Figure 5-6: Viscosity training model using only log-derived seismic properties.** In the left track, the black curve is the old (interpolated) target viscosity log. The red curve is the new target viscosity log, with 1-meter training windows centered around the true measurement depths (shown by the gold zones). The viscosity is presented on a logarithmic scale from 10,000 cP to 1,000,000 cP.

#### 5.4 – Viscosity prediction results using all logs, and calculated seismic properties

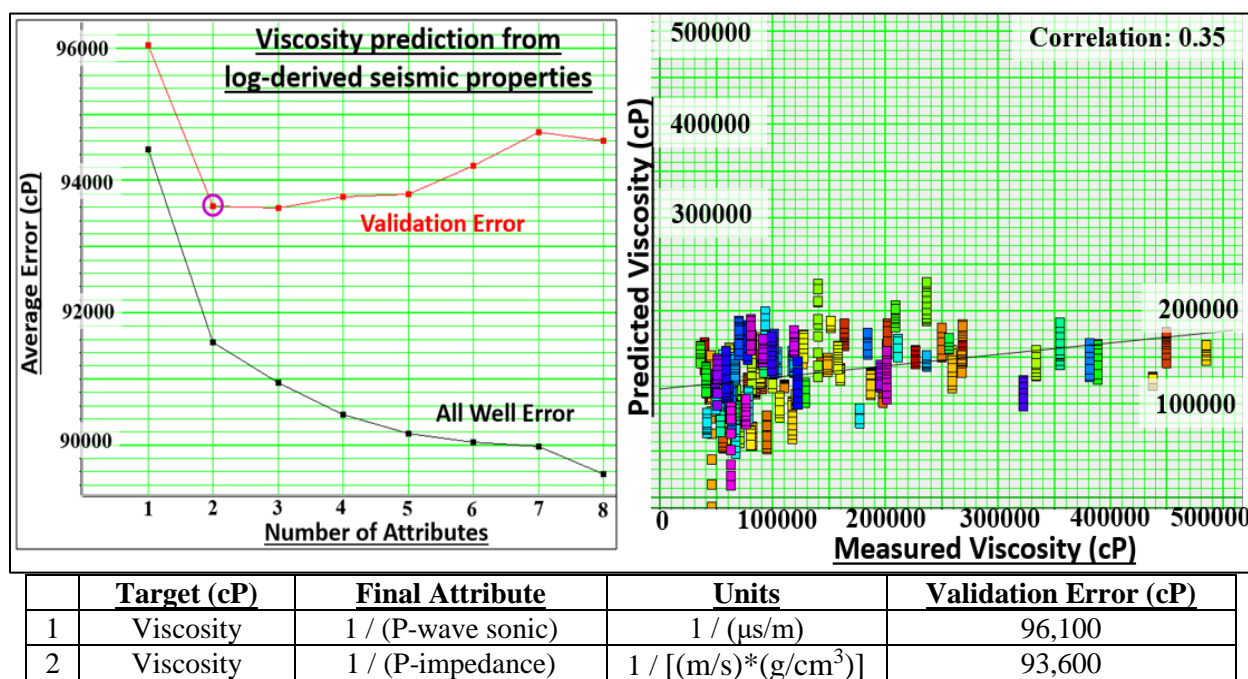
Upon running the multi-linear regression analysis in Hampson-Russell's Emerge™ software (as explained in chapter 3), the top viscosity predicting attributes were determined.

Figure 5-7 shows the graphical training and validation errors from using all available well logs as predicting attributes, along with the list of the attributes in descending order of importance. The results show the optimum viscosity prediction is made using the top six attributes. The validation error curve remains almost flat beyond six attributes, indicating that the prediction would be over-trained beyond six attributes. The average validation error is 69,300 cP, which is 0.693 of one standard deviation of all measured viscosity values. The correlation value of the predicted viscosities versus the measured viscosities is 0.76.



**Figure 5-7: *Top:* Emerge™ prediction error plot and cross-plot for viscosity using the new training model, and all the available well logs as the predicting attributes. In the crossplot, each color represents a different well. *Bottom:* The list of attributes with their associated validation errors. Note that each row in the list corresponds to a particular multi-attribute transform and includes all the attributes above it. *Explicit prediction equation is A1.1 in appendix A1.***

Figure 5-8 shows the prediction results using only the log-derived seismic properties from Figure 5-6 as the predicting attributes. This time, the optimum viscosity prediction is found using only the top two attributes: P-wave sonic and P-impedance. Beyond this, the validation error increases, meaning we would over-train the prediction using more than two attributes. The average validation error is 93,600 cP, which is 0.936 of one standard deviation of all measured viscosity values. The correlation value of the predicted versus measured viscosities is 0.35, significantly lower than the value of 0.76 when using all well logs.



**Figure 5-8: Top: Emerge™ prediction error plot and cross-plot for viscosity using the new training model, and calculated seismic properties as the predicting attributes. In the cross-plot, each color represents a different well. Bottom: The list of attributes with their associated validation errors. Note that each row in the list corresponds to a particular multi-attribute transform and includes all the attributes above it. *Explicit prediction equation is A1.3 in appendix A1.***

The explicit prediction equations showing the regression coefficients for each attribute are given in Appendix A1 (Equation A1.1 and Equation A1.3).

## 5.5 – Visualizing the viscosity predictions

This section is a series of figures to illustrate how the viscosity predictions actually behave in a few example wells. In each figure, the leftmost track shows the viscosity predictions using all well logs (from Figure 5-7), and the rightmost track shows the predictions using calculated seismic properties (from Figure 5-8). The true viscosities are superimposed in black for comparison. The gold zones highlight the reservoir intervals, and the magenta colored area is the separation between the predicted NMR Total and NMR Free porosity logs (the 3<sup>rd</sup> top predictor). For terminology, the “old prediction” refers to predictions using the old, interpolated training model (Figure 5-5 black curve). The “new prediction” refers to predictions using the updated, blocked training model (Figure 5-5 red log).

Figure 5-9 shows a well with bitumen extending 20m above the shallowest viscosity measurement. Both predictions (using well logs and calculated seismic properties) show good agreement with the measured viscosities, and they both predict a smooth trend of decreasing viscosity to the top of the bitumen reservoir. The spikes in the predicted viscosity logs occur in non-reservoir intervals, which makes sense because the predictions are only trained at the measurement points, all occurring in reservoir intervals. There is relatively little difference between the old and new viscosity predictions in this well.

Figure 5-10 shows a well with more dynamic behavior of the modeled viscosity. On the left side (prediction using well logs), the new viscosity prediction shows more variation than the old prediction. The new model shows a shallow decreasing viscosity profile from 410m to 420m, and three separate profiles of increasing viscosity in three reservoir intervals (430m to 460m) separated by shalier intervals, showing good agreement with the measured viscosities. This behavior of increasing viscosity gradients has been documented in other areas of the

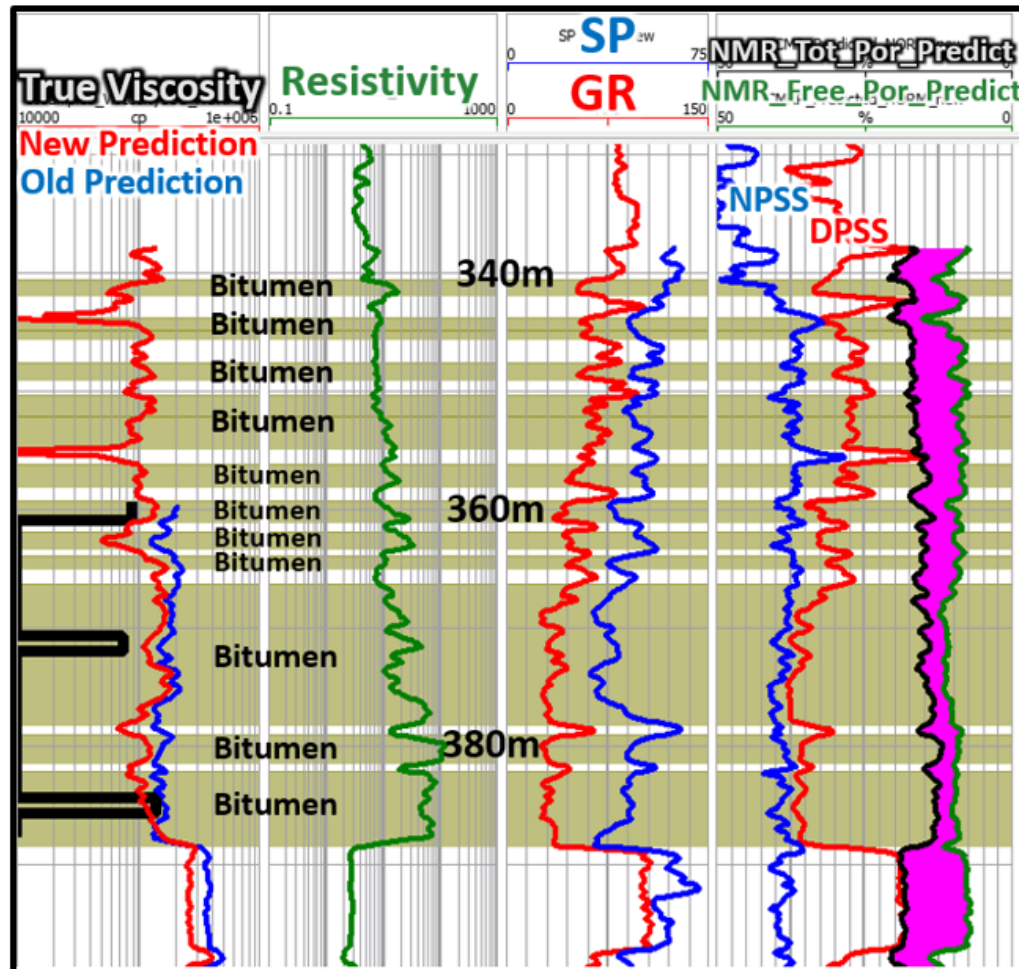
Athabasca oil sands (Larter et. al., 2008). It is encouraging that similar behavior is modelled here from well logs in the study area. In the right track of Figure 5-10, the viscosity prediction from calculated seismic properties shows less variation, and does not see the same trends. Note that most of the spikes in the predicted viscosities occur in the shaley zones. This is not a problem because we care only about the viscosity in the reservoir intervals.

Figure 5-11 shows a well with two viscosity gradients predicted from well logs (left side). One from 215m to 233m, and the other from 235m to 245m. The predicted viscosity closely matches the true viscosity at each of the three measurement depths. On the right side, the viscosity prediction from calculated seismic properties detects less variation than the well logs see, but still matches the true viscosities within reason.

Figure 5-12 shows a well where the predicted viscosity from well logs (left side) models a smooth increasing gradient from the top to base of the reservoir. There is a beautiful inverse correlation between the resistivity curve and the viscosity values. This inverse trend is observable in most wells (though not in Figure 5-9), and is the reason why resistivity emerged as the most important viscosity predicting attribute (Figure 5-7). The viscosity prediction from calculated seismic properties (right side) unfortunately does not model this trend so nicely.

In general, it has been observed that the new predictions yield greater viscosity variations than the old predictions. These variations are those we might expect to see in stacked bitumen intervals separated by shale layers. On the other hand, the viscosity predictions using calculated seismic properties detect less vertical variation than the well logs see, with higher validation error. This is not surprising since the prediction from seismic properties had a correlation value of only 0.35, compared to 0.76 when using all the well logs.

### Viscosity from standard logs, sonic, and NMR



### Viscosity from calculated seismic properties

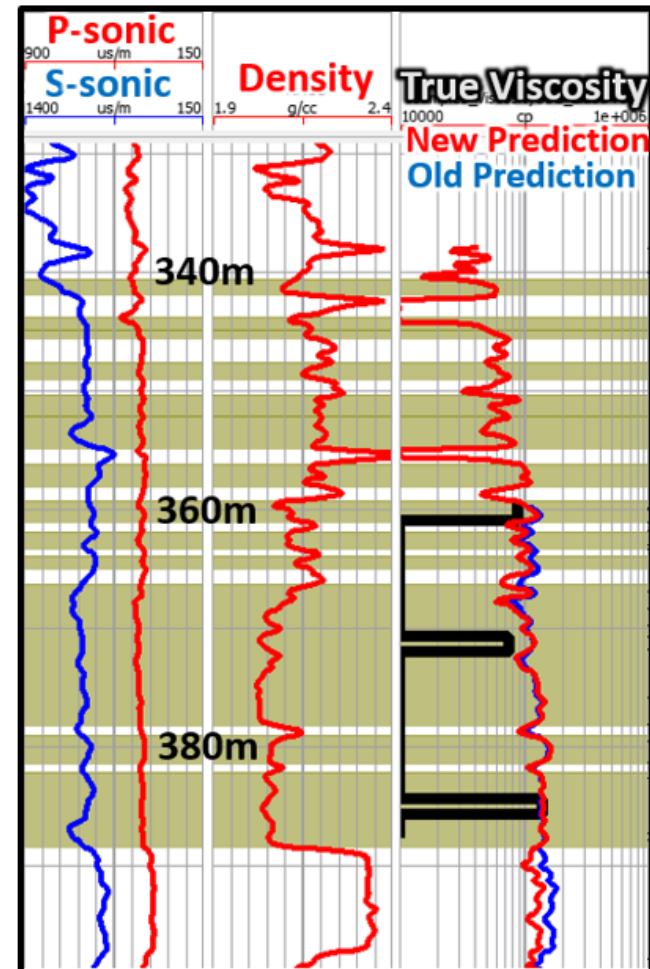
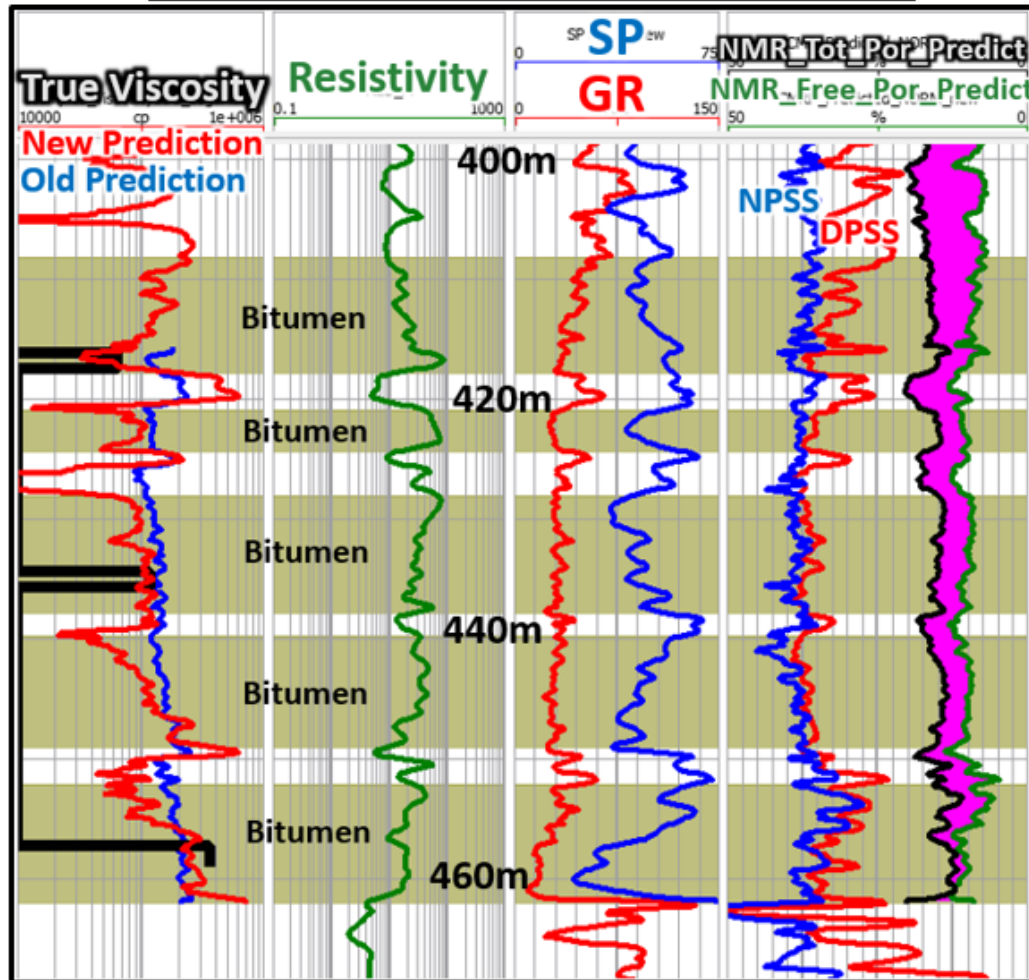


Figure 5-9: Viscosity predictions (validation results) for an example well where the viscosity trend continues 20m above the top measurement. The two outermost tracks show the true viscosity measurements (35<sup>0</sup>C) in black, with the new prediction in red overtop the old prediction in blue. The viscosity tracks are presented on logarithmic scales from 10,000 cP to 1,000,000 cP. The gold zones highlight the bitumen intervals. The magenta colored area is the separation between the predicted NMR Total and NMR Free porosity logs. Credit: Hampson-Russell Emerge™

### Viscosity from standard logs, sonic, and NMR



### Viscosity from calculated seismic properties

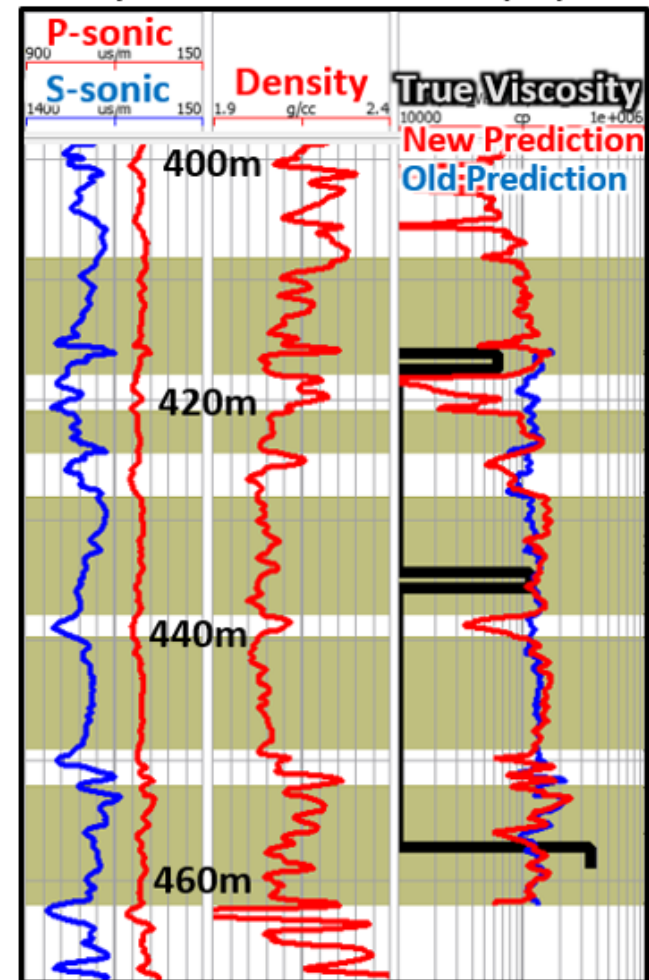
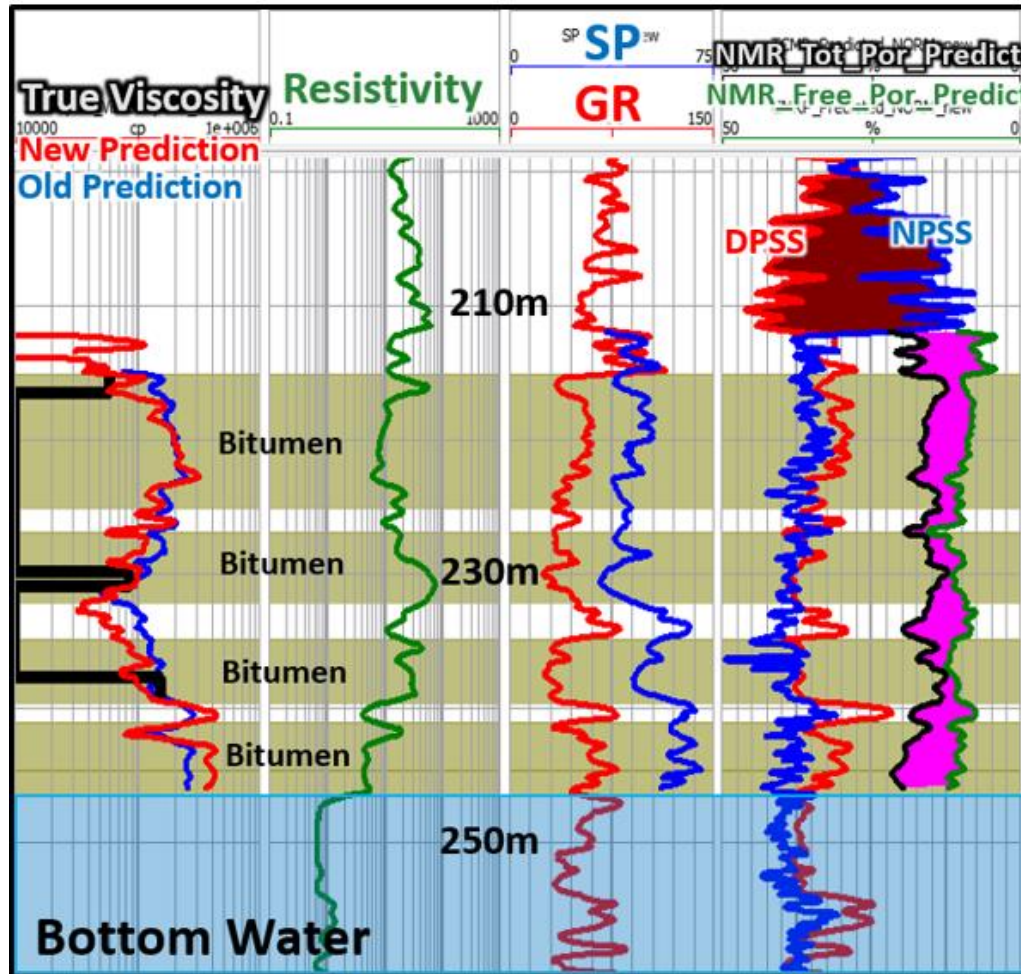


Figure 5-10: Viscosity predictions (validation results) for an example well where three viscosity gradients are modelled from 430m to 460m, separated by shaley zones. The two outermost tracks show the true viscosity measurements (35°C) in black, with the new prediction in red overtop the old prediction in blue. The viscosity tracks are presented on logarithmic scales from 10,000 cP to 1,000,000 cP. The gold zones highlight the bitumen intervals. The magenta colored area is the separation between the predicted NMR Total and NMR Free porosity logs. Credit: Hampson-Russell Emerge™

### Viscosity from standard logs, sonic, and NMR



### Viscosity from calculated seismic properties

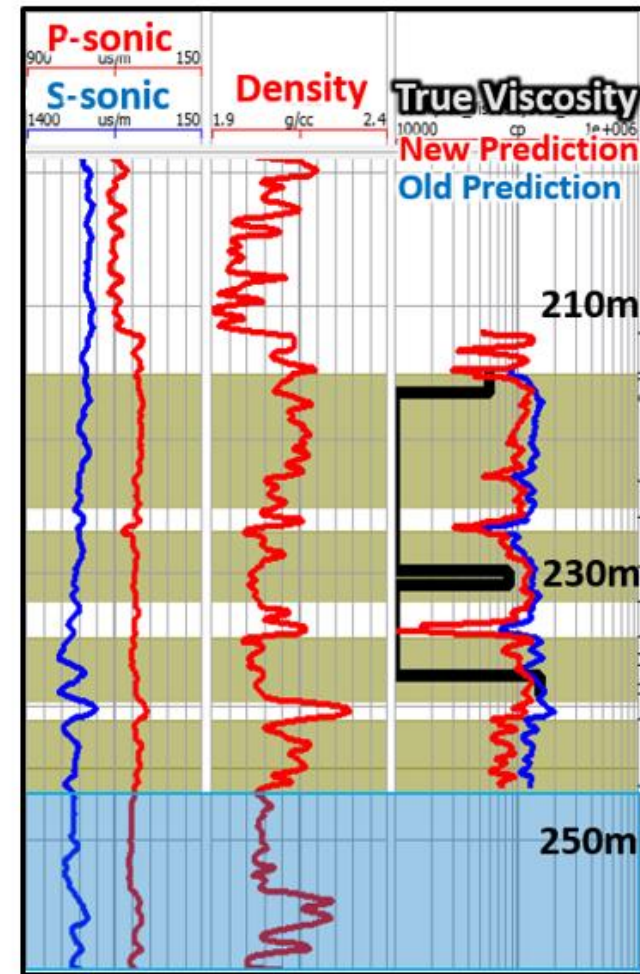
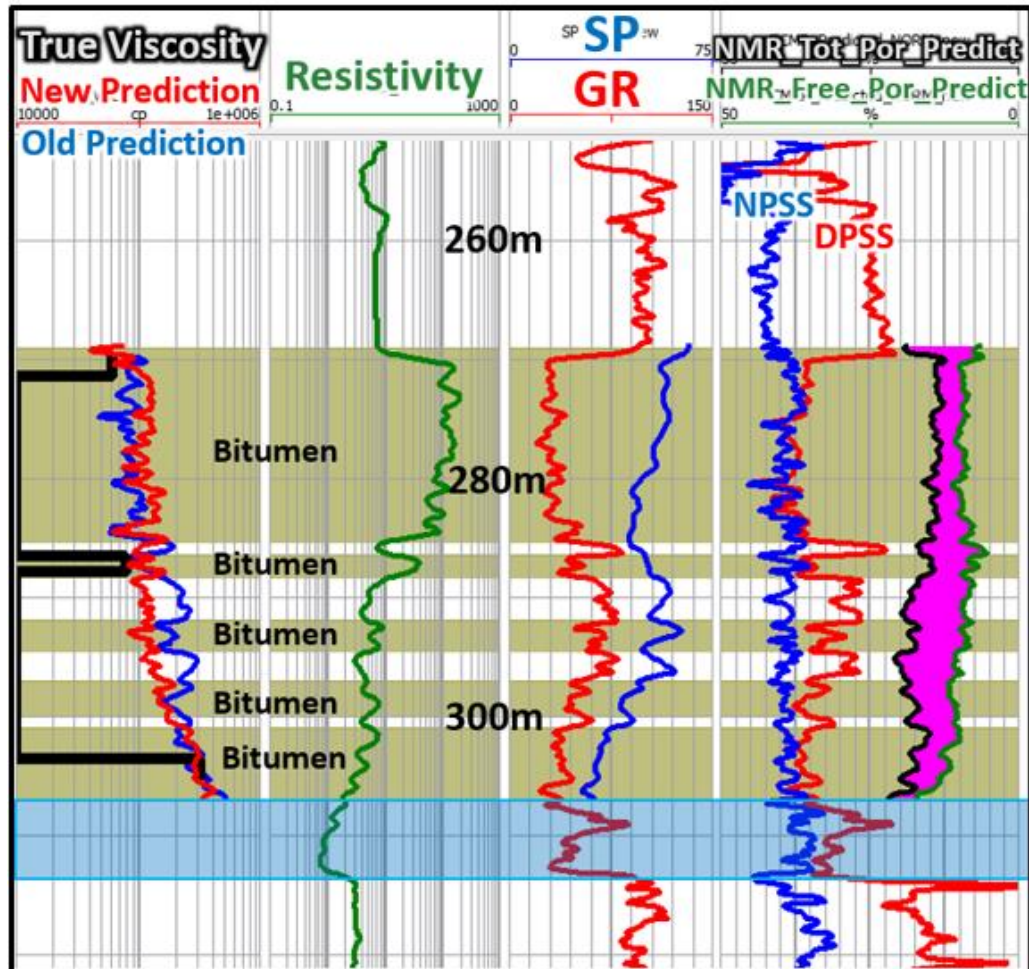


Figure 5-11: Viscosity predictions (validation results) for an example well where two viscosity gradients are modelled throughout the reservoir interval. The two outermost tracks show the true viscosity measurements ( $35^{\circ}\text{C}$ ) in black, with the new prediction in red overtop the old prediction in blue. The viscosity tracks are presented on logarithmic scales from 10,000 cP to 1,000,000 cP. The gold zones highlight the bitumen intervals. The magenta colored area is the separation between the predicted NMR Total and NMR Free porosity logs. Credit: Hampson-Russell Emerge™

### Viscosity from standard logs, sonic, and NMR



### Viscosity from calculated seismic properties

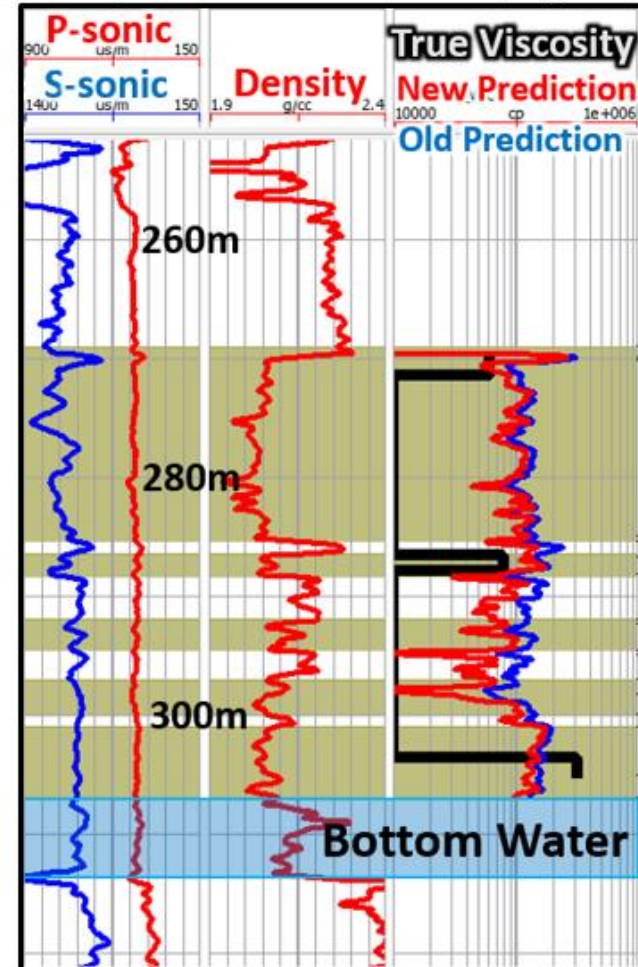
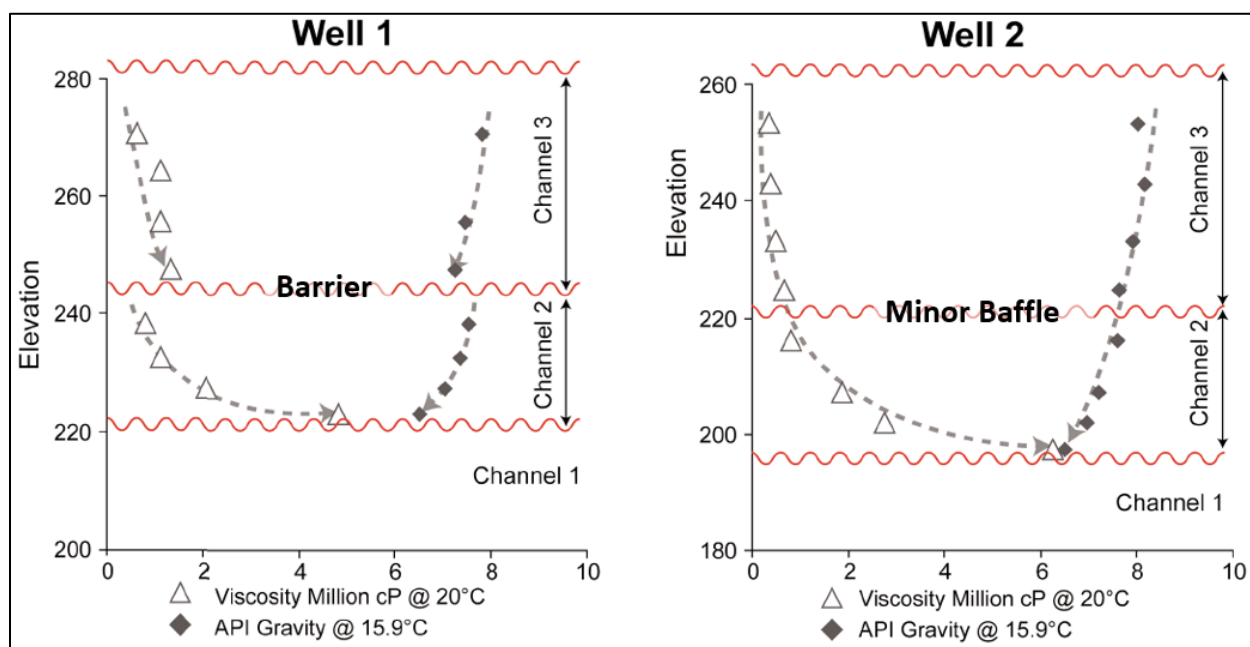


Figure 5-12: Viscosity predictions (validation results) for an example well with a smooth increasing viscosity gradient with depth, and a beautiful inverse correlation with resistivity. The two outermost tracks show the true viscosity measurements (35°C) in black, with the new prediction in red overtop the old prediction in blue. The viscosity tracks are presented on logarithmic scales from 10,000 cP to 1,000,000 cP. The gold zones highlight the bitumen intervals. The magenta colored area is the separation between the predicted NMR Total and NMR Free porosity logs. Credit: Hampson-Russell Emerge™

While predicting the viscosity value itself is important for reservoir development, the behavior of the viscosity profiles is also a critical consideration for steam-injection methods.

Figure 5-13 is from a study by Fustic et. al. (2011) of a nearby bitumen reservoir showing two wells with their lab-measured viscosity and API gravity profiles. Through an intensive geochemical study, the authors determined that the erosional surface between channel 2 and channel 3 in Well 1, characterized by two separate viscosity gradients, is likely a barrier to steam chamber development (meaning that steam flow cannot penetrate an impermeable layer). However, in Well 2, the viscosity and API gravity gradients are more continuous and the authors determined that the erosional surface is likely a minor baffle (meaning that steam flow may still be impeded, but only temporarily).

These observations can be directly related to the viscosity predictions from this thesis. For example, the three predicted viscosity gradients from 430m to 460m in Figure 5-10



**Figure 5-13: Viscosity measurements at 20°C and API gravity measurements plotted versus depth for two wells in a nearby bitumen reservoir. The authors propose that the erosional surface between channel 2 and channel 3 is a barrier in Well 1, and a minor baffle in Well 2. (modified from Fustic et. al., 2011).**

resemble the gradients from Well 1 of Fustic et. al. (2011), which suggests that the shaley zones at 440m and 450m could act as steam barriers. These viscosity gradients were hardly seen from the old prediction of Figure 5-10 (blue curve), which further supports that the new prediction is superior to the old prediction.

The smooth predicted viscosity gradient from Figure 5-12 resembles Well 2 from Fustic et. al. (2011), which suggests the shaley zones throughout the reservoir could act more as minor steam baffles, only temporarily impeding steam flow. A similar conclusion can be made regarding the shaley zone at 240m in Figure 5-11.

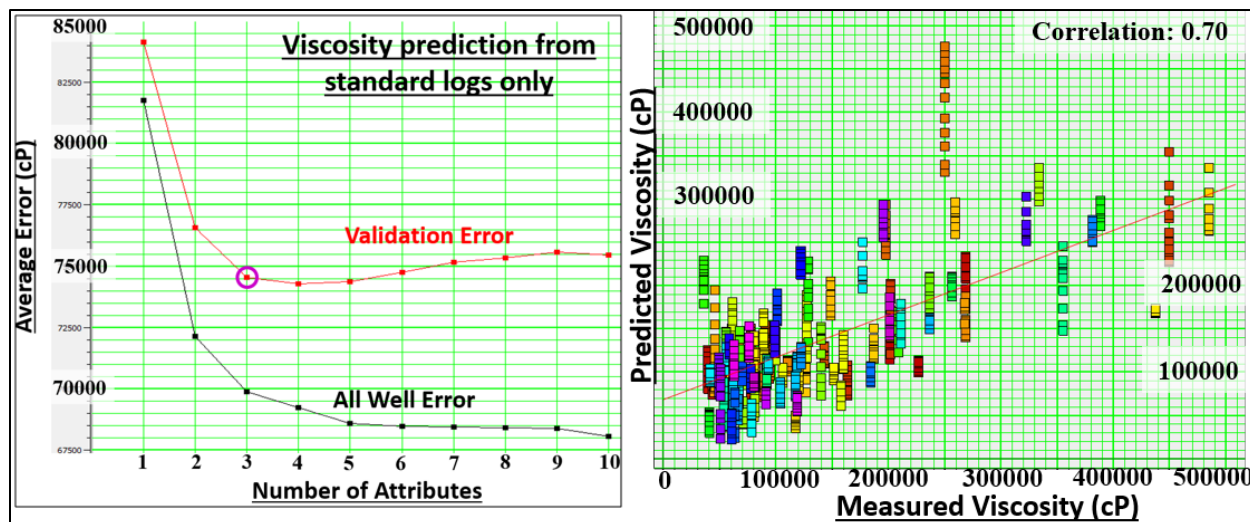
## **5.6 – Viscosity prediction using only standard logs, and predicting log<sub>10</sub>(viscosity)**

Due to cost, most wells do not have sonic logs, and far fewer have NMR logs. Therefore, another set of viscosity predictions were generated using only the standard, most commonly-run logs as the predicting attributes: *gamma-ray, resistivity, density, neutron porosity, spontaneous potential, and the photoelectric curve.*

This section also compares the prediction of viscosity versus the prediction of log<sub>10</sub>(viscosity). Since viscosity is a logarithmic variable (with respect to temperature), predicting the log<sub>10</sub>(viscosity) might be a more robust approach. This was done by forcing Emerge™ to predict log<sub>10</sub>(viscosity) as the target attribute, then converting back to linear space by  $10^{\text{[predicted log}_{10}(\text{viscosity})]}$  to compare with the absolute viscosity predictions.

Figure 5-14 shows the graphical training and validation errors from using only the standard well logs as predicting attributes, along with the list of attributes in descending order of importance. The result shows that the optimum viscosity prediction is made using the top three attributes. Beyond this, the validation error increases, meaning we would over-train the

prediction using more than three attributes. The average validation error is 74,600 cP, which is 0.75 of one standard deviation of all the measured viscosity values, and only 5,300cP greater than using all the well logs. The correlation value is 0.70, not much worse than the 0.76 value from using all well logs. The prediction equation is given in appendix A1 (Equation A1.2).



	<u>Target (cP)</u>	<u>Final Attribute</u>	<u>Units</u>	<u>Validation Error (cP)</u>
1	Viscosity	1 / (Medium Resistivity)	1 / (ohmm)	84,200
2	Viscosity	ln(Gamma Ray)	ln(GR-API)	76,600
3	Viscosity	1 / (SP)	1 / (mV)	74,600

**Figure 5-14: *Top:* Emerge™ prediction error plot and cross-plot for viscosity using the new training model, and only the standard logs as predicting attributes. In the crossplot, each color represents a different well. *Bottom:* The list of attributes with their associated validation errors. Note that each row in the list corresponds to a particular multi-attribute transform and includes all the attributes above it. *Explicit prediction equation is A1.2 in appendix A1.***

Figure 5-15 and Figure 5-16 show comparisons of the three viscosity prediction methods: using all available well logs (from Figure 5-7), using only standard well logs (from Figure 5-14), and using log-derived seismic final properties (from Figure 5-8). Also plotted as the green curves are the  $\log_{10}(\text{viscosity})$  predictions converted back to linear space.

There is little noticeable difference between the prediction using all well logs (left track) and the prediction using standard well logs (middle track). Using all well logs gives a slightly more accurate prediction, as seen by inspecting the viscosity measurement at 230m in

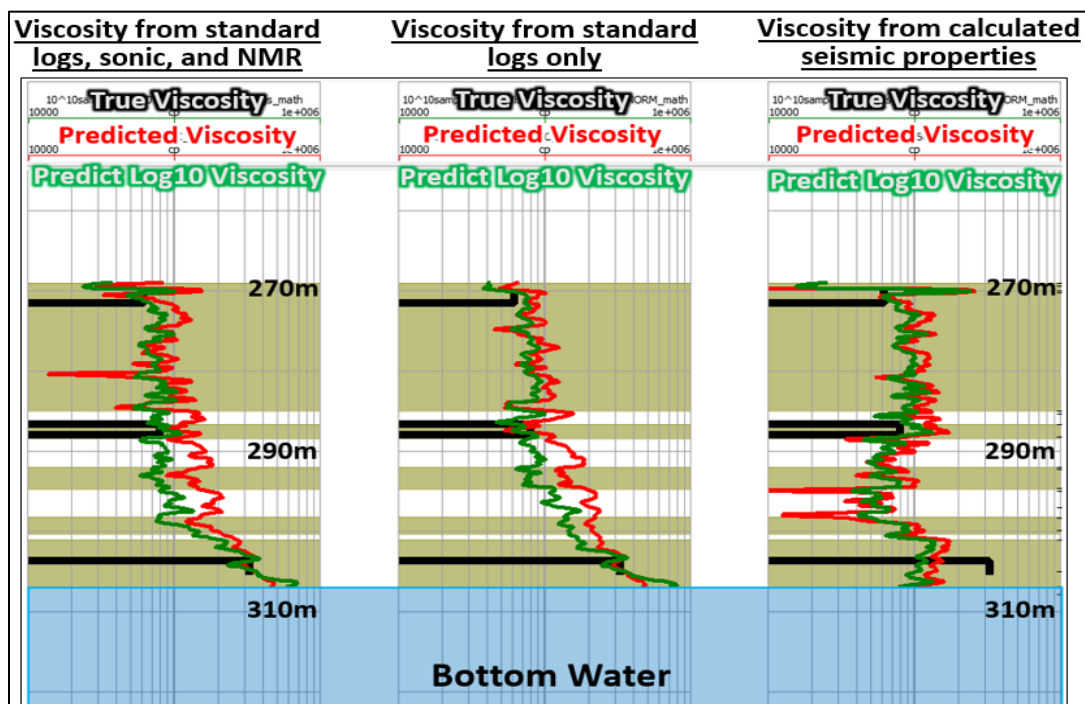


Figure 5-15: Comparison of the three viscosity prediction methods for an example well. The predicted  $\log_{10}(\text{viscosity})$  converted back to linear space is shown in green. The bitumen intervals are highlighted in gold.

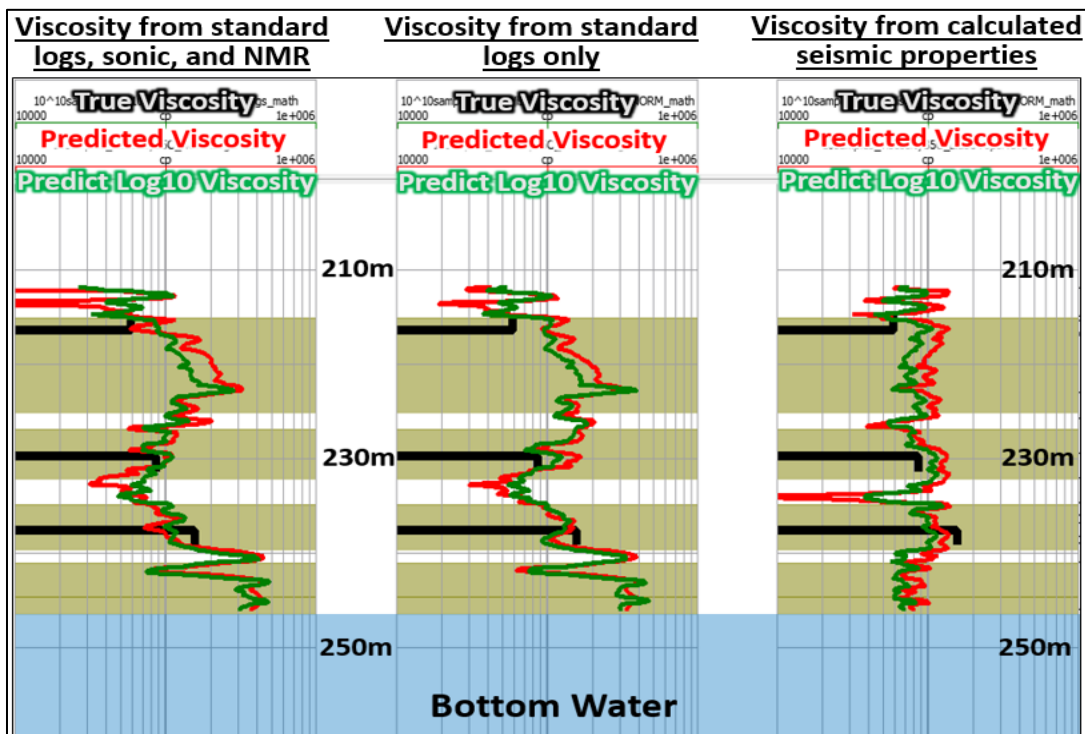


Figure 5-16: Comparison of the three viscosity prediction methods for an example well. The predicted  $\log_{10}(\text{viscosity})$  converted back to linear space is shown in green. The bitumen intervals are highlighted in gold.

the Figure 5-16 well, but the difference is not significant and both predictions capture the same trends. This is an encouraging result which demonstrates that viscosity can be predicted with almost the same level of detail in the absence of sonic and NMR logs.

Sections 5.4 and 5.5 already observed that the predictions from calculated seismic properties detect less vertical viscosity variations than the well logs see, with higher prediction error. This is especially obvious in the base reservoir sections in Figure 5-15 and Figure 5-16.

Comparing the viscosity predictions (red curves) versus the  $\log_{10}(\text{viscosity})$  predictions converted back to linear space (green curves), both capture the same overall trends with little difference in prediction error. The main difference is the  $\log_{10}(\text{viscosity})$  predictions appear moderately more stable and less spiky, especially in the shaley intervals for the seismic property predictions. This is the extent to which I investigated the prediction of  $\log_{10}(\text{viscosity})$ . However, for curious geoscientists interested in expanding the work of this thesis, note that predicting  $\log_{10}(\text{viscosity})$  appears to yield moderately more stable predictions with relatively equal prediction errors as predicting viscosity directly.

Table 5-4 is a visual comparison of the three prediction methods, with the top predicting attributes, average validation error, and correlation values for each.

<b><u>Viscosity from standard logs, sonic, and NMR:</u></b>	<b><u>Viscosity from standard logs only:</u></b>	<b><u>Viscosity from calculated seismic properties:</u></b>
1. (Resistivity) <sup>-1</sup> 2. ln  Gamma Ray  3. (NMR Total – NMR Free) <sup>1/2</sup> 4. (SP) <sup>-1</sup> 5. (P-wave sonic) <sup>-1</sup> 6. (S-wave sonic) <sup>-1</sup>	1. (Resistivity) <sup>-1</sup> 2. ln  Gamma Ray  3. (SP) <sup>-1</sup>	1. (P-wave sonic) <sup>-1</sup> 2. (P-impedance) <sup>-1</sup>
<i>Average validation error: <b>69,300cP</b> (0.693 of 1 standard deviation)</i>	<i>Average validation error: <b>74,600cP</b> (0.746 of 1 standard deviation)</i>	<i>Average validation error: <b>93,600cP</b> (0.936 of 1 standard deviation)</i>
<i>Correlation: <b>0.76</b></i>	<i>Correlation: <b>0.70</b></i>	<i>Correlation: <b>0.35</b></i>

**Table 5-4: Comparison of the three viscosity prediction methods. The explicit prediction equations are found in appendix A1.**

### 5.7 – Blind test on a well from a nearby reservoir

The multi-linear regression procedure automatically performs blind tests on each well during the cross-validation step, and determines the average prediction accuracy of all wells within the study area, as described in chapter 3. This section, however, shows the results of a blind test on a well *outside* of the study area.

Donor Company has another oil sands reservoir undergoing steam-assisted gravity drainage production 10km north of the thesis study area. Figure 5-17 shows the location of the blind test well (yellow star) relative to the study area wells (large black symbols). The blind test well was chosen because it has a wide range of measured viscosity values (230,000cP, 377,000cP, and 640,000cP measured at 35°C). The northern reservoir has a higher average viscosity than the study area reservoir, and so the prediction equations need to be multiplied by a calibration constant to yield viscosities in the correct magnitude range.

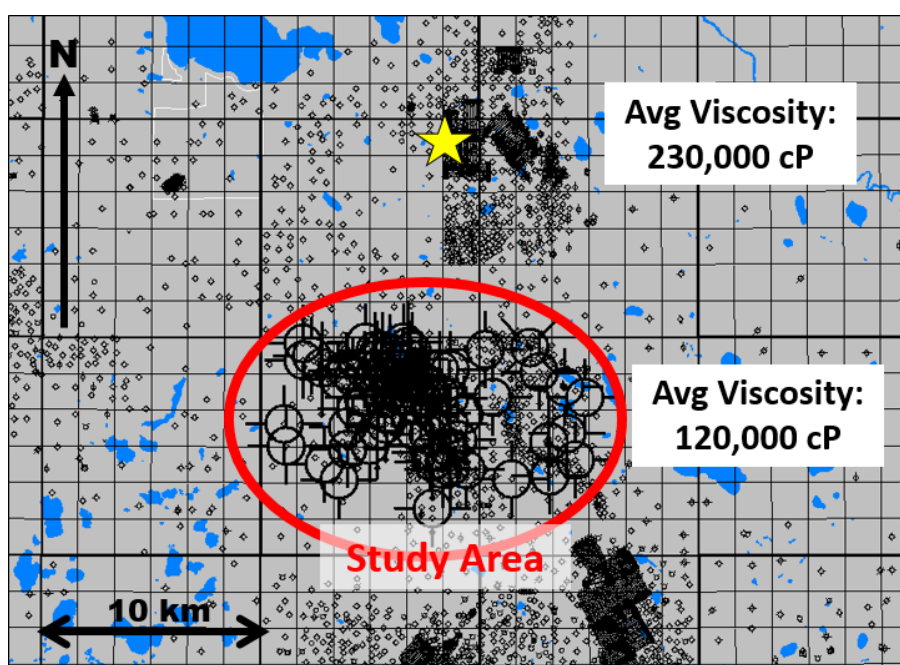
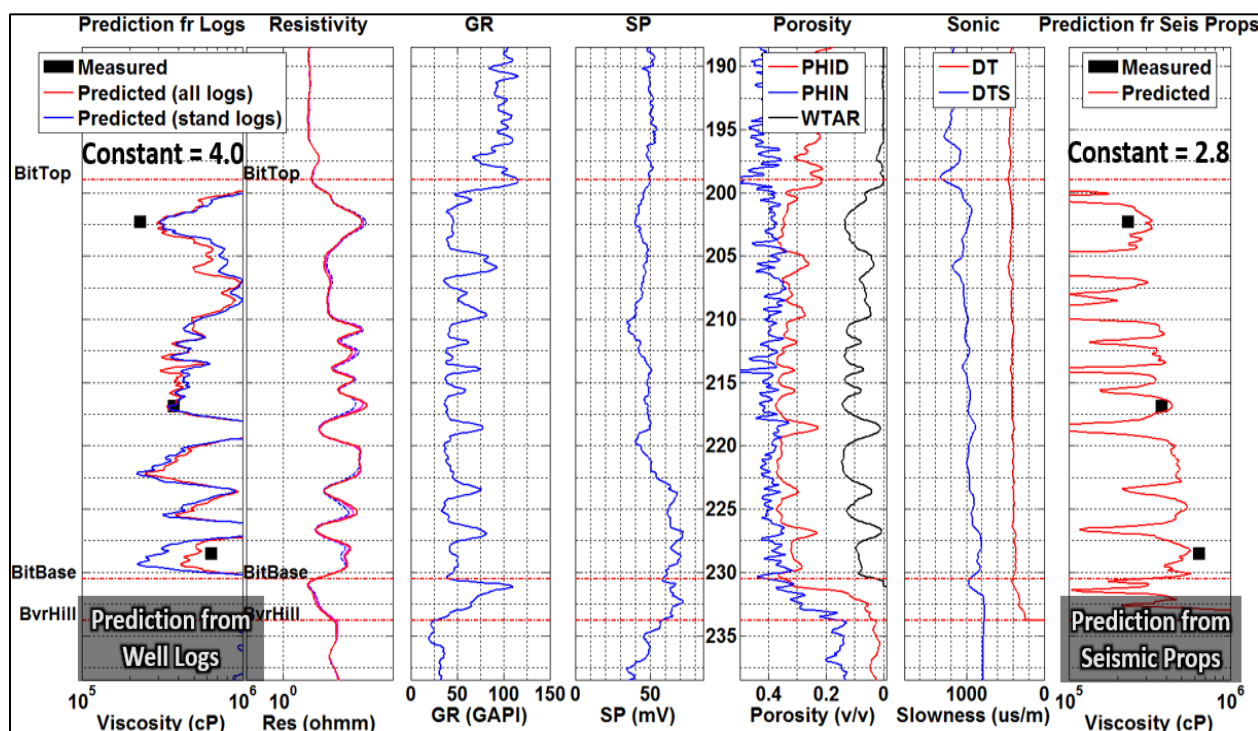


Figure 5-17: Location of the blind test well (yellow star) relative to the study area wells (large black symbols).

Figure 5-18 shows the viscosity predictions in the blind test well by applying a calibration constant of 4.0 to the well log prediction equations, and a calibration constant of 2.8 to the log-derived seismic properties prediction. The measured viscosities are shown by the black dots, with the predicted viscosities superimposed. Unlike the wells in the study area, here, the best prediction comes from log-derived seismic properties, which models an increasing viscosity gradient with depth matching the measured values reasonably well. Most of the spikes in the prediction occur within interbedded shale intervals.

Through correspondence with Donor Company geoscientists, the resistivity, SP, and S-wave sonic logs are less consistent and less reliable throughout this northern reservoir than in the study area. The prediction equation from log-derived seismic properties (P-wave sonic and



**Figure 5-18: Prediction results in the blind test well 10km north of the study area. This northern reservoir has a higher average viscosity than the study area reservoir, so the predictions were multiplied by constants to yield viscosities in the correct magnitude ranges.**

P-impedance) is the only one that does *not depend* on any of the problem logs, which is likely why the prediction from log-derived seismic properties does the best job in this blind test well. If the well logs were all consistent in the northern reservoir, the calibration constant should have been equal for all three prediction methods.

Despite the uncertainty of poor quality well log data in the northern reservoir, the prediction from log-derived seismic properties performed quite strongly in this test well. This demonstrates that it should be possible to use prediction equations developed in one reservoir and apply them to nearby reservoirs by applying a calibration constant.

### 5.8 – Adding depth as a viscosity predictor

Figure 5-19 shows the viscosity measurements from all 40 training wells plotted against depth. Depth was calculated as height above base of bitumen to keep things consistent because the reservoir depths vary from well to well. There is a logarithmic trend of increasing viscosity with reservoir depth. Similar trends have been documented in nearby oil sands projects, such as

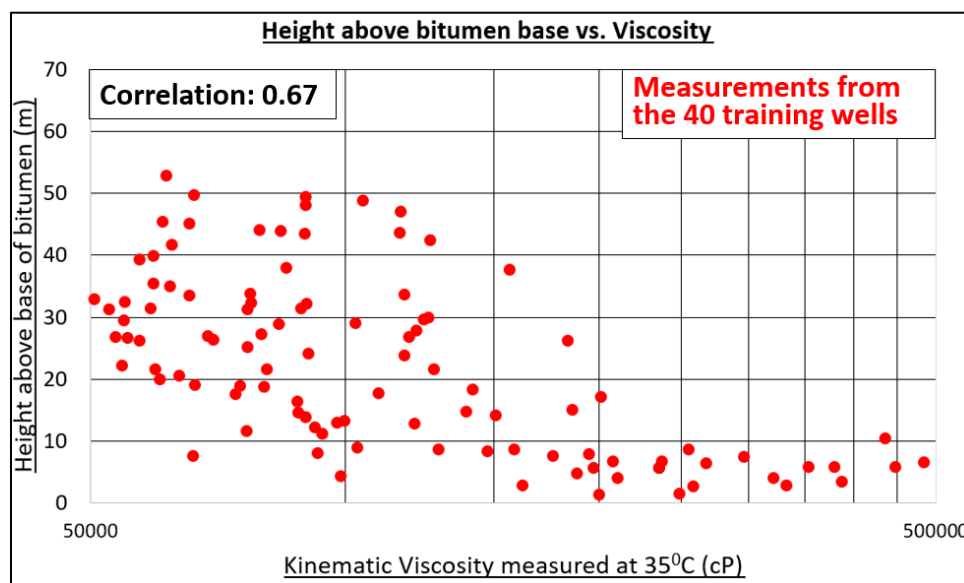
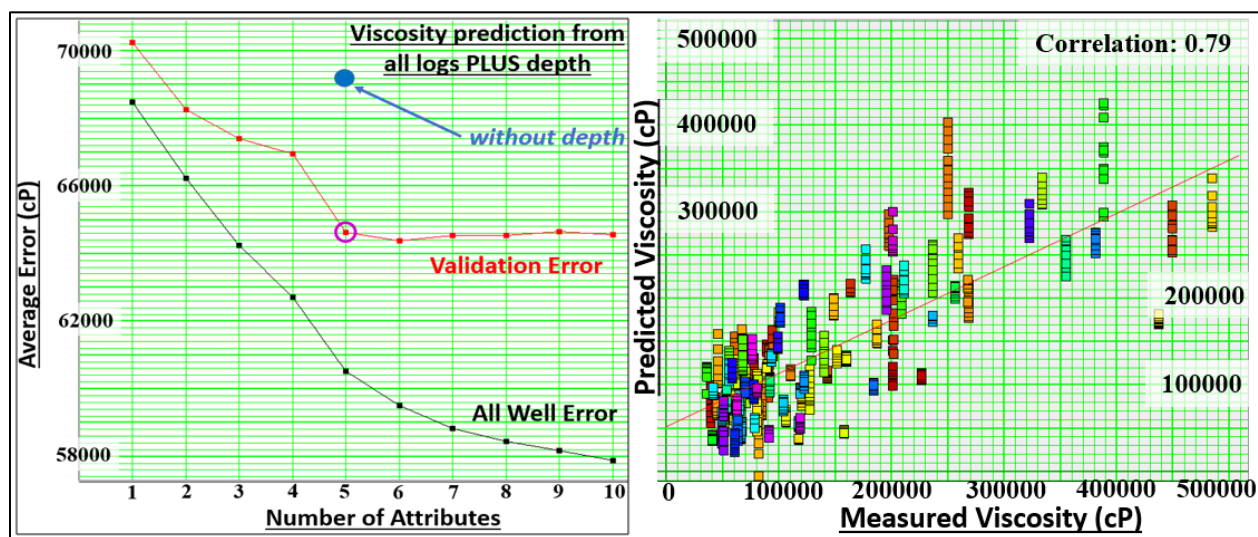


**Figure 5-19: Viscosity measurements from all 40 training wells plotted against depth. Logarithmic fit has a correlation value of 0.67.**

the ConocoPhillips Surmont project shown in appendix A3. While increasing bitumen viscosity gradients are well documented, a mechanism for their cause is not yet known, other than *something* (potentially the proximity to bottom-water) is causing the level of biodegradation to also increase with depth (Larter et. al., 2008).

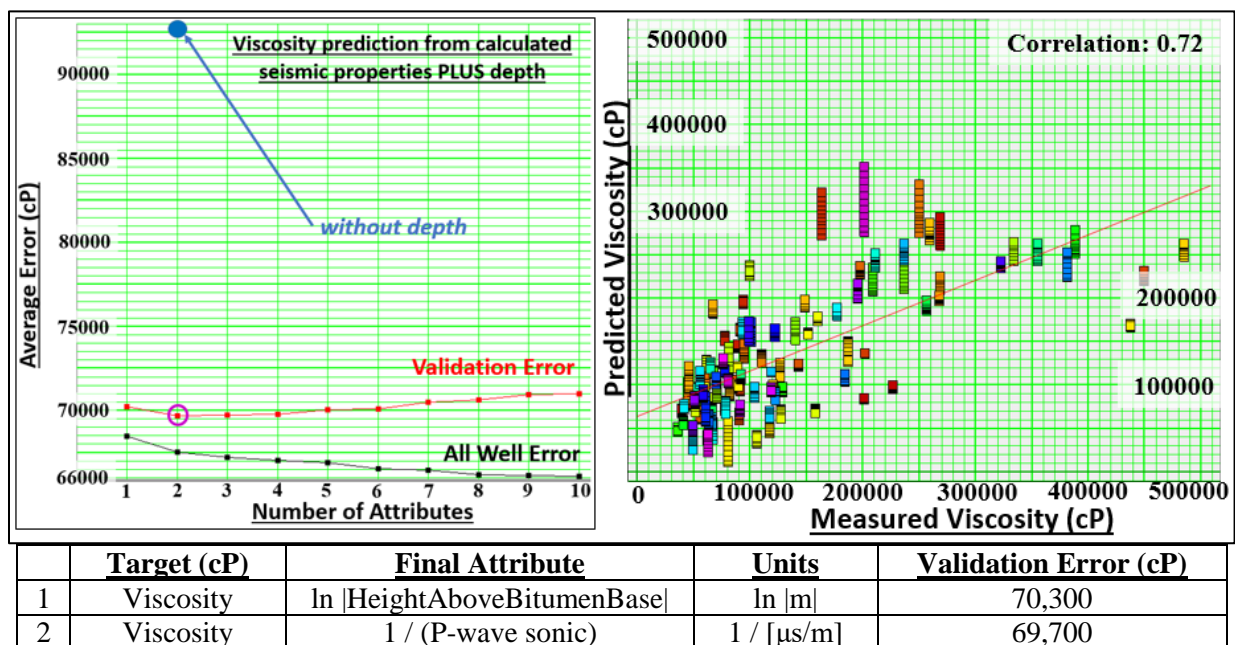
With this correlation in mind, bitumen base tops were picked in the 40 training wells to generate depth logs called “height above bitumen base.” The depth logs were then included as predicting attributes in the Emerge™ multi-linear regression analysis to see how depth influences the viscosity predictions.

Figure 5-20 and Figure 5-21 show the training and validation errors when depth is included as a predicting attribute for all logs, and log-derived seismic properties, respectively.



	<u>Target (cP)</u>	<u>Final Attribute</u>	<u>Units</u>	<u>Validation Error (cP)</u>
1	Viscosity	$\ln  \text{HeightAboveBitumenBase} $	$\ln  m $	70,300
2	Viscosity	$1 / (\text{SP})$	$1 / [mV]$	68,300
3	Viscosity	$1 / (\text{Medium Resistivity})$	$1 / [\text{ohmm}]$	67,400
4	Viscosity	$1 / (\text{Gamma Ray})$	$1 / [\text{GR-API}]$	67,000
5	Viscosity	$(\text{NMR Total} - \text{NMR Free})^{1/2}$	$[\text{decimal}]^{1/2}$	64,600

**Figure 5-20: Top: Emerge™ viscosity prediction error plot and cross-plot, using all well logs plus depth as predicting attributes. For the cross-plot, each color represents a different well. Bottom: The list of attributes with their associated validation errors. *Explicit prediction equation is A1.4 in appendix A1.***



**Figure 5-21: *Top:* Emerge™ viscosity prediction error plot and cross-plot, using log-derived seismic properties plus depth as predicting attributes. For the cross-plot, each color represents a different well. *Bottom:* The list of attributes with their associated validation errors. *Explicit prediction equation is A1.5 in appendix A1.***

From Figure 5-20, including depth has improved the overall viscosity prediction using *all logs* from 69,300cP to 64,600cP, and improved the correlation value from 0.75 to 0.79.

From Figure 5-21, including depth has improved the prediction using *log-derived seismic properties* from 93,600cP to 69,700cP. However, the scaling on the error plot shows that including seismic properties after depth does little to improve the overall prediction error.

Figure 5-22 shows visually how depth influences the viscosity prediction for three example wells. It is generally observed that the predictions including depth (the red curves) are closer to the true values than the predictions without depth (blue curves). The exception is the well on the right, which has a low measured viscosity at the base (66,000cP at 440m depth), whereas the depth predictor always expects viscosity to increase with depth (the green curve).

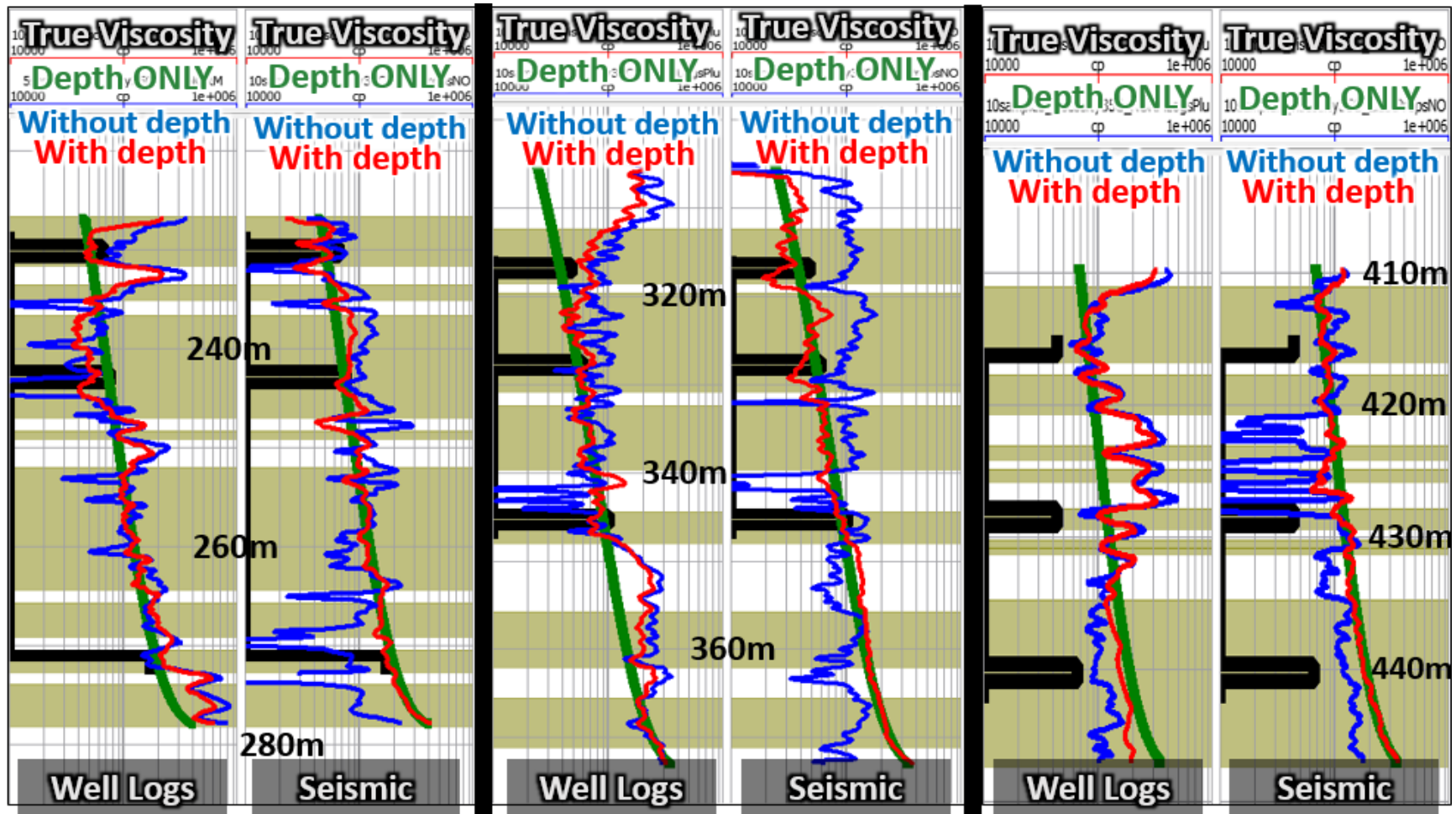


Figure 5-22: Influence of depth as a viscosity predictor for three example wells. In each well, the black blocked log shows the true viscosity measurements, and the green logarithmic curve is the prediction using *only depth*. In the left tracks, the viscosity predictions from *all logs* are plotted in blue, and the predictions from all logs *plus depth* are plotted in red. In the right tracks, the viscosity predictions from *calculated seismic properties* are plotted in blue, and the predictions from seismic *plus depth* are plotted in red. All tracks are presented on logarithmic scales from 10,000cP to 1,000,000cP. The gold zones highlight the bitumen intervals. Credit: Hampson-Russell Emerge™

It is interesting to note for the left and middle wells in Figure 5-22, depth alone predicts the measured viscosities almost perfectly as a logarithmic function (the green curves). However, this loses all the high resolution detail obtained from well logs. Combining depth with the well logs (red curves) captures the high resolution detail, while including the depth-viscosity trend from Figure 5-19. This is somewhat a similar concept to adding the low frequency component for seismic impedance inversions.

In summary, it was observed that including depth usually yields predictions closer to the measured values, however depth will always overestimate viscosity in the special cases where the base reservoir viscosity is low (as seen in the right well).

The results up to this point comprise the majority of the work done for this thesis. The next sections outline two quick experiments I did to investigate how applicable seismic data might be for predicting viscosity, and in detecting bitumen-water contacts.

## 5.9 – Predicting viscosity using acoustic logs filtered to seismic frequencies

This chapter has already shown the accuracy of using log-derived seismic properties to predict viscosity. However, this was done at well logging frequencies on the order of 10,000Hz. The P-wave sonic, S-wave sonic, and density logs were therefore low-pass filtered to 0–100/120 Hz as a proxy for what might be extracted from seismic inversion volumes. This process is informally known as “upscaling” of well logs.

Table 5-5 shows the top viscosity predictors when the three upscaled acoustic logs are

	<b>Target (cP)</b>	<b>Attribute</b>	<b>Units</b>	<b>Validation Error (cP)</b>
1	Viscosity	(upscaled P-wave sonic) <sup>2</sup>	( $\mu\text{s}/\text{m}$ ) <sup>2</sup>	95,700
2	Viscosity	(upscaled S-wave sonic) <sup>2</sup>	( $\mu\text{s}/\text{m}$ ) <sup>2</sup>	94,700
3	Viscosity	(upscaled density) <sup>2</sup>	( $\text{kg}/\text{m}^3$ ) <sup>2</sup>	94,400

**Table 5-5: Emerge™ top viscosity predicting attributes using acoustic logs upscaled to seismic frequencies (lowpass filtered from 0 – 100/120 Hz, 1 ms sample rate).**

input as the predicting attributes, using the same 40 training wells. Each attribute in turn slightly reduces the validation error.

Figure 5-23 and Figure 5-24 show how the upscaled acoustic logs look relative to the original logs, and how the viscosity predictions from upscaled acoustic logs look relative to the original acoustic predictions (from Figure 5-8) for two example wells.

The well in Figure 5-23 has a fairly continuous 20m thick bitumen interval, seen from the density log. The upscaled logs are smoothed versions of the originals. However, since this well has a relatively continuous reservoir interval (which is rare for the study area), the upscaled logs

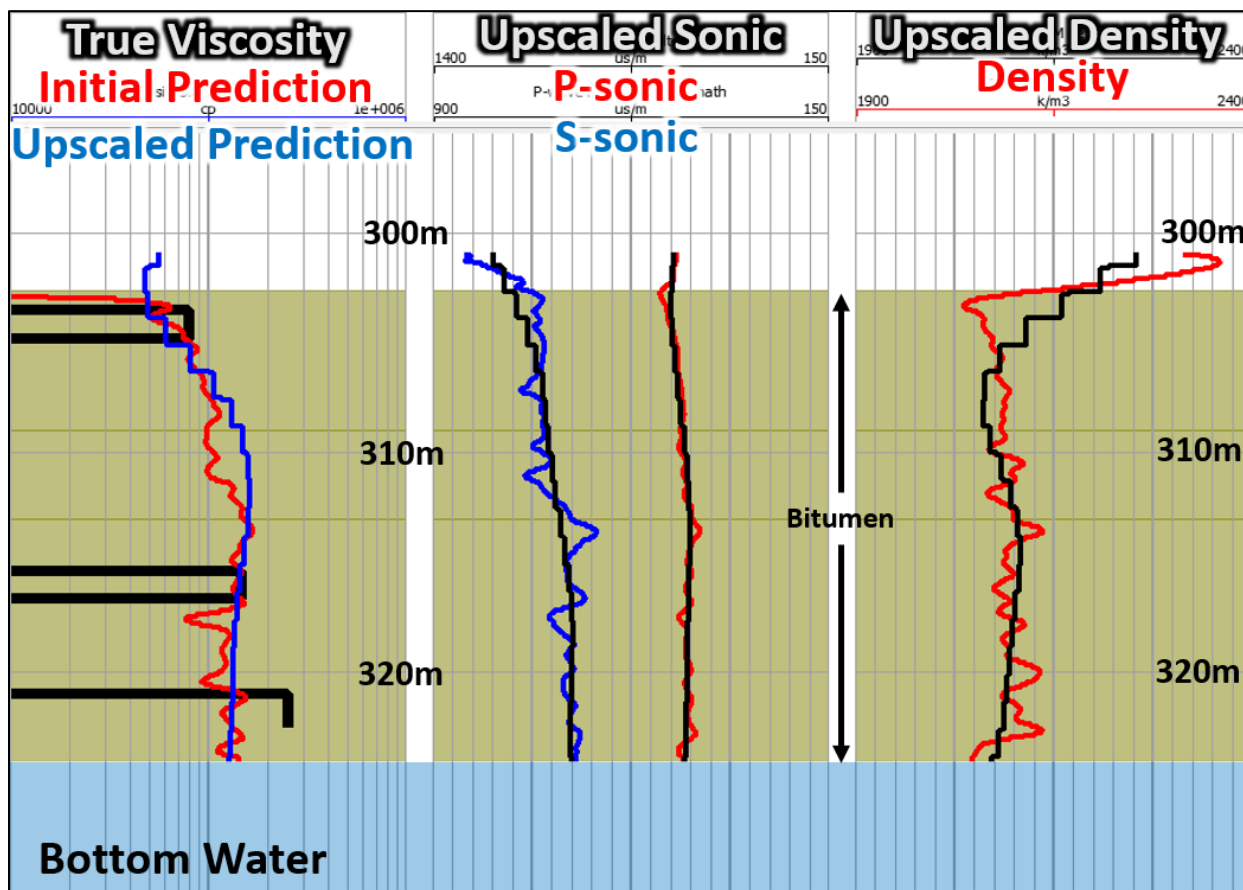
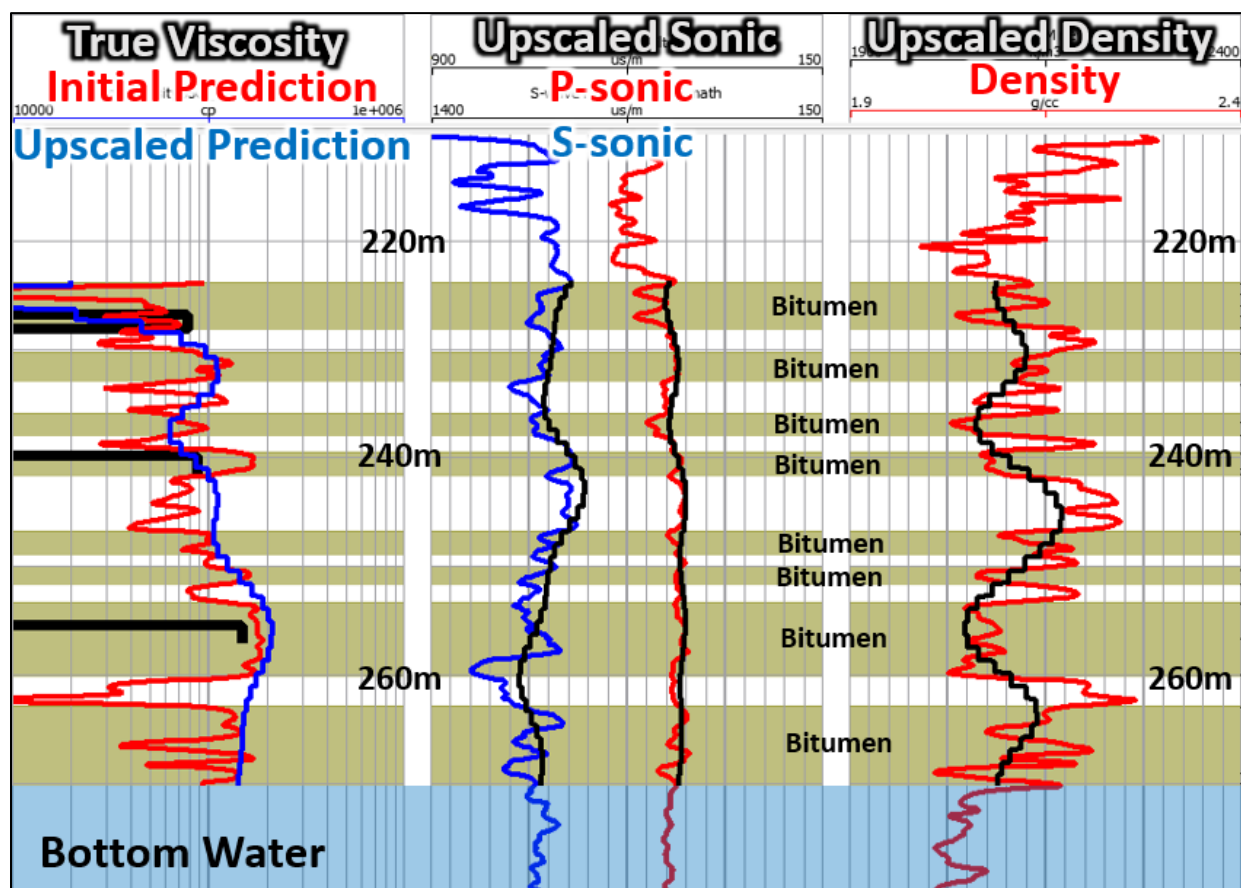


Figure 5-23: Predicting viscosity from upscaled acoustic logs for a well with a continuous 20m reservoir interval. The left track shows the true viscosity measurements in black, with the upscaled acoustic prediction in blue overlaying the original acoustic prediction in red. The other tracks show the upscaled acoustic logs in black overtop their original logs. The bitumen interval is highlighted in gold. The logs were lowpass filtered from 0-100/120Hz, with a 1ms sample rate.

still capture the main trends of the originals and the upscaled viscosity prediction is very similar to the original acoustic viscosity prediction. This result suggests that using  $V_p$ ,  $V_s$ , and density inversion volumes may provide an estimate of viscosity variations in areas with relatively continuous, thick reservoir.

Figure 5-24 shows the same results for a well with several interbedded shales throughout the reservoir, seen from the density log spikes. In this well, the upscaled logs lose considerable resolution because the frequent lithology changes are too thin to be detected at seismic frequencies. As a result, the upscaled viscosity prediction is considerably less detailed than the



**Figure 5-24: Predicting viscosity from upscaled acoustic logs for a well with several interbedded shale intervals. The left track shows the true viscosity measurements in black, with the upscaled acoustic prediction in blue overtop the original acoustic prediction in red. The other tracks show the upscaled acoustic logs in black overtop their original logs. The bitumen intervals are highlighted in gold. The logs were lowpass filtered from 0-100/120Hz, with a 1ms sample rate.**

original acoustic prediction. However, the upscaled prediction still matches the bottom two measurements, and the curve itself appears to be a believable, smoothed gradient of increasing viscosity with depth: still valuable information to have. The top reservoir prediction failed because the thin, clean sand response at the top measurement point was completely filtered out in each of the upscaled acoustic logs.

Both these examples suggest that using  $V_p$ ,  $V_s$ , and density inversion volumes could yield viscosity predictions that are considerably-smoothed versions of the true variations depending on the seismic frequencies in the reservoir.

Seismic properties, unfortunately, will never yield predictions as detailed as obtained by using all well log types (because they are all combinations of  $V_p$ ,  $V_s$ , and density). This fact is clear from the figures in section 5.5. However, from this quick investigation, it appears seismic inversion volumes could be capable of detecting large scale (low frequency) viscosity variations throughout the reservoir: still valuable information for development planning.

### **5.10 – Predicting resistivity from log-derived seismic properties**

Some of the study area wells have bottom water directly underneath the bitumen, as labeled in several figures from this chapter. A critical component of characterizing oil sands reservoirs is recognizing where the bitumen-water contact occurs: easily identified from well logs but difficult to detect in seismic data (Kelly, 2012).

The resistivity log is the most obvious indicator of a bitumen-water transition, and so another set of predictions were generated in Emerge™ using resistivity as the target log, and the log-derived seismic properties from Figure 5-6 as the predicting attributes. All 40 training wells, with the training window defined from top bitumen to 20m below base bitumen, were used to

adequately sample both the bitumen and the rock underneath (with or without bottom water). The results are shown in Table 5-6. The validation error begins to increase beyond two attributes which means using two attributes gives the optimal resistivity prediction.

	<b>Target (ohmm)</b>	<b>Attribute</b>	<b>Units</b>	<b>Validation Error (ohmm)</b>
1	Resistivity	1 / Density	1 / kg/m <sup>3</sup>	42.8
2	Resistivity	(P-wave sonic) <sup>1/2</sup>	(μs/m) <sup>1/2</sup>	42.3

**Table 5-6: Emerge™ top resistivity predicting attributes from calculated seismic properties. All 40 training wells were used, with the training windows defined from top bitumen to 20m below base bitumen in each well.**

Since resistivity behaves logarithmically, predictions for log<sub>10</sub>(resistivity) were also generated, similar to the procedure of section 5.6 for viscosity. This was done by forcing Emerge™ to predict log<sub>10</sub>(resistivity) as the target attribute, then converting back to resistivity units using 10<sup>[predicted log<sub>10</sub>(resistivity)]</sup> to compare with the absolute viscosity predictions.

Figure 5-25 shows the resistivity prediction results for three example wells. The left tracks show the true resistivities in black with the predictions overlain in red. The log<sub>10</sub>(resistivity) predictions converted back to resistivity units are shown in green.

It was observed that the resistivity predictions lose detail in the bitumen zone, but do a pretty good job above and below the reservoir interval. This is not unexpected because there is already a known, rough correlation between resistivity and V<sub>p</sub>, first given by Faust (1953). Also, there is little difference between the log<sub>10</sub>(resistivity) predictions and the original predictions, except that the log<sub>10</sub> prediction is a smoother, left-shifted version of the original.

Notably, the left and middle wells in Figure 5-25 have bottom water directly underneath the bitumen, as highlighted in blue. However, the resistivity predictions are essentially unchanged above and below the bitumen-water contact, as are the sonic and density logs. An explanation for this is shown in Figure 5-26, which shows the distribution of the bitumen

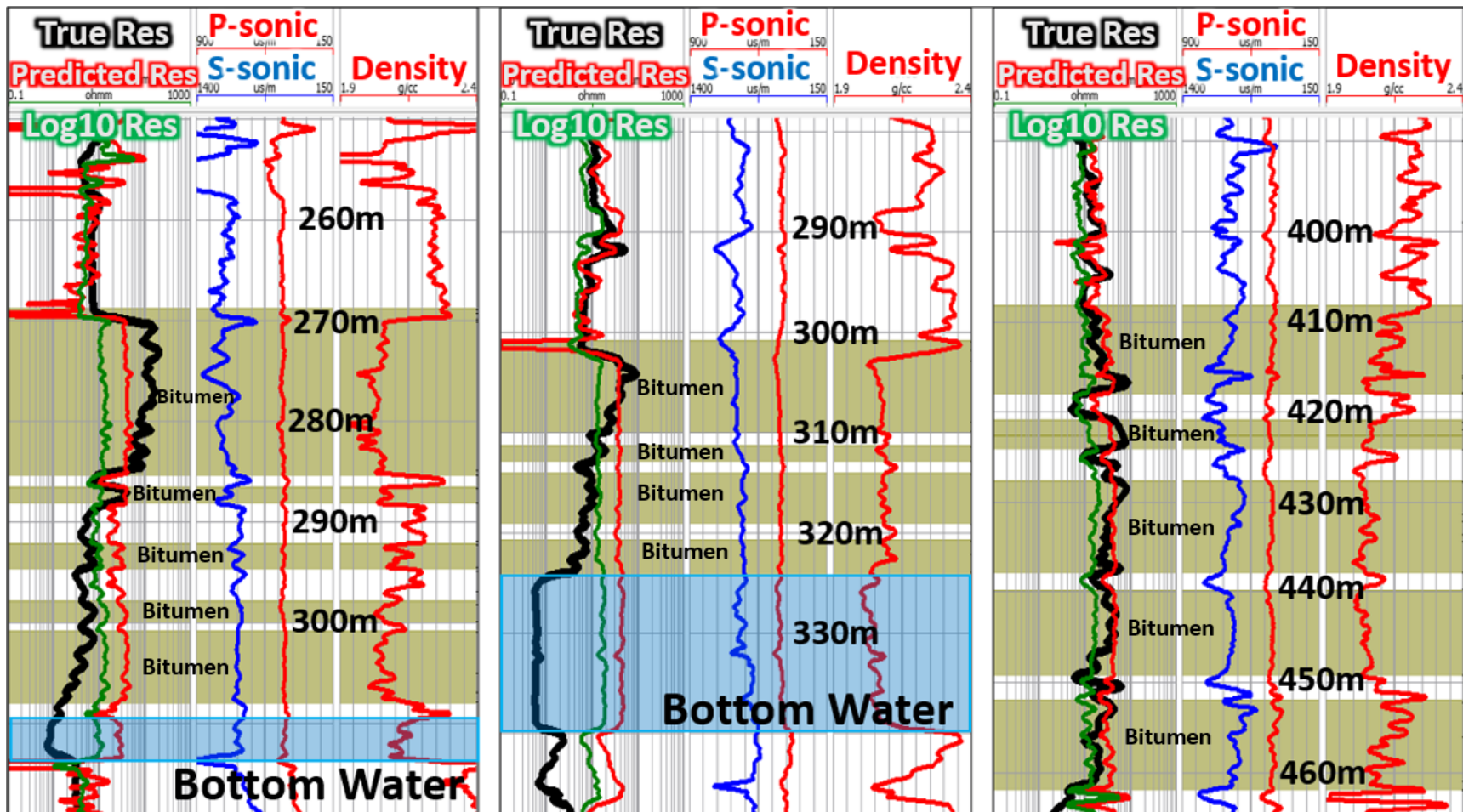
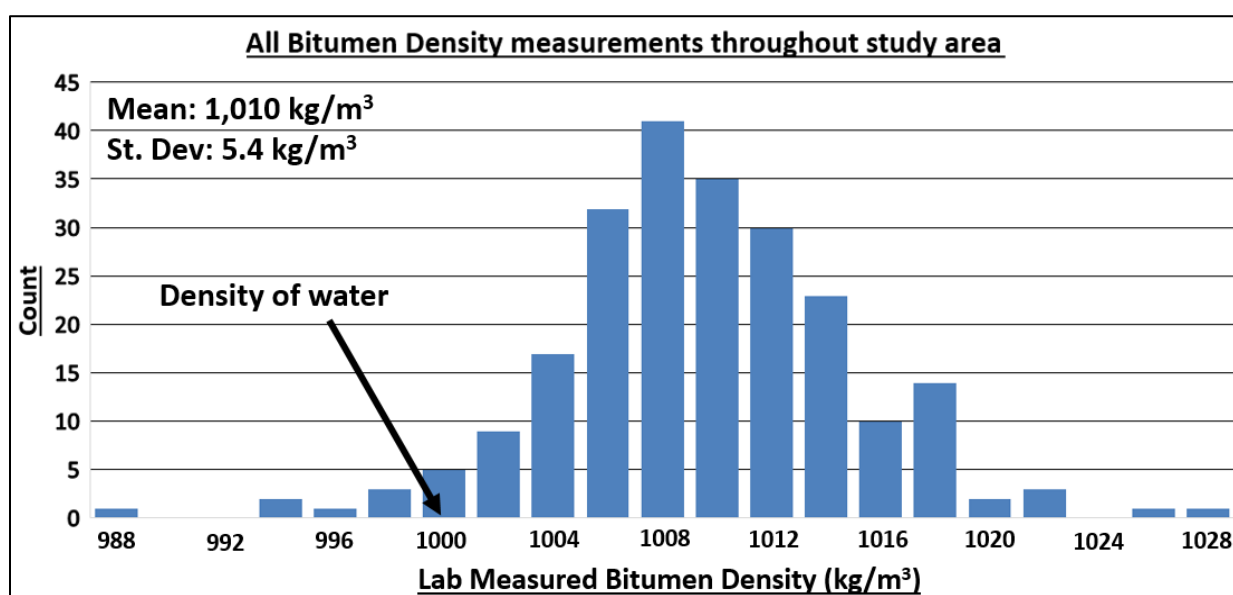


Figure 5-25: Resistivity prediction from log-derived seismic properties for three example wells. In the left track for each well, the true resistivity log is black, and the predicted resistivity is red. Also shown is the predicted log<sub>10</sub>(resistivity) converted back to linear space plotted in green. The resistivity logs are presented on logarithmic scales from 0.1 ohmm to 1,000 ohmm. The gold zones highlight the bitumen intervals. Credit: Hampson-Russell Emerge™

density measurements for all 78 project wells (from Figure 4-5). The average bitumen density is 1,010 kg/m<sup>3</sup>, which is so similar to the density of water (1,000 kg/m<sup>3</sup>) that the acoustic impedance contrast is likely too small to be measured by the sonic and density logs. Therefore, it is unlikely that 3D seismic data over this reservoir will reveal any sort of bitumen-water contact response.



**Figure 5-26: Histogram of all bitumen density measurements throughout the study area.**

## Chapter 6 – Discussion and Conclusions

### 6.1 – Comments regarding the well logs used to predict viscosity

The well log types that emerged as viscosity predictors throughout this thesis (see Table 5-4) were: *resistivity*, *gamma ray*, *SP*, *predicted NMR total porosity*, *predicted NMR free porosity*, *P-wave sonic*, and *S-wave sonic*. Possible physical relations to viscosity are explored in this section.

Resistivity was overall the top viscosity predictor due to their apparent inverse relationship (most clearly seen in Figure 5-12). Resistivity is the only log that is directly sensitive to changing reservoir fluid properties, so it seems logical that some sort of viscosity-resistivity correlation should exist, although the exact mechanism is not known. Decreasing resistivity with depth implies an increasing degree of freshwater. This could mean that biodegradation is leaching out salt at greater depths, and that the resistivity log is detecting the biodegradation, and hence viscosity, variations.

The degree of bitumen saturation might influence the viscosity, in which case the formation water resistivity ( $R_w$ ), which varies vertically and laterally, would be important. Through consultation with Donor Company petrophysicists, a first-pass bitumen saturation is calculated for all wells in the study area using the Poupon-Leveaux model for porous shaley sands:

$$S_w = \left\{ \left[ \left( \frac{V_{SH}^{2-V_{SH}}}{R_{SH}} \right)^{1/2} + \left( \frac{\phi_E^m}{a * R_w} \right)^{1/2} \right] R_T \right\}^{-1/n} \quad (6.1)$$

where  $S_w$  is bitumen saturation as a volume fraction,  $V_{SH}$  is the volume of shale determined from the gamma-ray, density, and neutron logs,  $R_{SH}$  is the resistivity value of pure shale in ohmm,  $R_w$  is the formation water resistivity in ohmm,  $\phi_E$  is effective porosity in porosity fraction units,  $R_T$  is

the true formation resistivity in ohmm (usually taken as the deep resistivity curve), and  $a$ ,  $m$ , and  $n$  are the Archie constants, which Donor Company has tweaked to match core data. It is quite possible that  $S_w$  and  $R_w$  could each influence viscosity in their own way, but detailed core analysis would be needed to explore this further.

Gamma-ray was another common viscosity predictor. The gamma-ray log measures the total natural radioactivity of the formation (potassium, thorium, and uranium concentrations), is commonly used to calculate shale volumes, and to differentiate between sand and shale units (Rider & Kennedy 2011). The physical reason why the gamma ray log would be related to viscosity is unclear, perhaps some unique bug deposits or uranium variations with viscosity? Perhaps the loss of lighter hydrocarbon chains with depth alters the potassium, thorium, or uranium concentrations? Spectral gamma ray logs, which have separate curves for potassium, thorium, and uranium would be critical in helping to determine if any real correlation to viscosity exists.

The SP log was another top viscosity predictor. As discussed in section 2.4, SP is sensitive to large changes in permeability, so perhaps it could also respond to viscosity variations in a similar manner. The SP signal is also sensitive to varying  $R_w$  (as in Equation 2.2), and  $R_w$  might be a viscosity-influencing factor as discussed above. Detailed core analysis would be needed to explore this further.

It is known that both  $V_p$  and  $V_s$  decrease with increasing temperature (Kato et. al., 2008). Since temperature and viscosity are closely related (see Figure 1-3), it follows for  $V_p$  and  $V_s$  to be sensitive to viscosity variations as well. However, it is surprising the shear-wave sonic log did not appear more often, because bitumen has a non-zero shear modulus compared to both water and conventional hydrocarbons. One might think the shear-wave sonic log should detect the

shear modulus variations caused by the varying viscosity. The questionable quality of the shear sonic data in the project area could explain why this was not the case. With better shear-wave sonic data, the viscosity predictions would likely be improved further.

Finally, it is well known that the NMR signal can be correlated to viscosity (as discussed in section 1.3). However, none of the project viscosity wells had NMR data, so the NMR logs were blindly predicted in the viscosity wells by training prediction equations using 25 nearby NMR wells (Figure 5-4). The fact that NMR Total – NMR Free separation (which was in itself predicted from resistivity, P-wave sonic, and gamma-ray) came up as the third top predictor is very encouraging. If the viscosity wells had real NMR data, the predictions would almost certainly have been improved further.

## **6.2 – Concluding remarks regarding viscosity prediction from all well logs**

The multi-attribute analysis determined that when *all* well log types are used as predicting attributes, viscosity can be predicted with a 0.76 correlation value from: *resistivity, gamma-ray, NMR (Total – Free) separation, SP, P-wave sonic, and S-wave sonic*. These predictions modelled detailed vertical viscosity variations between the measurement points, as seen from the figures in section 5.5.

It was also demonstrated that this technique might even help distinguish between barriers and baffles to steam propagation based on the predicted viscosity gradients (ie. Figure 5-10 appears to be a barrier at 440m and 450m, and Figure 5-12 looks more like baffles throughout the lower section).

### **6.3 – Concluding remarks regarding viscosity prediction from standard well logs only**

Since most wells do not have sonic logs, and far fewer have NMR logs due to their high cost, separate viscosity predictions were generated using only the standard, most commonly-run logs. The multi-attribute analysis determined that viscosity can be predicted with a 0.70 correlation value from: *resistivity*, *gamma-ray*, and *SP*.

There were only minor differences between the predictions using all well logs versus only standard well logs. This is encouraging because it demonstrates that vertical viscosity profiles can be predicted with almost the same level of detail with only resistivity, gamma-ray, and SP logs, normally available in almost all logged wells.

### **6.4 – Concluding remarks regarding viscosity prediction from calculated seismic properties**

To extend the concept of viscosity prediction into the seismic domain, the sonic and density logs were used to calculate the various seismic properties shown in Figure 5-6. Separate viscosity predictions were then generated using the log-derived seismic properties as input attributes. The best viscosity prediction was found using *P-wave sonic* and *P-impedance*, resulting in an average prediction error of 93,000cP (within one standard deviation of all measured viscosities). However, the correlation value was only 0.35, compared to 0.76 from using all well logs.

It was observed throughout the study that log-derived seismic properties cannot yield as accurate or detailed viscosity predictions as from using all well log types. This is because seismic properties are all different combinations of  $V_p$ ,  $V_s$ , and density, and all the other petrophysical properties are not available.

### **6.5 – Concluding remarks regarding depth as a viscosity predictor**

Given the strong evidence of a correlation of increasing viscosity with depth (Figure 5-19 and appendix A3), depth logs were generated in each well and included as predicting attributes to see how depth influenced the viscosity predictions.

It was found that combining depth with the well logs and the log-derived seismic properties improved the prediction accuracy in almost all cases, except for the special case where the base reservoir has a low measured viscosity. Combining depth with the well logs captures the high resolution detail of the logs, while including the low-frequency, depth-viscosity trend from Figure 5-19. This approach achieved the highest correlation between the measured and predicted viscosities, and the lowest prediction error (Figure 5-20). The correlation value was 0.79, and I believe that combining depth with the well logs is indeed the best approach in predicting viscosity from well logs.

However, the main limitation using depth is that viscosity will always be overestimated in the special case where the base reservoir has a low viscosity, as seen in the right well of Figure 5-22.

### **6.6 – Concluding remarks regarding the potential of seismic data for viscosity prediction**

This thesis focused on predicting viscosity from well logs, which have frequencies on the order of  $\sim 10,000$  Hz. Therefore, the P-wave sonic, S-wave sonic, and density logs were low-pass filtered to 0–100/120 Hz as a proxy for what might be extracted from seismic inversion volumes. The results from Figure 5-23 and Figure 5-24 suggest that using  $V_p$ ,  $V_s$ , and density seismic inversion volumes might be capable of detecting large scale (low frequency) viscosity variations throughout the reservoir, which is still valuable information for development planning.

Finally, section 5.10 explored the question of whether sonic and density logs could detect the bitumen-water contact in the study area. Figure 5-25 shows that the sonic and density log responses are virtually unchanged across the bitumen-water contact. This is likely because the average bitumen density in the study area ( $1,010 \text{ kg/m}^3$ ) is too similar to the density of water ( $1,000 \text{ kg/m}^3$ ) to yield a detectable acoustic impedance contrast. Therefore, it is unlikely that 3D seismic survey data from this reservoir will reveal any sort of bitumen-water contact response.

## **6.7 – Future Work**

There is an abundance of future work that could be done to expand and to better understand the results of this thesis. This section explores a few key ideas:

Incorporating spectral gamma-ray logs, which split the total gamma ray log into the potassium, thorium, and uranium components, could help explain why the total gamma-ray log comes up as the second-best viscosity predictor.

There is a chance that using a neural network approach to predict viscosity from well logs may improve prediction accuracy. The multi-linear regression approach as described in chapter 3 uses combinations of linear regressions in crossplot space, however a neural network might account directly for potential non-linear relationships between viscosity and the well logs.

It should be very interesting for a similar study to be carried out in a different oil sands reservoir. If the same attributes come up as the best viscosity predictors (resistivity, gamma-ray, SP, and sonic), that would be a large step toward the ultimate goal of developing a generalized viscosity prediction equation applicable to any oil sands reservoir, albeit with a unique calibration constant for each (as explored in section 5.7). If no viscosity measurements are available in the reservoir of interest, the prediction equations developed in this thesis (Appendix

A1 and Appendix A2) should reveal *qualitative vertical viscosity variations* without the need of a calibration constant.

Finally, the million-dollar question is whether seismic survey data can detect large-scale viscosity variations throughout the reservoir. Pre-stack 3D (and 4D) seismic data exists throughout the study area. By using a multi-attribute approach relating the measured viscosities to seismic inversion volumes, we would begin to see the potential of seismic data for viscosity prediction. The results from section 5.9 demonstrate that there is a possibility. Another approach would be to predict all the well logs from seismic inversion volumes, and use the resulting well-log volumes to predict viscosity.

## **6.8 – Final Remark**

This thesis demonstrated that multi-attribute analysis of well logs can successfully predict bitumen viscosity with correlations of 70% and greater, given sufficient in-situ samples of laboratory viscosity measurements to train the model. Blind predictions within about 0.7 standard deviations of accuracy can now be performed on any nearby well that has a reliable, standard suite of well logs. Note that, for uniform comparison, all prediction results leading to the conclusions of this thesis were calibrated to lab-measured well viscosities at 35<sup>0</sup>C. At virgin reservoir conditions, where temperatures may be around 10<sup>0</sup>C, viscosities are on the order of millions of centipoise.

Reliable estimation of bitumen viscosity adds value to any heavy oil or oil sands project because viscosity is the “*most important parameter influencing production and development*” (Batzle et. al., 2006). A reliable estimate of oil viscosity variations throughout a reservoir will greatly aid in determination of a development plan for optimal recovery from the reservoir.

The ultimate goal would be to expand the analysis of this thesis from one reservoir to several reservoirs, and develop a general viscosity prediction equation that, with a unique calibration constant, would apply to any reservoir. A similar concept to the Gardner (1974) relation for predicting P-wave velocity from the density log.

## References

- Alboudwarej, H., Felix, J., Taylor, S., Badry, R., Bremner, C., Brough, B., Skeates, C., Baker, A., Palmer, D., Pattison, K., Beshry, M., Krawchuk, P., Brown, G., Calvo, R., Triana, J., Hathcock, R., Koerner, K., Hughes, T., Kundu, D., Cardenas, J., & West, C. (2006). Highlighting heavy oil. *Schlumberger Oilfield review*, 18(2), 34-53.
- Batzle, M., Hofmann, R., & Han, D. H. (2006). Heavy oils—Seismic properties. *The Leading Edge*, 25(6), 750-756.
- Beggs, H. D., & Robinson, J. R. (1975). Estimating the viscosity of crude oil systems. *Journal of Petroleum technology*, 27(09), 1-140.
- Bryan, J., Kantzas, A., & Bellehumeur, C. (2005). Oil-viscosity predictions from low-field NMR measurements. *SPE Reservoir Evaluation & Engineering*, 8(01), 44-52.
- Cheadle, B. (2014). Heavy Future. *ES4472 Course Notes*. The University of Western Ontario. London, Ontario.
- Cheng, M., Kotov, A., Pyke, K., & Hanif, A. (2015). Improvement in Heavy-Oil Reservoir Evaluation Using Nuclear Magnetic Resonance: Long Lake and Kinosis SAGD Projects, Alberta, Canada. *Petrophysics*, 56(03), 239-250.
- Chopra, S., Lines, L. R., Schmitt, D. R., & Batzle, M. L. (Eds.). (2010). *Heavy oils: reservoir characterization and production monitoring*. Society of Exploration Geophysicists.
- Close, D., Cho, D., Horn, F., & Edmundson, H. (2009). The sound of sonic: A historical perspective and introduction to acoustic logging. *CSEG Recorder*, 34(5), 34-43.
- ConocoPhillips AER Annual Performance Presentation (2015). Subsection 3.1.1 (2f), p.30. Accessed on November 12, 2015.  
<https://www.aer.ca/documents/oilsands/insitu-presentations/2015AthabascaConocoSurmontSAGD94609426.pdf>

- De Ghetto, G., Paone, F., & Villa, M. (1995, January). Pressure-volume-temperature correlations for heavy and extra heavy oils. In *SPE International Heavy Oil Symposium*. Society of Petroleum Engineers.
- Dunn, K. J., Bergman, D. J., & LaTorraca, G. A. (Eds.). (2002). *Nuclear magnetic resonance: Petrophysical and logging applications* (Vol. 32). Elsevier. Danville, California, U.S.A.
- Dvorkin, J., Nolen-Hoeksema, R., & Nur, A. (1994). The squirt-flow mechanism: Macroscopic description. *Geophysics*, 59(3), 428-438.
- Ellis DV, Singer JM. (2008). *Well Logging for Earth Scientists (2<sup>nd</sup> Edition)*. Springer. Dordrecht, The Netherlands.
- Faust, L. Y. (1953). A velocity function including lithologic variation. *Geophysics*, 18(2), 271-288.
- Flach, P. D. (1984). *Oil sands geology: Athabasca deposit north*. Geological Survey Department, Alberta Research Council.
- Fustic, M., Bennett, B., Adams, J., Huang, H., MacFarlane, B., Leckie, D. A., & Larter, S. (2011). Bitumen and heavy oil geochemistry: a tool for distinguishing barriers from baffles in oil sands reservoirs. *Bulletin of Canadian Petroleum Geology*, 59(4), 295-316.
- Gardner, G. H. F., Gardner, L. W., & Gregory, A. R. (1974). Formation velocity and density—The diagnostic basics for stratigraphic traps. *Geophysics*, 39(6), 770-780.
- Hampson-Russell (2016). *Emerge: Multi-Attribute Analysis* [Course notes].
- Hein, F. J. (2006). Heavy oil and oil (tar) sands in North America: an overview & summary of contributions. *Natural Resources Research*, 15(2), 67-84.
- Hein, F. J., & Cotterill, D. K. (2006). The Athabasca oil sands—a regional geological perspective, Fort McMurray area, Alberta, Canada. *Natural Resources Research*, 15(2),

85-102.

- Hein, F. J., Dolby, G., & Fairgrieve B. (2013). A regional geologic framework for the Athabasca oil sands, northeastern Alberta, Canada, In *Heavy-oil and oil-sand petroleum systems in Alberta and beyond: AAPG Studies in Geology* 64, p. 207 – 250.
- Kato, A., Onozuka, S., & Nakayama, T. (2008). Elastic property changes in a bitumen reservoir during steam injection. *The Leading Edge*, 27(9), 1124-1131.
- Kantzas, A. (2009). Advances in magnetic resonance relaxometry for heavy oil and bitumen characterization. *Journal of Canadian Petroleum Technology*, 48(03), 15-23.
- Kelly, B. M. (2012). *Processing and Interpretation of Time-Lapse Seismic Data from a heavy oil field, Alberta, Canada*. M.Sc. thesis, Department of Geoscience, University of Calgary, Calgary, AB.
- Larter, S., Adams, J., Gates, I. D., Bennett, B., & Huang, H. (2008). The origin, prediction and impact of oil viscosity heterogeneity on the production characteristics of tar sand and heavy oil reservoirs. *Journal of Canadian Petroleum Technology*, 47(01).
- Lines, L. R., Daley, P. F., & Ibna-Hamid, L. (2010). The accuracy of dipole sonic logs and its implications for seismic interpretation. *Journal of Seismic Exploration*, 19(1), 87-102.
- McKennell, R. (1956). Cone-plate viscometer. *Analytical Chemistry*, 28(11), 1710-1714.
- Miller, K. A., Nelson, L. A., & Almond, R. M. (2006). Should you trust your heavy oil viscosity measurement? *Journal of Canadian Petroleum Technology*, 45(04).
- Mossop, G. D. (1980). Geology of the Athabasca oil sands. *Science*, 207(4427), 145-152.
- Nexen AER Annual Performance Presentation (2015). p.9-13. Accessed on February 14, 2017.  
<https://www.aer.ca/documents/oilsands/insitu-presentations/2015AthabascaNexenLongLakeSAGD9485.pdf>

- Rider, M., & Kennedy, M. (2011). *The Geological Interpretation of Well Logs. 3<sup>rd</sup> Edition*. Rider-French Consulting Ltd., Glasgow, Scotland.
- Russell, B. H. (2004). *The application of multivariate statistics and neural networks to the prediction of reservoir parameters using seismic attributes*. Ph.D. thesis, Department of Geoscience, University of Calgary, Calgary, AB.
- Schlumberger. (2009). *Log Interpretation Charts: 2009 Edition*. Schlumberger. Sugar Land, Texas.
- Schneider, C. L., Mei, S., Grobe, M., & Haug, C. (2012). Beneath the oil sands: stratigraphy and structural features of the Devonian of northeast Alberta. *Canadian Society of Petroleum Geologists, GeoConvention 2012 Abstracts*, 14-18.
- Shier, D. E. (2004). Well log normalization: methods and guidelines. *Petrophysics*, 45(03).
- Smith, M. L., & Norris, J. O., & Sondergeld, C. H. (1991). The Amoco Array Sonic Logger. *The Log Analyst*, 32(03).
- Sun, B., Liu, C., Menard, G., Dunn, K. J., & LaTorraca, G. A. (2007). Apparent hydrogen index and its correlation with heavy oil viscosity. In *48th Annual Logging Symposium*. Society of Petrophysicists and Well-Log Analysts.
- Teare, M., Burrowes, A., Baturin-Pollock, C., Rokosh, D., Evans, C., Gigantelli, P., & Marsh, R. (2012). ST98-2012: Alberta's energy reserves 2011 and supply/demand outlook 2012– 2021. *Calgary, Alberta: Energy Resources Conservation Board*.
- Vasheghani, F., & Lines, L. R. (2012). Estimating heavy oil viscosity from crosswell seismic data. *Journal of Seismic Exploration*, 21(3), 247-266

## Appendices

### A.1. Viscosity prediction equations (derived using Hampson-Russell Emerge™)

Viscosity from standard logs, sonic, and (predicted) NMR logs:

$$\eta = 168100 + \frac{1808200}{ResMedium} - 282150 * \ln(|GR|) + 84000(NMRtotal - NMRfree)^{\frac{1}{2}} + \frac{4588000}{SP} + \frac{398515000}{Pwave\ sonic} - \frac{315901000}{Swave\ sonic} \quad (A1.1)$$

where  $\eta$  is viscosity in centipoise, *ResMedium* is the medium resistivity curve in ohmm, *GR* is gamma ray curve in GR-API units,  $(NMRtotal - NMRfree)$  is the separation between the predicted NMR total and predicted NMR free porosity curves in porosity decimal units, *SP* is the spontaneous potential curve in mV, *Pwave sonic* and *Swave sonic* are the compressional and shear sonic logs in  $\mu\text{s/m}$ , respectively. All predicting logs are *normalized* (section 5.1).

**Number of training wells:** 40

**Average Validation Error:** 69,300cP (0.693 of 1 standard deviation)

**Correlation:** 0.76

Viscosity from standard logs only:

$$\eta = 473300 + \frac{1756600}{ResMedium} - 139800 * \ln(|GR|) + \frac{4503600}{SP} \quad (A1.2)$$

where  $\eta$  is viscosity in centipoise, *ResMedium* is the medium resistivity curve in ohmm, *GR* is gamma ray curve in GR-API units, and *SP* is the spontaneous potential curve in mV. All predicting logs are *normalized* (section 5.1).

**Number of training wells:** 40

**Average Validation Error:** 74,600cP (0.746 of 1 standard deviation)

**Correlation:** 0.70

Viscosity from calculated seismic properties:

$$\eta = -4672100 + \frac{1284750000}{Pwave\ sonic} + \frac{8611560000}{Pimpedance} \quad (A1.3)$$

where  $\eta$  is viscosity in centipoise, and *Pwave sonic* is the compressional sonic log in  $\mu\text{s/m}$ . *Pimpedance* is ( $V_p \cdot \text{density}$ ) calculated from the compressional sonic and density logs in units of  $[(\text{m/s}) \cdot (\text{g/cm}^3)]$ . All predicting logs are **normalized** (section 5.1).

**Number of training wells:** 40

**Average Validation Error:** 93,600cP (0.936 of 1 standard deviation)

**Correlation:** 0.35

Viscosity from standard logs, sonic, predicted NMR logs, PLUS DEPTH:

$$\eta = -183000 - 46400 * \ln(|Depth|) + \frac{3189900}{SP} + \frac{960200}{ResMedium} + \frac{5814300}{GR} + 76100(NMR_{total} - NMR_{free})^{\frac{1}{2}} \quad (\text{A1.4})$$

where  $\eta$  is viscosity in centipoise, *Depth* is the height above bitumen base in meters, *SP* is the spontaneous potential curve in mV, *ResMedium* is the medium resistivity curve in ohmm, *GR* is the gamma ray curve in GR-API units, (*NMRtotal* – *NMRfree*) is the separation between the predicted NMR total and predicted NMR free porosity curves in porosity decimal units. All predicting logs are **normalized** (section 5.1). *Sonic logs were input but did not come up as one of the top predictors.*

**Number of training wells:** 40

**Average Validation Error:** 64,600cP (0.646 of 1 standard deviation)

**Correlation:** 0.79

Viscosity from calculated seismic properties PLUS DEPTH:

$$\eta = -106300 - 73300 * \ln(|Depth|) + \frac{188454000}{Pwave\ sonic} \quad (\text{A1.5})$$

where  $\eta$  is viscosity in centipoise, *Depth* is the height above bitumen base in meters, and *Pwave sonic* is the compressional sonic log in  $\mu\text{s/m}$ . All predicting logs are **normalized** (section 5.1).

**Number of training wells:** 40

**Average Validation Error:** 69,700cP (0.697 of 1 standard deviation)

**Correlation:** 0.72

## A.2. Other useful prediction equations not discussed in the main text

(For practical use, none of the equations in this appendix contain predicted NMR logs)

Viscosity from standard logs and sonic logs (gives very similar results to Eq. A1.1):

$$\eta = -268800 + \frac{1717200}{ResMedium} - 146100 * \ln(|GR|) + \frac{4219800}{SP} + \frac{456157000}{Pwave sonic} - \frac{311075000}{Swave sonic} \quad (A2.1)$$

where  $\eta$  is viscosity in centipoise, *ResMedium* is the medium resistivity curve in ohmm, *GR* is gamma ray curve in GR-API units, *SP* is the spontaneous potential curve in mV, *Pwave sonic* and *Swave sonic* are the compressional and shear sonic logs in  $\mu\text{s/m}$ , respectively. All predicting logs are *normalized* (section 5.1).

**Number of training wells:** 40

**Average Validation Error:** 71,200cP (0.712 of 1 standard deviation)

**Correlation:** 0.74

Viscosity from standard logs, sonic logs, PLUS DEPTH (gives very similar results to Eq. A1.4):

$$\eta = -508300 - 41400 * \ln(|Depth|) + \frac{3414000}{SP} + \frac{954600}{ResMedium} + \frac{2518700}{GR} + \frac{314070000}{Pwave sonic} - \frac{167706000}{Swave sonic} \quad (A2.2)$$

where  $\eta$  is viscosity in centipoise, *Depth* is the height above bitumen base in meters, *SP* is the spontaneous potential curve in mV, *ResMedium* is the medium resistivity curve in ohmm, *GR* is gamma ray curve in GR-API units, *Pwave sonic* and *Swave sonic* are the compressional and shear sonic logs in  $\mu\text{s/m}$ , respectively. All predicting logs are *normalized* (section 5.1).

**Number of training wells:** 40

**Average Validation Error:** 65,900cP (0.659 of 1 standard deviation)

**Correlation:** 0.78

Viscosity from standard logs PLUS DEPTH (extension of Eq. A1.2):

$$\eta = 99100 - 47800 * \ln(|Depth|) + \frac{3452000}{SP} + \frac{876200}{ResMedium} + \frac{2168300}{GR} \quad (\text{A2.3})$$

where  $\eta$  is viscosity in centipoise,  $Depth$  is the height above bitumen base in meters,  $SP$  is the spontaneous potential curve in mV,  $ResMedium$  is the medium resistivity curve in ohmm, and  $GR$  is gamma ray curve in GR-API units. All predicting logs are *normalized* (section 5.1).

**Number of training wells:** 40

**Average Validation Error:** 67,000cP (0.670 of 1 standard deviation)

**Correlation:** 0.77

### A.3. Viscosity versus depth measurements from the ConocoPhillips Surmont project

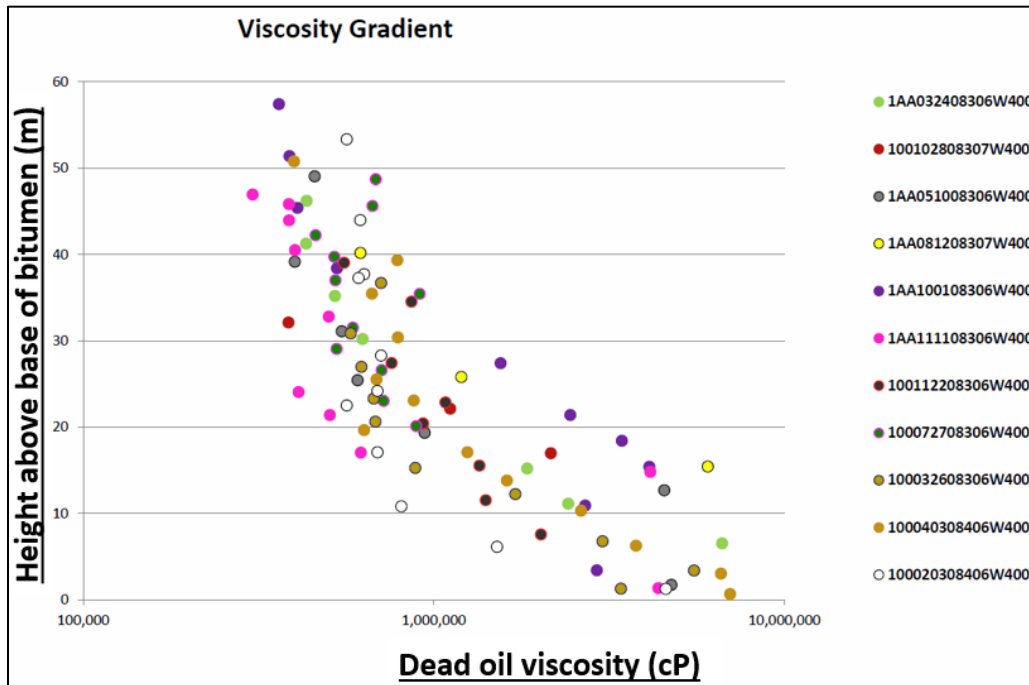


**Figure A3-1: Viscosity measurements plotted against reservoir depth for the ConocoPhillips Surmont oil sands project (2015 AER presentation).**